

THESIS FOR THE DEGREE OF DOCTOR OF PHILOSOPHY

**Copper and Manganese-based Oxygen Carriers in Chemical-Looping Combustion (CLC)  
and Chemical-Looping with Oxygen Uncoupling (CLOU)**

Mehdi Arjmand



**CHALMERS**

Department of Chemical and Biological Engineering

Chalmers University of Technology

Gothenburg, Sweden 2014

Copper and Manganese-based Oxygen Carriers in Chemical-Looping  
Combustion (CLC) and Chemical-Looping with Oxygen Uncoupling (CLOU)

MEHDI ARJMAND

ISBN 978-91-7385-956-1

© Mehdi Arjmand, 2014

Doktorsavhandlingar vid Chalmers tekniska högskola  
Ny serie nr 3638  
ISSN 0346-718X

Department of Chemical and Biological Engineering  
Chalmers University of Technology  
SE-412 96 Gothenburg  
Sweden  
Phone: +46 (0)31-772 1000

Cover: Schematic representation of the chemical-looping combustion (CLC)  
process

Printed at Chalmers Reproservice AB  
Gothenburg, Sweden 2014

## ABSTRACT

---

The chemical-looping combustion (CLC) and chemical-looping with oxygen uncoupling (CLOU) processes are attractive solutions for efficient combustion with inherent separation of carbon dioxide. These processes use a metal oxide as an oxygen carrier to transfer oxygen from an air to a fuel reactor where the fuel, or gasification products of the fuel, is converted. When solid fuel is used in CLC, the char needs to be gasified, by e.g. steam, to form H<sub>2</sub> and CO that can subsequently be oxidized to H<sub>2</sub>O and CO<sub>2</sub> by the oxygen carrier. In the case of CLOU, the oxygen carrier releases gas-phase oxygen in the fuel reactor. This enables a high rate of conversion of char from solid fuels, as CLOU eliminates the need for the gasification step required in normal CLC with solid fuels.

In this work, copper- and manganese-based oxygen carriers were investigated for the CLC and the CLOU processes. Their chemical-looping performance was examined in a laboratory-scale fluidized-bed reactor under alternating reducing and oxidizing conditions at different temperatures. The materials were generally evaluated with respect to oxygen release, reactivity and performance. Detailed material analysis and characterization of various oxygen carriers were carried out. Different gaseous fuels such as methane and synthesis gas (50% CO in H<sub>2</sub>) as well as solid fuels such as petroleum coke and wood char were used.

As copper-based materials, freeze-granulated Al<sub>2</sub>O<sub>3</sub> and MgAl<sub>2</sub>O<sub>4</sub>-supported CuO oxygen carriers were investigated for CLC and CLOU applications using methane. In order to establish the phase relationships in the Cu–Al–O system, the standard enthalpy of formation,  $\Delta H_f^0$ , of CuAl<sub>2</sub>O<sub>4</sub> was reassessed using differential scanning calorimetry (DSC). The reducing and oxidizing pathways in the Cu–Al–O system and the reversibility of the phases during the redox process were also studied.

As manganese-based materials, various manganese-based perovskite-type oxygen carriers produced by extrusion and spray-drying and different manganese ores were studied. The effect of dopants, operating temperature and calcium content on the reactivity of oxygen carriers towards methane and the stability of the perovskite-structured materials as well as tolerance towards deactivation with sulphur were examined for the CLOU process. The reactivity of manganese ores with gaseous fuels and their influence on the rate of char gasification was scrutinized for CLC application with gasification of solid fuels.

A method for obtaining the rate of oxygen release for CLOU by utilizing a devolatilized wood char has been developed and was applied to the MgAl<sub>2</sub>O<sub>4</sub>-supported CuO oxygen carrier and the extruded perovskite-type materials. Furthermore, the oxidation rate of the MgAl<sub>2</sub>O<sub>4</sub>-supported CuO oxygen carrier for CLOU was studied. Based on the obtained rates, the minimum solids inventories using these oxygen carriers were determined for a CLOU unit.

---

---

## ACKNOWLEDGMENTS

---

I would like to express my sincere gratitude to the following persons and organizations for their contribution:

My supervisor, Professor Anders Lyngfelt, for giving me the opportunity to work with the interesting subject of chemical-looping combustion (CLC). I particularly appreciate your patience, availability, openness and the quality of your advice and comments to my various questions. I remain ever grateful to you.

Associate Professor Henrik Leion, for your friendly help. Without your guidance, especially during difficult times, I would have not been able to put this work together.

Professor Tobias Mattisson, to whom I am indebted for encouraging and inspiring me. Your constructive and scrutinizing approach to my research has been very helpful.

Associate Professor Magnus Rydén, for offering the opportunity of collaboration and for interesting discussions.

Professor Abdul-Majeed Azad, for all the encouragement and guidance you rendered me throughout my research work.

Associate Professor Christopher Knee, for your help, support and assistance with thermogravimetric analysis (TGA) as well as offering the possibility for pleasant collaboration. Professor Vratislav Langer is specially acknowledged for fruitful discussions and for giving insight that led to the experiments in Paper III. My heartfelt thanks also go to Professor Itai Panas for all your advice.

Thanks to all the people in the CLC group for contributing with your great spirit: Martin, Erik, Georg, Sebastian, Volkmar, Dazheng, Golnar, Pavleta, Calle, Pontus, Patrick, Jesper, Roeland, Ali, Matthias, Malin, Peter and Ulf. My appreciation also goes to all the people at the division of Environmental Inorganic Chemistry and Energy Technology for creating a pleasant working environment. I am grateful to Esa and Erik for your technical help with equipment and instruments and to Charlotte for helping with administration at the division. Many thanks are also due to Professor Jan-Erik Svensson for offering the opportunity to work at the division and making facilities available. I would like to thank Vattenfall, Chalmers University of Technology via the Energy Area of Advance and European Research Council for financial support of this project.

Finally, I would like to thank my beloved parents and sisters for their unconditional support through all the years that I have been away from home for my studies. To them, I dedicate this work.

Mehdi Arjmand  
Gothenburg, March 2014

---

---

## LIST OF PUBLICATIONS

---

This thesis is based on the following publications, which are referred to in the text by Roman numerals and are attached to this thesis.

- I. **Arjmand M**, Azad A-M, Leion H, Lyngfelt A, Mattisson T, “Prospects of  $\text{Al}_2\text{O}_3$  and  $\text{MgAl}_2\text{O}_4$ -Supported CuO Oxygen Carriers in Chemical-Looping Combustion (CLC) and Chemical-Looping with Oxygen Uncoupling (CLOU)”, *Energy & Fuels*, 2011, 25 (11), 5493–5502
- II. **Arjmand M**, Azad A-M, Leion H, Mattisson T, Lyngfelt A, “Evaluation of  $\text{CuAl}_2\text{O}_4$  as an Oxygen Carrier in Chemical-Looping Combustion (CLC)”, *Industrial & Engineering Chemistry Research*, 2012, 51 (43), 13924–13934
- III. **Arjmand M**, Knee C, Leion H, Mattisson T, “Standard Enthalpy of Formation of  $\text{CuAl}_2\text{O}_4$  Revisited”, 2014, *Chemical Engineering Communications*, In press
- IV. **Arjmand M**, Hedayati A, Azad A-M, Leion H, Rydén M, Mattisson T, “ $\text{Ca}_x\text{La}_{1-x}\text{Mn}_{1-y}\text{M}_y\text{O}_{3-\delta}$  (M = Mg, Ti, Fe or Cu) as Oxygen Carriers for Chemical-Looping with Oxygen Uncoupling (CLOU)”, *Energy & Fuels*, 2013, 27 (8), 4097–4107
- V. **Arjmand M**, Kooiman R F, Rydén M, Leion H, Mattisson T, Lyngfelt A, “Sulphur Tolerance of  $\text{Ca}_x\text{Mn}_{1-y}\text{M}_y\text{O}_{3-\delta}$  (M = Mg, Ti) Perovskite-type Oxygen Carriers in Chemical-Looping with Oxygen Uncoupling (CLOU)”, *Energy & Fuels*, 2014, In press
- VI. **Arjmand M**, Keller M, Leion H, Mattisson T, Lyngfelt A, “Oxygen Release and Oxidation Rates of  $\text{MgAl}_2\text{O}_4$ -Supported CuO for Chemical-Looping with Oxygen Uncoupling (CLOU)”, *Energy & Fuels*, 2012, 26 (11) 6528–6539
- VII. **Arjmand M**, Leion H, Lyngfelt A, Mattisson T, “Use of Manganese Ore in Chemical-Looping Combustion (CLC) – Effect on Steam Gasification”, *International Journal of Greenhouse Gas Control*, 2012, 8, 56–60
- VIII. **Arjmand M**, Leion H, Mattisson T, Lyngfelt A, “Investigation of Different Manganese Ores as Oxygen Carriers in Chemical-Looping Combustion (CLC) for Solid Fuels”, *Applied Energy*, 2014, 113, 1883–1894<sup>†</sup>

### Contribution report:

Principal author, responsible for experimental work and data evaluation in Papers I–III and Papers VI–VIII.

Principal author, responsible for part of the experimental work and data evaluation in Papers IV and V.

---

Other related publications and contributions not included in this thesis:

- Rydén M, **Arjmand M**, “Continuous Hydrogen Production via Steam-Iron Chemical-Looping Process in a Circulating Fluidized-bed Reactor”, *International Journal of Hydrogen Energy*, 2012, 37 (6), 4843–4854
- **Arjmand M**, Leion H, Mattisson T, Lyngfelt A, “ZrO<sub>2</sub>-Supported CuO Oxygen Carriers for Chemical-Looping with Oxygen Uncoupling (CLOU)”, *Energy Procedia*, 2013, 37, 550–559<sup>\*</sup>
- Iñaki Adánez-Rubio, **Arjmand M**, Leion H, Mattisson M, Lyngfelt A, “Investigation of Combined Supports for CuO-based Oxygen Carriers for Chemical-Looping with Oxygen Uncoupling (CLOU)”, *Energy & Fuels*, 2013, 27 (7), 3918–3927
- Frohn P, **Arjmand M**, Azimi G, Leion H, Mattisson T, Lyngfelt A, “On the High Rate of Gasification of Brazilian Manganese Ore in Chemical-Looping Combustion (CLC) for Solid Fuels”, *AIChE Journal*, 2013, 59 (11), 4346–4354
- **Arjmand M**, Azad A-M, Leion H, Rydén M, Mattisson T, “CaZrO<sub>3</sub> and SrZrO<sub>3</sub>-Supported CuO Oxygen Carriers for Chemical-Looping with Oxygen Uncoupling (CLOU)”, *Energy Procedia*, 2014, *In press*<sup>§</sup>
- Keller M, **Arjmand M**, Leion H, Mattisson T, “Interaction of Mineral Matters from Coal with Oxygen Carriers in Chemical-Looping Combustion (CLC)”, *Chemical Engineering Research and Design*, 2014, *In press*
- Jing D, **Arjmand M**, Leion H, Rydén M, Mattisson T, Lyngfelt A, “Examination of oxygen uncoupling behaviour and reactivity towards methane for manganese silicate oxygen carriers in Chemical-Looping with Oxygen Uncoupling (CLOU)”, 2014, *To be submitted for publication*
- **Arjmand M**, Rydén M, Leion H, Mattisson T, Lyngfelt A, Lyngfelt A, “Rate of Oxygen Release and Sulphur Tolerance of Combined Mn-Si Oxygen Carriers in Chemical-Looping with Oxygen Uncoupling (CLOU)”, 2014, *To be submitted for publication*
- **Arjmand M**, Frick V, Rydén M, Leion H, Mattisson T, Lyngfelt A, “Screening of Combined Mn–Fe–Si Oxygen Carriers for Chemical-Looping with Oxygen Uncoupling (CLOU)”, 2014, *To be submitted for publication*

<sup>†</sup>This contribution was also presented orally at the 2<sup>nd</sup> International Conference on Chemical-looping in Darmstadt, Germany, 26–28 September 2012.

<sup>\*</sup>This contribution was also presented as a poster at the 11<sup>th</sup> International Conference on Greenhouse Gas Control in Kyoto, Japan, 18–22 November 2012.

<sup>§</sup>This contribution was also presented as a poster at the 7<sup>th</sup> Trondheim Conference on CO<sub>2</sub> Capture, Transport and Storage (TCCS–7) in Trondheim, Norway, 4–6 June 2013.

## CONTENTS

---

<b>1. INTRODUCTION</b> .....	<b>1</b>
1.1 <i>The Greenhouse Effect and Global Warming</i> .....	1
1.2 <i>Carbon Capture and Storage (CCS)</i> .....	1
1.3 <i>Chemical-Looping Combustion (CLC) and Chemical-Looping with Oxygen Uncoupling (CLOU)</i> .....	2
1.4 <i>Oxygen Carriers in CLC and CLOU</i> .....	4
1.5 <i>Scope of Study</i> .....	9
<b>2. EXPERIMENTAL DETAILS</b> .....	<b>11</b>
2.1 <i>Preparation and Manufacturing of Oxygen Carriers and Materials</i> .....	11
2.2 <i>Characterization of Oxygen Carriers and Materials</i> .....	13
2.3 <i>Experimental Setup and Procedure</i> .....	14
2.4 <i>Data Analysis and Evaluation</i> .....	17
<b>3. RESULTS AND DISCUSSION</b> .....	<b>21</b>
3.1 <i>Oxygen Release from the Oxygen Carriers for CLOU (Papers I, IV, V and VIII)</i> .....	21
3.2 <i>Reactivity of the Oxygen Carriers for CLC and CLOU (Papers I, II, IV, V and VIII)</i> .....	23
3.3 <i>Standard Enthalpy of Formation, <math>\Delta H_f^0</math>, of <math>\text{CuAl}_2\text{O}_4</math> (Paper III)</i> .....	29
3.4 <i>Phase Analysis of the Cu–Al–O System During Redox Cycle in CLC (Papers I and II)</i> .....	31
3.5 <i>Sulphur Tolerance of Perovskite-type Oxygen Carriers for CLOU (Paper V)</i> .....	34
3.6 <i>Rate of Oxygen Release from Copper-based and Perovskite-type Oxygen Carriers for CLOU (Papers VI and IV)</i> .....	39
3.7 <i>Rate of Oxidation of Copper-based Oxygen Carriers for CLOU (Paper VI)</i> .....	42
3.8 <i>Solids Circulation Rate and Inventory of Copper-based and Perovskite-type Oxygen Carriers for CLOU (Papers VI and IV)</i> .....	44
3.9 <i>Rate of Steam Gasification of Char for Manganese Ores in CLC (Papers VII and VIII)</i> .....	44
3.10 <i>Characteristics of Oxygen Carriers Before and After Redox Cycle (Papers I, II, IV, V and VIII)</i> .....	49
<b>4. CONCLUSIONS</b> .....	<b>55</b>
<b>NOMENCLATURE</b> .....	<b>59</b>
<b>BIBLIOGRAPHY</b> .....	<b>61</b>

---

---

# 1. INTRODUCTION

---

## 1.1 The Greenhouse Effect and Global Warming

The increase in the concentration of some greenhouse gases in the atmosphere is expected to cause global warming and thus create changes in the world's climate.<sup>1, 2</sup> As shown in Figure 1.1, the short wave radiation from the sun penetrates the atmosphere and reaches the earth's surface. As the earth's surface is heated up, long wave radiation is emitted which is subsequently absorbed by greenhouse gases such as water vapour, carbon dioxide, methane, nitrous oxide, and aerosols, thus trapping heat. At general thermal equilibrium conditions, this keeps the earth's surface warm at an average temperature of 17°C. However, excessive emission of the above-mentioned gases could trap more heat, thus increasing the average temperature.<sup>3</sup>

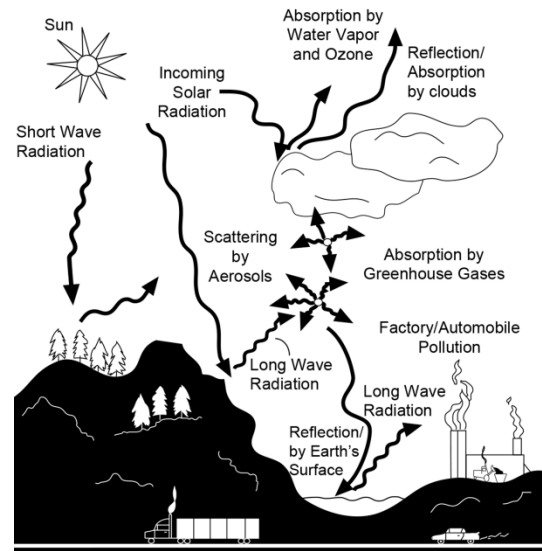


**Figure 1.1** Entrapment of part of the heat radiated from the earth's surface by greenhouse gases.<sup>3</sup>

Correlations have been found between the global average temperature and CO<sub>2</sub> concentrations in the atmosphere. With increased use of fossil fuels for energy production,<sup>4</sup> measures need to be taken to reduce anthropogenic CO<sub>2</sub> emissions in order to decrease any possible contribution to global warming. A major source for the release of CO<sub>2</sub> in the atmosphere is the combustion of fossil fuels. Therefore, the intergovernmental panel on climate change (IPCC) has recommended a 50–85% reduction in total CO<sub>2</sub> emission by 2050 to limit the anticipated global temperature rise to 2°C.<sup>5</sup> A number of alternative technologies have been proposed to mitigate the rising levels of carbon dioxide in the atmosphere. Carbon capture and storage (CCS) is one of these, which in combination with increased use of renewable energy and increased energy efficiency, could help reduce emissions of greenhouse gases to the atmosphere.

## 1.2 Carbon Capture and Storage (CCS)

By definition, CCS is the capture, transportation and storage of CO<sub>2</sub> in underground storage locations (Figure 1.2).<sup>6</sup> Pre-combustion, post-combustion and oxy-fuel combustion are among the most investigated technologies for the capture of CO<sub>2</sub> from power plants and other CO<sub>2</sub>-intensive industries. Post-combustion involves the separation of CO<sub>2</sub> from the flue gas by e.g. chemical absorption using amines. In pre-combustion, the CO in the synthesis gas produced from gasification is transformed to H<sub>2</sub> and CO<sub>2</sub> via the water-gas shift reaction, giving a gas with mainly H<sub>2</sub> and CO<sub>2</sub>.

## 1. INTRODUCTION

CO<sub>2</sub> is then separated from the H<sub>2</sub> prior to combustion. Oxy-fuel combustion involves removing N<sub>2</sub> from the air stream, and carrying out the combustion process in O<sub>2</sub> and recycled flue gas.<sup>7</sup>

The CO<sub>2</sub> capture technologies are in various stages of development and some of them are at a semi-commercial demonstration stage for CCS application.<sup>7</sup> To date, more than one thousand patents on different carbon capture technologies have been published.<sup>8</sup> However, the greatest drawback with most of the proposed processes is that there are large costs and energy penalties incurred due to gas separation steps needed in order to obtain CO<sub>2</sub> in pure form. This decreases the process energy efficiency and thus increases the electricity or final energy cost.<sup>9</sup> It is therefore favoured to investigate and develop other inexpensive CO<sub>2</sub> capture technologies.

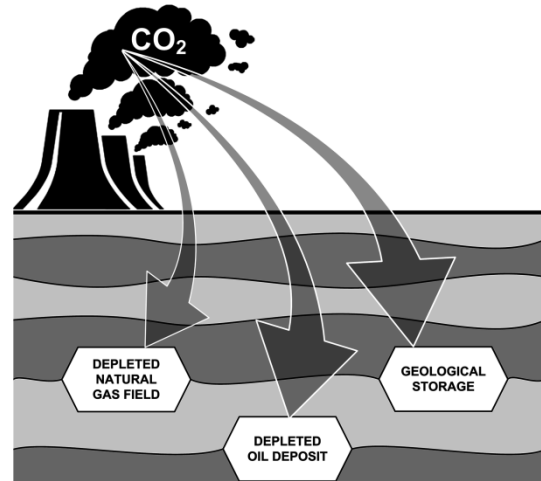
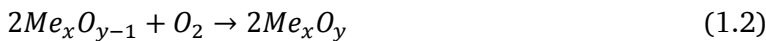
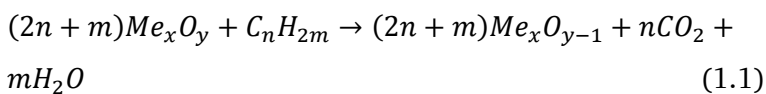


Figure 1.2 Carbon dioxide capture and transportation to underground for long-term storage.

### 1.3 Chemical-Looping Combustion (CLC) and Chemical-Looping with Oxygen Uncoupling (CLOU)

In contrast to other solutions for the capture of CO<sub>2</sub>, the chemical-looping combustion (CLC) process can give an essentially pure CO<sub>2</sub> stream from hydrocarbon conversion without any direct gas separation. In a CLC system, two reactors, a fuel reactor and an air reactor, are interconnected with an oxygen carrier circulating between these reactors.<sup>10-12</sup> When fuel and air are introduced into the reactors, the following overall reactions occur, i.e. reaction (1.1) in the fuel reactor, and reaction (1.2) in the air reactor,



Here  $Me_xO_y$  and  $Me_xO_{y-1}$  are the oxidized and reduced forms of an oxygen carrier. The scheme of the process is shown in Figure 1.3. With complete conversion of the fuel, the exhaust stream from the fuel reactor will consist of only CO<sub>2</sub> and H<sub>2</sub>O, from which pure CO<sub>2</sub> can be obtained after the condensation of water. The reduced form of the oxygen carrier,  $Me_xO_{y-1}$ , is then transferred to the air reactor where it is re-oxidized with air, making it ready for the

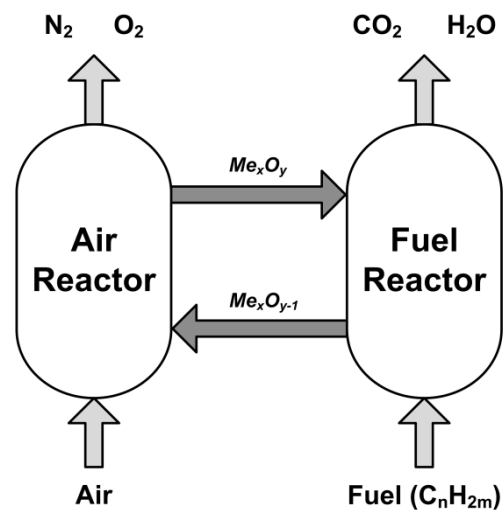


Figure 1.3 Schematic of the Chemical-Looping Combustion (CLC) process.

next cycle. Thus in CLC,  $N_2$  and  $CO_2$  gases are never mixed. The oxidation reaction is always exothermic while the reduction reaction can be exothermic or endothermic, depending on the fuel and the oxygen carrier.<sup>13</sup> However, the sum of the heat from reactions (1.1) and (1.2) is the same as for conventional combustion. Therefore, the CLC process does not entail any direct energy penalty for  $CO_2$  separation.

Chemical-looping combustion (CLC) was first introduced by Lewis and Gilliland<sup>14</sup> to produce a pure stream of  $CO_2$ . In 1994, Ishida and Jin<sup>15</sup> suggested the technique for  $CO_2$  capture and to reduce the exergy destruction caused by combustion and heat-exchange processes. In 2001, Lyngfelt et al.<sup>10</sup> proposed a unit consisting of two interconnected fluidized-bed units to implement chemical-looping combustion. The process was first demonstrated for gaseous fuels in 2003.<sup>16</sup> Today, CLC has been successfully demonstrated in a number of units of sizes up to 120 kW.<sup>17, 18</sup> Overviews of current achievements in CLC are given by Lyngfelt et al.,<sup>17, 19, 20</sup> Hossain and de Lasa,<sup>21</sup> Adanez et al.,<sup>22</sup> and Fan et al.<sup>23</sup>

The CLC process can be used with gaseous, liquid or solid fuels. In the case of solid fuels, the char remaining after devolatilization is gasified in the presence of either steam or  $CO_2$  via,<sup>24-33</sup>



The CO and  $H_2$  products are then converted by the oxygen carrier to  $CO_2$  and  $H_2O$ , as per Eq. (1.1). This means that the char conversion does not directly involve the oxygen carrier material. An alternative to CLC for solid fuels using gasification of the char, is chemical-looping with oxygen uncoupling (CLOU),<sup>34</sup> in which the char reacts directly with the gaseous oxygen released from the oxygen carrier. In comparison to CLC where the reduction of oxygen carrier and oxidation of the gaseous fuel generally occurs in a single step, an additional step is needed in CLOU for the release of gaseous oxygen from the carrier prior to the conversion of the fuel according to



This is followed by the normal combustion of the fuel via



The reduced oxygen carrier is transferred to the air reactor for re-oxidation. The net heat of reaction for the CLOU processes is the same as CLC and only the mechanism by which oxygen is accessed by the fuel differs. However when using solid fuels like coal, the CLOU process avoids the slow gasification of the solid fuel needed to produce syngas as a prerequisite for the reaction with the oxygen carrier.<sup>34</sup>

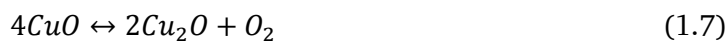
The oxygen carrier in CLOU must be able to both react (oxidize) with  $O_2$  from air and release  $O_2$  at temperatures suitable for the process, i.e. 800 to 1200°C. The most commonly proposed approach to

practically realizing CLC is to use inter-connected fluidized-bed reactors in a fashion similar to a circulating fluidized-bed boiler (CFB),<sup>10</sup> the difference being that CLC will require an active oxygen carrier rather than sand as bed material. Conventional CFB boilers often operate at an air to fuel ratio of about 1.2, which in the case of CLC corresponds to an outlet oxygen concentration close to 5% from the air reactor. To be noted is that the oxygen concentration in CLC is somewhat higher than in normal combustion since the flue gas from the air reactor does not contain CO<sub>2</sub>. Therefore, oxide systems with an equilibrium oxygen partial pressure lower than 5% at temperatures typical of the air reactor are desirable to ensure complete oxidation of the oxygen carrier particles over the whole reactor height. Otherwise, higher air ratio will be required than in conventional combustion, which would result in greater heat loss due to the larger flue gas stream. Moreover, the oxygen carrier should also be able to release a sufficiently large amount of oxygen into the fuel reactor at a sufficiently high rate. Thus, the choice of oxygen carriers for the CLOU process is limited by these kinds of considerations. Demonstration of the CLOU process<sup>35</sup> has proven the advantage of this technology over the CLC process, where slow gasification is an imperative step.<sup>36</sup> Moreover, the solids inventory in the fuel reactor of the CLOU process would be lower than in CLC due to faster fuel conversion,<sup>37,38</sup> thus limiting the need for a carbon stripper or additional treatments.

### 1.4 *Oxygen Carriers in CLC and CLOU*

A cornerstone in the development of CLC and CLOU processes is the oxygen carrier material. Thus, it is important to obtain a portfolio of inexpensive, durable oxygen carriers with sufficient reactivity. Oxides of transition metals (Mn, Fe, Co, Ni and Cu), their mixtures, and a number of natural minerals (ores), industrial wastes and by-products have been used as oxygen carriers in CLC and CLOU.<sup>17-23</sup> The reactivity of the oxygen carrier during oxidation and reduction, and the ability to fully convert the fuel have been among the most sought-after criteria. In addition, thermal stability, mechanical strength, certain fluidization characteristics and resistance to attrition and agglomeration are important. One way of achieving this for manufactured oxygen carriers is to mix the active phase (i.e. the reactive metal oxide) with a support material such as TiO<sub>2</sub>, SiO<sub>2</sub>, ZrO<sub>2</sub>, Al<sub>2</sub>O<sub>3</sub> or MgAl<sub>2</sub>O<sub>4</sub> and/or heat-treat the oxygen carriers.

Copper oxide has received a great deal of attention as an efficient oxygen carrier, owing to its high reactivity during reduction and oxidation, high oxygen transport capacity and absence of thermodynamic limitation for the complete conversion of a fuel.<sup>17-23</sup> The CuO–Cu<sub>2</sub>O oxide pair is also one of the prominent monometallic oxygen carriers suitable for the CLOU process along with Mn<sub>2</sub>O<sub>3</sub>–Mn<sub>3</sub>O<sub>4</sub> and CoO–Co<sub>3</sub>O<sub>4</sub> oxide pairs.<sup>34</sup> Figure 1.4 illustrates the equilibrium partial pressure of O<sub>2</sub> as a function of temperature for these systems.<sup>39-41</sup> For instance, it can be observed that CuO decomposes to Cu<sub>2</sub>O as per reaction (1.7) when the actual concentration of oxygen is lower than the equilibrium concentration according to



As a result, oxygen is released thereby making CLOU possible. It could be inferred from Figure 1.4 that the equilibrium  $\text{O}_2$  concentration is strongly dependent on the temperature. For CuO, oxygen release takes place at oxygen concentrations below 1.5% at 900°C and 2.7%, at 925°C. Thus, from a CLOU point of view, the optimum temperature of the air reactor is most likely in the range of 900 to 925°C for Cu-based oxygen carriers.

Despite the attractive features of CuO as an oxygen carrier, its use is not without limitations. For example, CuO suffers from a tendency towards agglomeration upon full reduction,<sup>42</sup> due to the formation of elemental

copper which has a rather low melting temperature (1085°C). Various supports of those mentioned above have been investigated for Cu-based oxygen carriers, among which  $\text{Al}_2\text{O}_3$  has received considerable attention.<sup>26, 42-58</sup> However, when using  $\text{Al}_2\text{O}_3$  as a support material, another difficulty arises due to the facile interaction between CuO and  $\text{Al}_2\text{O}_3$  either during synthesis or during operation, resulting in partial loss of CuO and CLOU behaviour caused by the formation of copper(II) aluminate ( $\text{CuAl}_2\text{O}_4$ ) and copper(I) aluminate ( $\text{CuAlO}_2$ ; delafossite).<sup>26, 42-58</sup> Since the copper-aluminate phases are highly reducible, the interaction between the support and the active phase does not necessarily cause a problem with respect to application for CLC. For CLOU however, this interaction should be avoided in order to preserve CuO as the active phase, for instance by using other unreactive support materials. Nonetheless, the use of  $\text{Al}_2\text{O}_3$  as a support material for CuO oxygen carriers in CLC is favoured because of its abundance and lower cost, e.g. compared to  $\text{ZrO}_2$ .

Most of the early studies using Cu-based oxygen carriers had been carried out at low temperatures (~850°C or below) where the CLOU effect is small, i.e. application for CLC, where the focus has been on the direct gas-solid reaction between CuO and fuel.<sup>42, 43, 46-81</sup> However at higher temperatures (~950°C), an increase in the carbon conversion rate in the vicinity of CuO particles has been reported as associated with the direct oxidation of char.<sup>14</sup> It is now well established that CuO decomposes to  $\text{Cu}_2\text{O}$  when the actual concentration of oxygen is lower than the equilibrium concentration.<sup>34</sup> Research has also been conducted on Cu-based oxygen carriers in the temperature regime applicable for CLOU in fluidized-bed batch reactors,<sup>27, 34, 37, 56, 65, 82-87</sup> continuous operations<sup>35, 38, 44, 83, 88, 89</sup> and thermogravimetric studies,<sup>84, 87, 90-93</sup> with and without support materials.

For the  $\text{Mn}_2\text{O}_3$ – $\text{Mn}_3\text{O}_4$  oxide pair as shown in Figure 1.4, re-oxidation is restricted to lower temperatures which are of less practical importance for a realistic CLC unit. It is however possible to

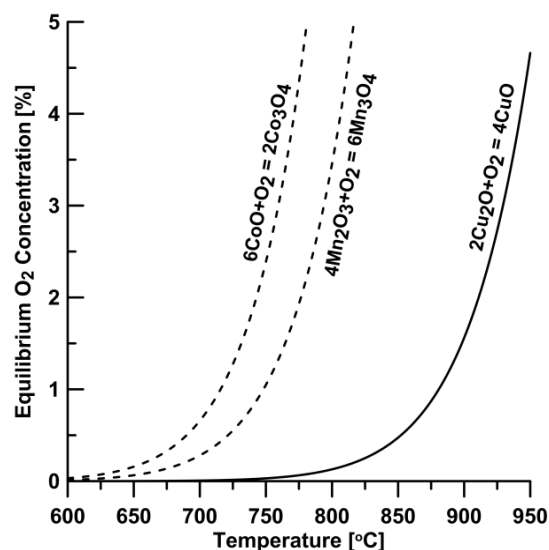


Figure 1.4 Partial pressure of gas-phase  $\text{O}_2$  over metal oxide systems of  $\text{CuO}/\text{Cu}_2\text{O}$ <sup>39</sup>  $\text{Mn}_2\text{O}_3/\text{Mn}_3\text{O}_4$ ,<sup>40</sup> and  $\text{Co}_3\text{O}_4/\text{CoO}$ .<sup>41</sup>

## 1. INTRODUCTION

---

overcome this thermodynamic constraint by combining manganese oxide with other oxides of, for instance, Ni, Cu, Si, Mg, Si or Fe.<sup>94-96</sup> Co-based oxygen carriers are however, less attractive due to cost, health and environmental issues.

Another group of manufactured oxygen carriers suitable for the CLOU process are  $ABO_3$  perovskite-type materials which exhibit interesting properties by virtue of their oxygen non-stoichiometry.<sup>97-107</sup> These materials can release a considerable amount of gaseous oxygen through



The amount of oxygen released in the gas phase given by  $\frac{1}{2}(\delta_{FR} - \delta_{AR})$ , can be used to burn gaseous, liquid or solid fuel during the CLOU process. The term ‘ $\delta$ ’ gauges the degree of oxygen non-stoichiometry and ‘AR’ and ‘FR’ refer to the value of  $\delta$  in the air and the fuel reactor, respectively. The oxygen non-stoichiometry of a perovskite-based material can be altered by changing parameters such as the ambient temperature or the  $O_2$  partial pressure.<sup>108-110</sup> One promising group of perovskite-type oxygen carrier materials belongs to the calcium manganate ( $CaMnO_{3-\delta}$ ) family and its slightly altered variants which have shown excellent behaviour in gaseous fuel combustion.<sup>111, 112</sup> Assuming an  $O_2$  partial pressure of 5% in the air reactor and a temperature of 950°C in the air and the fuel reactor, the change in  $3-\delta$  is approximately 0.04 for  $CaMnO_{3-\delta}$ ,<sup>108, 109</sup> which corresponds to 0.5 wt.% of gaseous oxygen release from the material. Rydén et al.<sup>111</sup> have examined  $CaMn_{0.875}Ti_{0.125}O_{3-\delta}$  as oxygen carrier in a 300 W circulating fluidized-bed reactor and reported good fluidization behaviour, stable operation and steady  $O_2$  release in an inert atmosphere; complete conversion of  $CH_4$  was also achieved. More recently, the performance of  $CaMn_{0.9}Mg_{0.1}O_{3-\delta}$  as oxygen carrier was investigated in a 10 kW natural gas fired CLC unit.<sup>112</sup> The results showed a high rate of oxygen release and full conversion of natural gas, higher than a NiO-based oxygen carrier in the same unit.<sup>113, 114</sup>

Using perovskite-type oxygen carriers in CLC or CLOU is not without limitations. Sulphur is present in significant concentrations in solid fuels and to a lesser extent in natural gas. Several studies have investigated the use of perovskite-structured materials in fuel cell applications and have shown that these oxides can be highly susceptible to deactivation in the presence of sulphur-containing compounds.<sup>115-120</sup> The general consensus is that the deactivation of these materials by  $SO_2$  or  $H_2S$  occurs in two steps. Initially, the sulphur-containing species binds or adsorbs to certain active sites by pairing with the oxygen ion vacancies. Then, the adsorbed sulphur species is converted to a sulphite (e.g.  $CaSO_3$  or  $LaSO_3$ ) and after that to a sulphate species (e.g.  $CaSO_4$  or  $LaSO_4$ ).<sup>121</sup> Severe deactivation of perovskite-type materials has been reported after exposure to even small amounts of  $SO_2$  which has been ascribed to phase separation and the formation of sulphates.<sup>117-120</sup> Substituting with transition metals such as Ti, Zr, V, Sn, Cu or Cr might make the  $SO_2$  bonding with the surface weaker, and therefore might result in a higher resistance towards  $SO_2$  poisoning.<sup>121, 122</sup> For instance, the presence of manganese at the B-site increases the reactivity for methane conversion but makes

such materials more prone to poisoning by  $\text{SO}_2$ , while the presence of chromium at the B-site decreases the former and increases the latter, owing to its acidic nature.<sup>116</sup> Additionally, the presence of MgO in the materials could slow the deactivation process, as MgO preferentially reacts with sulphur, thus allowing the perovskite-based material to avoid deactivation for a longer period of time.<sup>123</sup> It should be mentioned however, that the operating conditions such as oxygen partial pressure and/or temperature in CLC or CLOU are quite different from those encountered in fuel cell applications. Experiments in a batch fluidized-bed reactor with  $\text{CaMn}_{0.875}\text{Ti}_{0.125}\text{O}_{3-\delta}$  as oxygen carrier at 950°C in the presence of  $\text{SO}_2$ , suggests a decrease in reactivity, likely due to the formation of  $\text{CaSO}_4$ .<sup>124</sup> Also, investigation of the  $\text{CaMn}_{0.9}\text{Mg}_{0.1}\text{O}_{3-\delta}$  as oxygen carrier in continuous operation at 900°C in the presence of  $\text{H}_2\text{S}$ , showed a considerable decrease in reactivity.<sup>125</sup>

Predicting the behaviour of  $\text{CaMnO}_{3-\delta}$  during the chemical-looping combustion of sulphur-containing fuels is not a trivial task. Earlier studies on the use of limestone ( $\text{CaCO}_3$ ) in fluidized-bed combustion (FBC) for capturing  $\text{SO}_2$  provide some information on the possible reaction pathways in the system Ca–S–O under oxidizing and reducing conditions,<sup>126–128</sup> which are summarized in Table 1.1. It is possible to envisage the occurrence of similar reactions in the fuel and the air reactor of a CLC or CLOU unit for perovskite-type oxygen carriers, should calcium in a perovskite-structured material form  $\text{CaSO}_4$  or CaS. Of particular importance in Table 1.1, are the decomposition reactions of  $\text{CaSO}_4$  under reducing conditions, i.e. Eq. (1.12)–(1.14), which indicate that  $\text{CaSO}_4$  is not stable under reducing conditions. Figure 1.5 shows the stability regions of CaS, CaO and

**Table 1.1 Possible reaction pathways in the Ca–S–O system in oxidizing and reducing ( $\text{CO}$  and  $\text{H}_2$ ) environments.**

Eq.	Oxidizing conditions
(1.9)	$\text{CaS} + 3/2 \text{O}_2 \rightarrow \text{CaO} + \text{SO}_2$
(1.10)	$\text{CaS} + 2 \text{O}_2 \rightarrow \text{CaSO}_4$
(1.11)	$\text{CaO} + 1/2 \text{O}_2 + \text{SO}_2 \rightarrow \text{CaSO}_4$
Reducing conditions*	
(1.12)	$\text{CaSO}_4 + \text{CO} \rightarrow \text{CaO} + \text{SO}_2 + \text{CO}_2$
(1.13)	$\text{CaSO}_4 + \text{H}_2 \rightarrow \text{CaO} + \text{SO}_2 + \text{H}_2\text{O}$
(1.14)	$\text{CaSO}_4 + 4 \text{H}_2 \rightarrow \text{CaO} + 4 \text{H}_2\text{S} + 3\text{H}_2\text{O}$
(1.15)	$\text{CaSO}_4 + 4 \text{CO} \rightarrow \text{CaS} + 4 \text{CO}_2$
(1.16)	$\text{CaSO}_4 + 4 \text{H}_2 \rightarrow \text{CaS} + 4 \text{H}_2\text{O}$
(1.17)	$\text{CaO} + \text{SO}_2 + 3 \text{CO} \rightarrow \text{CaS} + 3 \text{CO}_2$
(1.18)	$\text{CaO} + \text{SO}_2 + 3 \text{H}_2 \rightarrow \text{CaS} + 3 \text{H}_2\text{O}$
(1.19)	$\text{CaS} + 3\text{CaSO}_4 \rightarrow 4\text{CaO} + 4\text{SO}_2$

\* Hydrocarbons such as  $\text{CH}_4$  could replace CO or  $\text{H}_2$  as the reducing agent in reactions (1.12)–(1.19).

the chemical-looping combustion of sulphur-

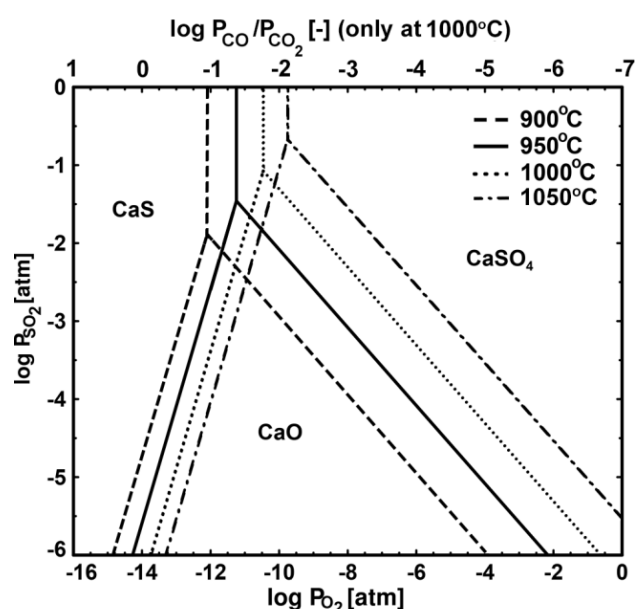


**Figure 1.5 Predominance diagram for the system Ca–S–O showing the stability regions of CaS,  $\text{CaSO}_4$  and CaO between 900 and 1050°C.<sup>129</sup> The  $\text{CO}/\text{CO}_2$  ratio corresponding to the  $\log P_{\text{O}_2}$  at 1000°C is also shown in the diagram.**

## 1. INTRODUCTION

---

$\text{CaSO}_4$  as a function of temperature and partial pressure of  $\text{O}_2$  and  $\text{SO}_2$  using FactSage® 6.3.1.<sup>129</sup> It can be readily seen that  $\text{CaO}$  is thermodynamically more stable than  $\text{CaSO}_4$  and  $\text{CaS}$ , at certain partial pressures of  $\text{O}_2$  and  $\text{SO}_2$ . Worth noting is that the stable region for  $\text{CaO}$  increases with temperature, thus favouring the decomposition of  $\text{CaSO}_4$  or  $\text{CaS}$ .

Figure 1.5 would be slightly different if  $\text{CaO}$  was replaced with  $\text{CaMnO}_{3-\delta}$ . While precise thermodynamic data on  $\text{CaMnO}_{3-\delta}$  perovskite-structured materials is lacking, it is helpful to consider  $\text{CaMnO}_{3-\delta}$  as being composed of the two individual components  $\text{CaO}$  and  $\text{MnO}_{2-\delta}$ . It is known that that a mixture of calcium and manganese oxides of the correct stoichiometry spontaneously forms perovskite-type materials during calcination, at least above  $1000^\circ\text{C}$ . This indicates that  $\text{CaMnO}_{3-\delta}$  is more strongly favoured thermodynamically at these temperatures than calcium and manganese oxides. Considering that manganese oxides are inert towards sulphur species at these temperatures, it is expected that the window of operation without the formation of solid sulphur compounds should be larger for  $\text{CaMnO}_{3-\delta}$  than for  $\text{CaO}$ .

Knowledge about the reduction and oxidation rates of oxygen carriers is also of great importance in the design phase and for determining the solids inventory in CLC and CLOU. It is important for the oxygen carrier to transport a sufficient amount of oxygen from the air reactor to the fuel reactor in order to achieve complete conversion of the fuel. For the case of endothermic reactions in the fuel reactor, it is also essential to transport adequate heat to avoid an excessive temperature drop. For CLOU oxygen carriers however, heat transport is not limiting since the overall reaction with fuel is exothermic. Reduction and oxidation kinetics of  $\text{CuO}$  oxygen carriers for CLC has been successfully acquired using thermogravimetric analysis (TGA) and fluidized-bed reactors.<sup>50, 72-79</sup> The rate of char conversion in CLOU has been reported as a 45-fold increase for a 40 wt.%  $\text{CuO}/\text{ZrO}_2$  oxygen carrier compared to synthesized  $\text{MgAl}_2\text{O}_4$ -supported  $\text{Fe}_2\text{O}_3$  and ilmenite (an iron-titanium natural mineral) oxygen carriers as determined using Mexican petroleum coke.<sup>82</sup> Chadda et al.<sup>130</sup> have obtained the rate of pure  $\text{CuO}$  decomposition in  $\text{N}_2$  in the temperature range of  $760$  to  $910^\circ\text{C}$  using TGA. The conditions of CLOU in TGA were later simulated using pure  $\text{CuO}$  powder.<sup>91</sup> Several efforts have been made to obtain the decomposition kinetics of  $\text{CuO}$  and/or oxidation rates of  $\text{Cu}_2\text{O}$  for CLOU.<sup>37, 93, 131, 132</sup> Recent studies have also investigated the reduction and/or oxidation kinetics of perovskite-type oxygen carriers for CLC and CLOU.<sup>106, 107</sup>

In general, manufactured oxygen carriers allow for better control over the physical and chemical properties of the oxygen carrier during the preparation stage. However, the manufacturing cost for such oxygen carriers may be of concern. Moreover, when utilizing solid fuels in CLC, the lifetime of oxygen carrier particles is presumably affected by the deactivation caused by ash or the loss of material with the ash during separation from the oxygen carrier. Thus for CLC with solid fuels, less expensive natural minerals, industrial wastes and by-products with sufficient reactivity are favoured compared to more costly manufactured oxygen carriers. For instance, char gasification rates have

been found to be similar in a fluidized-bed of ilmenite as in a bed of a manufactured oxygen carrier consisting of  $\text{Fe}_2\text{O}_3$  and  $\text{MgAl}_2\text{O}_4$  as support material.<sup>33</sup> Another cheap natural mineral that can be used as an oxygen carrier is manganese ore. The use of manganese ores and manganese-based industrial by-products in CLC has also been investigated,<sup>97, 133</sup> using gaseous fuels.<sup>96, 130</sup> Studies of a Slovakian manganese ore with methane as the fuel in a 300 W CLC unit have also shown a small CLOU effect.<sup>134</sup> Operation in a 10 kW CLC unit for solid fuel using a Brazilian manganese ore has showed a significant increase in the rate of steam gasification of char compared to using ilmenite as oxygen carrier.<sup>135</sup> In terms of raw material cost, manganese ore is more expensive than ilmenite. The cost of ilmenite is around 100 \$/ton whereas the price of manganese ore (metallurgical grade) has varied between 100 and 800 \$/ton in the past ten years,<sup>136</sup> with the most recent prices around 200–300 \$/ton. Although more expensive, manganese ore is considerably cheaper than manufactured oxygen carriers. It should be noted however, that the lifetime of particles plays an important role in the final cost of an oxygen carrier in the CLC process.

### ***1.5 Scope of Study***

The main objective of this thesis is to provide a deeper understanding of the use of copper and manganese-based oxygen carriers in CLC and CLOU, which is based on the studies presented in Papers I–VIII.

In Paper I, a reactivity and feasibility study of four copper-based oxygen carriers using two different supports, i.e.  $\text{MgAl}_2\text{O}_4$  and  $\text{Al}_2\text{O}_3$ , is carried out. The implication of the interaction of  $\text{CuO}$  with  $\text{Al}_2\text{O}_3$  in CLC and CLOU is also briefly addressed in that paper. Paper II provides a more detailed investigation of the reaction pathways in the  $\text{Cu–Al–O}$  phase system for the CLC process using one of the oxygen carriers ( $\text{CuAl}_2\text{O}_4$ ) from Paper I. Due to a discrepancy between thermodynamic databases, establishing the phase relationships in the  $\text{Cu–Al–O}$  system required the relevant thermodynamic data to be reassessed, which is performed in the study presented in Paper III. Paper IV investigates the influence of doping at the A- and B-sites of six different  $\text{ABO}_3$  perovskite-type materials on the reactivity towards methane, oxygen-carrying capacity, rate of oxygen release and stability. Paper V examines the sulphur tolerance of different perovskite-structured oxygen carriers for the CLOU process with respect to calcium content, temperature and dopants. In Paper VI, a method for obtaining the rate of oxygen release for CLOU is developed using one of the oxygen carriers ( $\text{CuO/MgAl}_2\text{O}_4$ ) from Paper I. The rate of oxidation and the amount of solids needed for the CLOU process are also determined in that paper. Paper VII introduces the effect of the Brazilian manganese ore on the rate of steam gasification of char. The study presented in Paper VIII further investigates the use of six different manganese ores for CLC with solid fuels. Possible explanations for the high rate of char gasification when using manganese ores as oxygen carrier are also addressed in Paper VIII. The thesis will also discuss the implications of the presented results on the use of copper- and manganese-based oxygen carriers.



## 2. EXPERIMENTAL DETAILS

### 2.1 Preparation and Manufacturing of Oxygen Carriers and Materials

The physical properties and characteristics of the copper-based oxygen carriers are summarized in Table 2.1. The particles used in these studies were manufactured by freeze-granulation which involves the preparation of a water-based slurry of active oxides, support powders, additives and binders with intended ratios followed by pumping through a spray nozzle and into liquid nitrogen to form spherical particles upon instantaneous freezing. The samples were calcined at 950 and 1050°C for 6 h. For reassessing the thermodynamic data pertaining to  $\text{CuAl}_2\text{O}_4$ , the C4A-1050 sample was re-calcined in air at 1050°C for an additional 6 h in order to complete the transition to  $\text{CuAl}_2\text{O}_4$ .

The physical properties and characteristics of the extruded perovskite-type oxygen carriers are shown in Table 2.2. These oxygen carriers were produced by mechanical homogenization of primary solids, additives and binders in a rotary evaporator followed by extrusion, drying and calcination at 1300°C for 6 h, details of which are provided in Paper IV. Table 2.3 summarizes the physical properties and characteristics of the spray-dried perovskite-type oxygen carriers. The spray-drying technique is similar to the freeze-granulation process. In this technique, the water-based slurry with intended ratios of oxides, additives and binders is pumped through a spray-drying nozzle to form spherical particles which are then injected into a hot spray-drying chamber. This was followed by calcination of the materials at 1300°C for 4 h.

The physical properties and characteristics of the manganese ores are indicated in Table 2.4. Table 2.5 also shows the composition analysis of the investigated manganese ores as determined by

**Table 2.1 Physical properties and characteristics of the copper-based oxygen carriers investigated.**

Oxygen carrier	C4A-950	C4A-1050	C4MA-950	C4MA-1050
Theoretical CuO content [wt.%]		40		
Support phase		$\text{Al}_2\text{O}_3$		$\text{MgAl}_2\text{O}_4$
Effective density [g/cm <sup>3</sup> ]	2.4	1.3	2.1	2.6
BET specific surface area [m <sup>2</sup> /g]	4.1	4.2	11.7	6.5
Crushing strength [N]		<0.5		
Porosity [%]	–	–	47.6	–
Crystalline phase identified by XRD	$\text{CuO}$ , $\alpha\text{-Al}_2\text{O}_3$ , $\text{CuAl}_2\text{O}_4^*$	$\text{CuAl}_2\text{O}_4$ , $\alpha\text{-Al}_2\text{O}_3$ , $\text{CuO}^*$		$\text{CuO}$ , $\text{MgAl}_2\text{O}_4$

\* minor phase

## 2. EXPERIMENTAL DETAILS

inductively coupled plasma mass spectrometry (ICP-MS). The ores were not pre-treated in any way except for being crushed and sieved. In Paper VII, ilmenite and in Paper VIII, ilmenite as well as a manufactured Mn-oxide oxygen carrier consisting of  $Mn_3O_4$  and MgO-stabilized  $ZrO_2$  as support material (40/60 wt.%), were used for comparison. The ilmenite had been activated using

**Table 2.2 Physical properties and characteristics of the extruded perovskite-type oxygen carriers.**

Oxygen carrier	Nominal composition	Crushing strength [N]	Bulk (tapped) density [ $g/cm^3$ ]	BET specific surface area [ $m^2/g$ ]
CM	$CaMnO_{3-\delta}$	1.4	1.62	0.28
CLM	$Ca_{0.9}La_{0.1}MnO_{3-\delta}$	1.2	1.72	0.44
CLMM	$Ca_{0.9}La_{0.1}Mn_{0.9}Mg_{0.1}O_{3-\delta}$	1.3	2.27	0.48
CLMT	$Ca_{0.9}La_{0.1}Mn_{0.9}Ti_{0.1}O_{3-\delta}$	1.5	1.68	0.40
CLMF	$Ca_{0.9}La_{0.1}Mn_{0.9}Fe_{0.1}O_{3-\delta}$	2.8	2.21	0.23
CLMC	$Ca_{0.9}La_{0.1}Mn_{0.9}Cu_{0.1}O_{3-\delta}$	1.7	3.08	0.08

**Table 2.3 Physical properties and characteristics of the spray-dried perovskite-type oxygen carriers.**

Oxygen carrier	Nominal composition	Crushing strength [N]	Bulk (tapped) Density [ $g/cm^3$ ]	BET specific surface area [ $m^2/g$ ]
C49M	$CaMnO_{3-\delta}$	0.47	1.4	0.28
C45M	$Ca_{0.83}MnO_{3-\delta}$	0.42	1.3	0.27
C50MMg	$CaMn_{0.90}Mg_{0.10}O_{3-\delta}$	1.40	1.5	0.37
C46MMg	$Ca_{0.85}Mn_{0.90}Mg_{0.10}O_{3-\delta}$	0.30	1.4	0.25
C43MMg	$Ca_{0.75}Mn_{0.90}Mg_{0.10}O_{3-\delta}$	0.50	1.1	0.40
C40MMg	$Ca_{0.65}Mn_{0.90}Mg_{0.10}O_{3-\delta}$	0.23	0.9	0.47
C50MTMg	$CaMn_{0.775}Mg_{0.10}Ti_{0.125}O_{3-\delta}$	1.40	1.6	0.33
C46MTMg	$Ca_{0.85}Mn_{0.775}Mg_{0.10}Ti_{0.125}O_{3-\delta}$	1.01	1.4	0.29
C43MTMg	$Ca_{0.75}Mn_{0.775}Mg_{0.10}Ti_{0.125}O_{3-\delta}$	1.37	1.3	0.29
C40MTMg	$Ca_{0.65}Mn_{0.775}Mg_{0.10}Ti_{0.125}O_{3-\delta}$	0.73	1.2	0.27

**Table 2.4 Physical properties and characteristics of the manganese ores investigated.**

Oxygen carrier	S. Africa B	S. Africa A	Norway	Brazil	Slovakia	Egypt
Origin	Nchwaning	Wessels	–	Buritirama	–	Sinai
Bulk (tapped) density [ $g/cm^3$ ]	2.09	2.43	1.63	1.72	1.67	1.45
BET specific surface area [ $m^2/g$ ]	0.63	0.65	6.73	3.13	5.07	7.09
Crushing strength [N]	1.5	2.3	1.2	1.1	1.4	1.7

**Table 2.5 Composition analysis of the manganese ores investigated.**

Oxide	Content [wt.%]					
	S. Africa B	S. Africa A	Norway	Brazil	Slovakia	Egypt
SiO <sub>2</sub>	4.13	1.32	10.5	9.17	11.1	3.35
Al <sub>2</sub> O <sub>3</sub>	0.317	0.372	4.49	7.65	0.454	1.1
CaO	7.58	5.76	2.33	0.291	9.46	14.2
Fe <sub>2</sub> O <sub>3</sub>	18.7	26.6	8.48	8.02	8.23	22.8
K <sub>2</sub> O	<0.1	0.176	0.467	1.25	0.835	0.252
MgO	1.08	0.776	0.465	0.661	2.83	1.55
MnO	63.3	57.2	63.3	68.8	62.3	48.8
Na <sub>2</sub> O	<0.05	0.085	<0.05	<0.05	0.432	0.559
P <sub>2</sub> O <sub>5</sub>	0.0773	0.0974	0.114	0.129	0.0609	0.145
TiO <sub>2</sub>	0.017	0.0256	0.0987	0.661	0.0553	0.0423

**Table 2.6 Composition analysis of the solid fuels used.**

Fuel	$H_f$ [MJ/kg] (as received)	Proximate [wt.%] (as received)			Ultimate [wt.% d.a.f.]				
		Moisture	Ash	Volatile matter	C	H	N	S	O
Petroleum coke	31.7	1.1	3.9	11.6	87.7	3.2	1.9	6.9	0.2
Wood char	32.1	4.3	3.2	22.9	81.5	3.3	0.6	0.02	11.2
Devolatilized wood char	28.7	1.4	3.4	1.7	93.4	<0.2	1.11	0.03	1.9

syngas for 30 cycles at 900°C, and in this way, a stable reactivity was achieved.<sup>137</sup> For physical properties and characteristics of the ilmenite particles, see Leion et al.<sup>138</sup> The Mn-oxide particles were manufactured by freeze-granulation and were sintered at 1150°C for 6 h. For properties of the Mn-oxide oxygen carrier, see Zafar et al.<sup>139</sup> or Johansson et al.<sup>140</sup>

All oxygen carrier particles were sieved through stainless steel screens to obtain particles in the size range of 125–180 and 180–250  $\mu\text{m}$ . Different solid fuels, namely petroleum coke (Cadereyta refinery, Mexico) and (devolatilized) wood char (Skogens Kol AB, Sweden) were occasionally used. The proximate and ultimate analysis of these fuels using thermogravimetric and calorimetric analysis are shown in Table 2.6. The fuel particles were sieved to a size range of 180–250  $\mu\text{m}$ . However, for surface analysis of fuel particles during steam gasification experiments, petcoke particles with a size range of 500–750  $\mu\text{m}$  were used.

## 2.2 Characterization of Oxygen Carriers and Materials

Several analysis and characterization techniques were used in the course of the studies presented here. Crystalline phase determination of the oxygen carriers was carried out using powder X-ray diffraction (Bruker AXS, D8 Advanced) with CuK <sub>$\alpha$ 1</sub> radiation. The bulk (tapped) density was measured for particles in the size range of 125–180  $\mu\text{m}$  using a graduated cylinder. Occasionally,

## 2. EXPERIMENTAL DETAILS

---

for obtaining the effective density of the particles, a theoretical void fraction of 0.37 of a packed-bed with uniform spherical particles was assumed. The Brunauer-Emmett-Teller (BET) specific surface area was measured by N<sub>2</sub>-adsorption (Micromeritics, TriStar 3000). The particle size distribution (PSD) was determined using a light microscope (Nikon, SMZ800) and ImageJ software<sup>141</sup> which measured the area of an ellipse fitted to a large number of particles. The crushing strength (force needed to fracture a single particle) was measured using a digital force gauge (Shimpo, FGN-5) for particles in the size range of 180–250 μm. 30 measurements were made for each sample and the average value was chosen as the representative crushing strength. The morphology of the particles was examined with an environmental scanning electron microscope (ESEM) fitted with a field emission gun (FEI, Quanta 200) and energy-dispersive X-ray (EDX).

In order to assess the oxygen-carrying capacity ( $R_o$ ) of the investigated materials for CLOU, a thermogravimetric analyser (Netzsch, STA 409 PC *Luxx*) was used. For this purpose, approximately 20 mg of a used sample was exposed to high purity N<sub>2</sub> with an inlet flow rate of 20–50 mL<sub>N</sub>/min at a given temperature. The heating rate was a linear ramp of 40°C/min and after reaching the set temperature, isothermal condition was maintained for 30 min. Prior to this, the thermobalance was calibrated with an empty Al<sub>2</sub>O<sub>3</sub> crucible under identical experimental conditions.

The attrition rate of the particles sized 125–180 μm was measured using a customized jet-cup attrition rig,<sup>142</sup> which simulates the effects of grid jet attrition and cyclone attrition in a circulating fluidized-bed combustor. The jet-cup attrition rig consisted of a conical cup located at the bottom of the apparatus with a nozzle that was tangentially introduced in relation to the cup wall. The cup was placed at the bottom of a gravitational particle-gas separator, which was an additional cone. Due to the increasing cross-section area in the upper cone, the gas velocity in the settling chamber was much lower than at the inlet. Therefore, the low gas velocity in this upper region allowed the elutriated particles to fall back into the cup, while the produced fines were allowed to exit. At the top of the apparatus, a particle filter (Parker) with a nominal mesh size of 0.01 μm was mounted to collect the fines. Approximately 5 g of a fresh sample was placed inside the cup and the apparatus was assembled. Air at 10 L<sub>N</sub>/min was introduced at the nozzle, which corresponds to an air jet velocity of approximately 94 m/s. In order to avoid static electricity, which otherwise would cause particles to adhere to the inner walls of the apparatus, the air was humidified by bubbling it through a column of water. Six measurements at 10 min intervals were made for every sample. These experiments were carried out at room temperature and at near atmospheric pressure.

### 2.3 *Experimental Setup and Procedure*

The schematic of the general experimental setup is shown in Figure 2.1. The experiments were carried out in a quartz fluidized-bed reactor, 870 mm long and 22 mm in inner diameter. A porous quartz plate was placed at a height of 370 mm from the bottom and the reactor temperature was measured with chromel-alumel (type K) thermocouples sheathed in inconel-600 located about 5

mm below and 25 mm above the plate. Pressure transducers (Honeywell) were used to measure the pressure drop over the bed of particles and the quartz plate at a frequency of 20 Hz. By measuring the fluctuations in the pressure drop, it was possible to determine if the particles were fluidized or not, i.e. a defluidization would be noted from a decrease in pressure fluctuations. The exit gas stream from the reactor was led into a condenser to remove water, which is generated during the oxidation of the fuel and from the introduced steam in case of gasification

experiments. Where applicable, the steam flow rate in the reactor was calibrated by measuring the mass of the water condensed at the outlet of the reactor. In order to obtain an understanding of the degree of deactivation of perovskite-structured oxygen carriers, a mass balance for sulphur had to be made over the reactor system. However, a major difficulty is the high solubility of  $\text{SO}_2$  in water<sup>143</sup> which leads to a partial loss of  $\text{SO}_2$  in the condensed water produced from the conversion of methane during reduction. Therefore, in experiments involving the measurement of  $\text{SO}_2$ , the condenser was replaced with a filter pipe directly after the sampling probe followed by a short heated line. The filter was filled with granulated magnesium perchlorate anhydrous ( $\text{Mg}(\text{ClO}_4)_2$ ) as the drying agent in order to dry the effluent stream. In this manner,  $\text{SO}_2$  was prevented from dissolving in the water produced during the conversion of methane.

The composition of the dry gas was measured using a gas analyser (Emerson, Rosemount NGA-2000), which measured the concentrations of  $\text{O}_2$  through a paramagnetic channel, measured  $\text{CO}_2$ ,  $\text{CO}$ ,  $\text{CH}_4$  and  $\text{SO}_2$  through infrared channels and measured  $\text{H}_2$  through the difference in thermal conductivity of  $\text{H}_2$  and  $\text{N}_2$ , with a correction for other measured gases. For experiments using methane or synthesis gas (50%  $\text{CO}$  in  $\text{H}_2$ ) as the fuel, the solid fuel injection and the sweeping gas parts were removed from the reactor system.

The reactivity and feasibility studies of the different oxygen carriers for CLC and/or CLOU processes were investigated at temperatures ranging from 850 to 1050°C under alternating reducing ( $\text{CH}_4$  and/or 50%  $\text{CO}$  in  $\text{H}_2$ ) and oxidizing conditions (often 5%  $\text{O}_2$ , but also 10%  $\text{O}_2$  in order to accelerate the oxidation process). Approximately 15 g of the oxygen carrier particles were placed inside the reactor and the reactor was heated to the set temperature to ensure full oxidation of the carrier prior to the experiments. Hereinafter, the term “cycle” will be used to describe a sequence of reduction-oxidation periods. The reducing periods often consist of exposures to either an inert gas ( $\text{N}_2$ ), a fuel gas ( $\text{CH}_4$  or 50%  $\text{CO}$  in  $\text{H}_2$ ) or a solid fuel (petcoke or wood char), and were followed by oxidation with the aforementioned 5 or 10%  $\text{O}_2$  mixture. A set of three inert gas cycles were carried

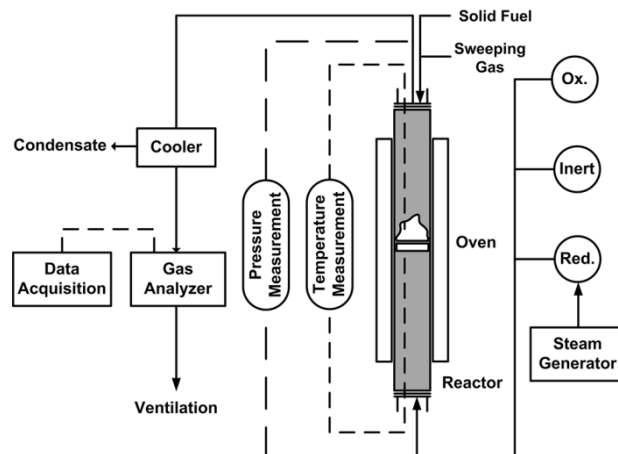


Figure 2.1 Scheme of the experimental setup used for gaseous and solid fuels.

## 2. EXPERIMENTAL DETAILS

---

out in an  $N_2$  environment to investigate the release of oxygen during a span of 360 s at different temperatures. The reduction period for  $CH_4$  was 20 s and for 50% CO in  $H_2$  it was 80 s. In these experiments, tendencies towards agglomeration, defluidization and loss of active phase were analysed by changing the experimental process variables, such as reaction time, temperature and reducing and inert environments. The redox cycles were altered particularly for additional characterization of the oxygen carriers, for instance by carrying out step-wise sequential reduction with methane and/or re-oxidation at different oxygen concentrations or partial/complete reduction of the oxygen carriers. The phase relationship analysis in the Cu–Al–O system or perovskite-based oxygen carriers are examples of this.

The tolerance of the spray-dried perovskite-structured oxygen carriers towards sulphur was investigated in a stream of 50%  $CH_4$ –0.5%  $SO_2$ –balance  $N_2$  in the temperature range of 900–1050°C. Consequently, the concentration of  $SO_2$  in this stream corresponds to 5000 vppm which is representative of a low-sulphur coal. Inert cycles were also carried out following the fuel cycles to evaluate the effect of sulphur on the oxygen release ability of the materials.

The rate of oxygen release and oxidation rates of a copper-based oxygen carrier were investigated for the CLOU process in the temperature range of 850–900°C. In order to obtain the rate of release of oxygen from CuO for CLOU, the oxygen carrier must be exposed to an oxygen-deficient environment at a suitable temperature to allow for the decomposition of CuO; reaction (1.7). However, when nitrogen is used to simulate such a condition, reaction (1.7) may approach the equilibrium oxygen concentration thus releasing oxygen at a limited rate. This rate may be slower than the actual rate in a real process, where the oxygen released will be consumed by a fuel. Therefore, such experimental approach would not readily yield the true rate of oxygen release since CuO decomposition is hindered by the equilibrium concentration of oxygen surrounding the particles. Instead, the rate of oxygen release was obtained using a devolatilized wood char as the fuel, which was introduced at the top of the reactor from which it fell down into the bed. The reactor was fluidized with inert  $N_2$ , thus eliminating possible side reactions through gasification. The oxygen released reacts directly with the char and thus the char keeps the ambient  $O_2$  concentration low. A nitrogen sweeping gas accompanied the introduction of the solid fuel at the top of the reactor to ensure that the fuel particles reach the reaction zone of the reactor. The reduction time was continued until the  $CO_2$  concentration at the outlet diminished, after which a new cycle was initiated. This method was also used to estimate the rate of oxygen release from the extruded perovskite-based oxygen carriers at 950°C. The rate of oxidation for a copper-based oxygen carrier was studied by first reducing the oxygen carrier in inert nitrogen until the oxygen concentration at the outlet diminished. Subsequently, oxidation was carried out in a flow of 5%  $O_2$ .

The experiments with solid fuels using the manganese ores were carried out in a manner similar to the reactivity test described above. In these experiments, the reactor was heated to the set

temperature of 970°C in 5% O<sub>2</sub> in N<sub>2</sub>. During reduction, a mixture of 50% steam in nitrogen was used as the fluidizing agent and petcoke and wood char were used as the fuel. In order to examine the surface of the fuel particles during steam gasification, additional experiments were carried out during which the gasification reaction was stopped by turning off the oven and quenching the reactor in N<sub>2</sub>, prior to complete conversion of the fuel particles. The bed material was separated from the partially gasified fuel particles using a magnet. The partially gasified fuel particles were then examined with ESEM and EDX.

Simultaneous thermogravimetric analysis and differential scanning calorimetry (TGA/DSC; STA 409 PC *Luxx*) was performed to reassess the standard enthalpy of formation,  $\Delta H_f^0$ , of CuAl<sub>2</sub>O<sub>4</sub>. To achieve complete reduction of CuAl<sub>2</sub>O<sub>4</sub>, the sample was exposed to a stream of 20% CO in Ar at 900°C. The reaction enthalpy,  $\Delta H_r^0$ , of the CuAl<sub>2</sub>O<sub>4</sub> sample with CO at 900°C is obtained by integrating the area under the DSC curve during the reduction period, from which the standard enthalpy of formation,  $\Delta H_f^0$ , of CuAl<sub>2</sub>O<sub>4</sub> is determined.

For further details of the experimental procedures that pertain to the different investigations, see Papers I–VIII.

#### 2.4 Data Analysis and Evaluation

The oxygen-carrying capacity,  $R_O$ , of the carriers investigated for CLOU is defined as the mass change of oxygen in the samples as follows:

$$R_O = \frac{m_{ox} - m_{red}}{m_{ox}} \quad (2.1)$$

where  $m_{ox}$  and  $m_{red}$  are the mass of the oxygen carrier in oxidized and reduced states, respectively.

Using methane as the fuel, the reactivity of the given oxygen carrier is quantified in terms of gas yield or conversion efficiency,  $\gamma_{CH_4}$ . This is defined as the fraction of fully oxidized carbon fuel divided by the carbon containing gases in the outlet stream, i.e. CO<sub>2</sub>, CO and CH<sub>4</sub>.

$$\gamma_{CH_4} = \frac{y_{CO_2}}{y_{CO_2} + y_{CH_4} + y_{CO}} \quad (2.2)$$

Here  $y_i$  denotes the concentration (vol.%) of each respective gas obtained from the gas analyser. In some cases, in order to facilitate the comparison of reactivity of different oxygen carriers at varying temperatures,  $\gamma_{CH_4,tot}$  or  $\gamma_{CH_4,ave}$  is used. These are defined as the average of gas yield in Eq. (2.2) for the entire reduction period ( $\gamma_{CH_4,tot}$ ) or for the period of  $\omega$  from 1 to 0.99 ( $\gamma_{CH_4,ave}$ ). For 50% CO in H<sub>2</sub> as the fuel, the gas yield,  $\gamma_{CO}$ , is similarly defined as in Eq. (2.2) but with  $y_{CH_4} = 0$ .

The mass-based conversion of the oxygen carrier,  $\omega$ , is defined as:

$$\omega = \frac{m}{m_{ox}} \quad (2.3)$$

where  $m$  is the actual mass of the oxygen carrier during the experiments.

## 2. EXPERIMENTAL DETAILS

---

Since it is not possible to measure the mass of the oxygen carrier in the reactor while cycling between different phases, a mass balance for oxygen has been made over the reactor system. Thus, using methane as the fuel, Eq. (2.4) is employed for calculating  $\omega$  as a function of time during the reduction period from the measured concentrations of various gaseous species in the gas analyser:

$$\omega_i = 1 - \int_{t_0}^{t_1} \frac{\dot{n}_{out} M_o}{m_{ox}} (4y_{CO_2} + 3y_{CO} + 2y_{O_2} - y_{H_2}) dt \quad (2.4)$$

where  $\omega_i$  is the instantaneous mass-based conversion at time  $i$ ,  $t_0$  and  $t_1$  are the initial and final time of measurement,  $M_o$  is the molar mass of oxygen, and  $\dot{n}_{out}$  is the molar flow rate of dry gas at the reactor outlet as measured by the analyser. In case of the fuel being 50% CO in  $H_2$ , Eq. (2.5) is used to calculate  $\omega$ ,

$$\omega_i = 1 - \int_{t_0}^{t_1} \frac{\dot{n}_{out} M_o}{m_{ox}} (2y_{CO_2} + y_{CO} + 2y_{O_2} - y_{H_2}) dt \quad (2.5)$$

The  $SO_2$  yield,  $\eta_{SO_2}$ , due to absorption of sulphur and/or reaction with the oxygen carrier particles is determined using a mass balance for  $SO_2$  over the reactor system via,

$$\eta_{SO_2} = \frac{n_{SO_2,out}}{n_{SO_2,in}} \quad (2.6)$$

where  $n_{SO_2,in}$  is the moles of  $SO_2$  introduced to the reactor and  $n_{SO_2,out}$  is the moles of  $SO_2$  in the effluent during the reduction period. Thus,  $\eta_{SO_2} = 1$  indicates that all  $SO_2$  has passed through the reactor and has been detected by the gas analyser, while  $\eta_{SO_2} = 0$  implies that all  $SO_2$  has been absorbed by and/or reacted with the oxygen carrier particles.

In order to account for the effect of back-mixing of gases in experiments where the rate of oxygen release from a copper-based oxygen carrier was obtained, the reactor's effluent concentrations were deconvoluted assuming a first-order response of the analyser. For this purpose, the actual concentration of  $CO_2$  and  $O_2$  were approximated as follows

$$y_{i,act} = y_i + \tau \frac{dy_i}{dt} \quad (2.7)$$

Here,  $y_{i,act}$  is the deconvoluted concentration of the respective gas and  $\tau$  is a time constant obtained as 1.2 s. The value of  $\tau$  was determined by fitting the deconvolution equation to the change in  $O_2$  concentration with time when the fluidizing gas was changed from oxidizing condition to inert  $N_2$  during reduction. In these experiments, it was possible to measure the flow rate at the outlet of the reactor from the analyser. However, the increase in flow rate due to a large and instantaneous expansion of the gas during the conversion of the solid fuel in the reduction phase does not coincide with the peak concentration of  $CO_2$ . This is because flow variations caused by reactions are measured instantly, while gas concentrations are measured with some time delay. Therefore, for these experiments, the corrected flow rate at the outlet of the reactor,  $\dot{n}_{out}$ , was calculated using mass balance over the reactor system by the inlet flow rate,  $\dot{n}_{in}$ , and the deconvoluted concentration of each respective outgoing gas,  $y_{i,act}$ :

---

$$\dot{n}_{out,corr} = \frac{\dot{n}_{in}}{1 - y_{CO_2,act} - y_{O_2,act}} \quad (2.8)$$

Here,  $\dot{n}_{in}$  is the sum of the flow rates from the bottom and the sweeping gas from the top of the reactor. For measurement of the rate of oxidation however, the flow rate used was the same as measured by the analyser,  $\dot{n}_{out}$ , and no deconvolution was made. For obtaining the rate of oxygen release from the extruded perovskite-type oxygen carriers, deconvolution and correction for flow rate were not performed due to the slow rate of oxygen release from these particles, as discussed in Section 3.6.

In order to calculate the conversion of a copper-based oxygen carrier in CLOU experiments,  $X_{red}$  and  $X_{ox}$  were defined, respectively, during reduction, Eq. (2.9), and oxidation, Eq. (2.10).

$$X_{red} = \int_{t_0}^{t_1} \frac{\dot{n}_{out,corr}}{n_o} (y_{CO_2,act} + y_{O_2,act}) dt \quad (2.9)$$

$$X_{ox} = \int_{t_0}^{t_1} \frac{1}{n_o} (\dot{n}_{in} y_{O_2,in} - \dot{n}_{out} y_{O_2,out}) dt \quad (2.10)$$

$n_o$  is the number of moles of molecular oxygen in the oxygen carrier that can be released. However, for the extruded perovskite-structured oxygen carriers, the mass-based conversion of the oxygen carrier during reduction with the devolatilized wood char was defined as in Eq. (2.11).

$$\omega_i = \omega_{i-1} - \int_{t_0}^{t_1} \frac{\dot{n}_{out} M_o}{m_{ox}} (2y_{CO_2} + 2y_{O_2}) dt \quad (2.11)$$

The fraction of char conversion,  $X_C$ , during solid fuel experiments is defined as

$$X_C = \frac{m_C(t)}{m_{tot}} \quad (2.12)$$

where  $m_C(t)$  is the mass of carbon converted at time  $t$  and  $m_{tot}$  is the cumulative amount of carbon converted during one cycle. Both  $m_C(t)$  and  $m_{tot}$  are determined by integrating the concentration of carbon containing gases using Eq. (2.13).

$$m_C(t) = \int_{t_0}^{t_1} \dot{n}_{out} M_C (y_{CO_2} + y_{CO} + y_{CH_4}) dt \quad (2.13)$$

where  $M_C$  is the molar mass of carbon. To determine  $m_{tot}$ , Eq. (2.13) is integrated to the end of the reduction period. Some small amounts of carbon (less than 5%) stuck to the walls or in the filter during fuel introduction, upstream of the fluidized-bed reactor. This carbon was oxidized during the subsequent oxidizing period; however, it was not included in the calculations as it did not have contact with the oxygen carrier particles. The instantaneous rate of char conversion based on the remaining non-reacted carbon in the bed,  $r_{inst}$ , is calculated as

$$r_{inst} = \frac{dX_C/dt}{1 - X_C} \quad (2.14)$$

The rate of char conversion is also demonstrated by the arithmetic average of the instantaneous rate,  $\bar{r}_{inst}$ , which is calculated for  $X_C$  between 0.3 and 0.7, in intervals of  $\Delta X_C$  of 0.02. The lower

## 2. EXPERIMENTAL DETAILS

---

limit has been chosen since the gasification rate is mainly influenced by the release of volatiles during the early stages of the reduction phase. The higher limit has been chosen to avoid effects such as fuel particles stuck on the walls of the reactor influencing the gasification rate close to the end of the reduction period.

The gas conversion during experiments with steam gasification of petcoke,  $\eta_{gas}$ , is defined as

$$\eta_{gas} = 1 - \frac{0.5y_{H_2} + 0.5y_{CO}}{y_{CO_2} + y_{CO}} \quad (2.15)$$

### 3. RESULTS AND DISCUSSION

#### 3.1 Oxygen Release from the Oxygen Carriers for CLOU (Papers I, IV, V and VIII)

Figure 3.1 shows the oxygen concentration during an inert gas ( $N_2$ ) period for the copper-based oxygen carriers and a sand reference. During this period,  $CuO$  decomposed spontaneously into  $Cu_2O$  via reaction (1.7) in the environment of inert nitrogen, thus the particles released gaseous oxygen. The oxygen concentration was relatively consistent with the theoretical equilibrium partial pressure,  $P_{O_2}$ , corresponding to the decomposition of  $CuO$  into  $Cu_2O$ , i.e. 1.5% at 900 and 2.7% at 925°C, see Figure 1.4. This is valid for all the carriers tested except C4A-1050. In contrast to the C4A-950 particles, the C4A-1050 sample had much less ability to release gaseous oxygen, i.e. it had a lower CLOU ability. The only difference between the C4A-950 and C4A-1050 samples was the temperature at which they were calcined. Yet, while C4A-950 maintained the anticipated equilibrium oxygen concentration at both operating temperatures, C4A-1050 only released oxygen to a minor extent.

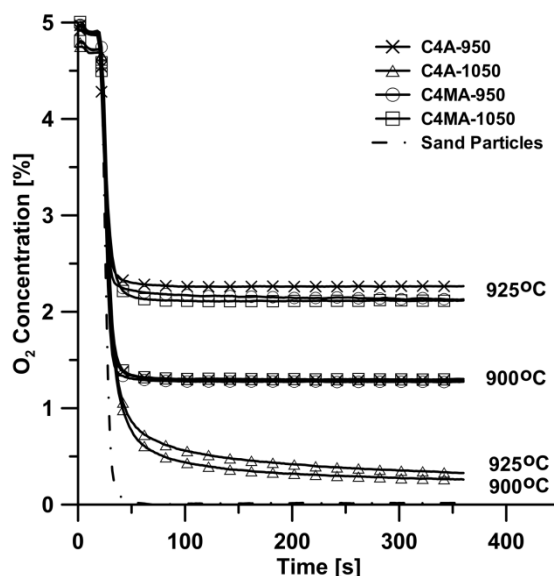


Figure 3.1 Oxygen concentrations of  $CuO/Al_2O_3$  (C4A) and  $CuO/MgAl_2O_4$  (C4MA) oxygen carriers during inert cycles at 900 and 925°C.

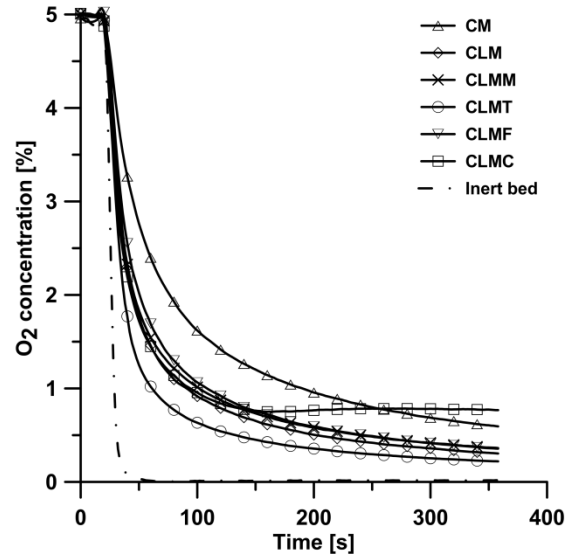
From Table 2.1, it can be seen that in the C4A-1050 sample,  $CuAl_2O_4$  was the predominant phase, while this was only a minor phase in the sample calcined at the lower temperature (950°C). In the fresh C4A-1050 sample,  $CuO$  which is capable of releasing oxygen at above 850°C appears as a minor phase together with excess and unreacted alumina. Consequently in this case, very little oxygen was released via the CLOU mechanism since  $CuAl_2O_4$  was quite incapable of releasing oxygen. The insignificant release of oxygen from the C4A-1050 sample is investigated in more detail in Section 3.4. For C4MA-950 and C4MA-1050 samples however, an identical equilibrium concentration of oxygen release was obtained irrespective of the calcination temperature, which is also in line with Figure 1.4.

Figure 3.2 shows the oxygen release profiles during the inert gas purge at 900°C for the extruded perovskite-type oxygen carriers as well as sand reference. Evidently each of the formulations exhibited oxygen uncoupling behaviour. The oxygen release trend in each of the six carriers was quite similar, indicated by a steady decline in the amount of released oxygen as a function of time. This is typical for perovskite-structured oxygen carriers, where two mechanisms are believed to be dominant: (a) the oxygen non-stoichiometry is an artefact of defect chemistry, and (b) the release

### 3. RESULTS AND DISCUSSION

or uptake of oxygen is a function of oxygen partial pressure in the ambient, according to reaction (1.8). Since the parent compound ( $\text{CaMnO}_{3-\delta}$ , CM) has the highest oxygen content (smallest  $\delta$ ), the amount of oxygen release via uncoupling in the inert environment is the highest. Doping at the A-site alone (CLM) affects the magnitude of oxygen non-stoichiometry, which is reflected in the oxygen profile being lower than that of CM.

In light of the above rationale, the amount of oxygen released is even lower for doubly-doped formulations with CLMT showing the smallest release. Interestingly, the behaviour of Cu-doped material (CLMC) was different from the others in the same series. For instance, while it followed a similar trend up to  $\sim 120$  s, the amount of released oxygen became almost non-variant at about 1% for the remainder of the inert period. In fact, during the latter part of the inert period, CLMC released the highest amount of oxygen of all the doped perovskite-type materials investigated here.



**Figure 3.2** Oxygen concentrations of extruded perovskite-type oxygen carriers during inert cycles at 900°C.

To facilitate the comparison of the oxygen uncoupling property of the different spray-dried perovskite-type materials, an average oxygen concentration during the inert phase has been used in Figure 3.3. In order to prevent the remaining oxygen in the reactor from the oxidation phase from influencing the results, the average oxygen concentration was calculated for the inert phase starting from 100 s into the inert period and until the end of the period. These ten perovskite-type oxygen carriers were categorized into three different groups, namely undoped, doped with Mg and doped with Mg and Ti, all with different calcium content. It can be observed that all of the investigated perovskite-structured materials were able to release oxygen and therefore have CLOU ability.

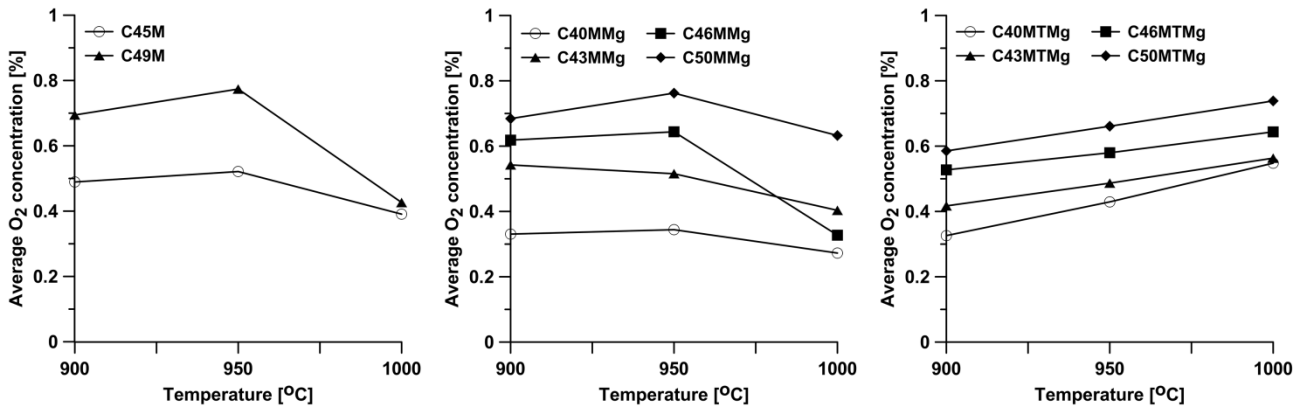


**Figure 3.3** Average oxygen concentration as a function of temperature during inert cycles for various spray-dried perovskite-type oxygen carriers following fuel cycles using 50%  $\text{CH}_4$ -rest  $\text{N}_2$  at 900, 950 and 1000°C.

During inert periods following fuel cycles, the undoped and the Mg-doped materials showed the same trend of an increase in the average oxygen concentration with an increase in the temperature from 900 to 950°C. However, for both of these materials, the average oxygen concentration decreased at 1000°C to an even lower concentration than that at 900°C. The materials doped with both Mg and Ti showed an increase in the average oxygen concentration with the temperature rise from 900 to 1000°C. Lowering the calcium content in the perovskite-type materials decreased the average oxygen concentration during the inert periods, likely due to less formation of the active perovskite-based phase, e.g.  $\text{CaMnO}_{3-\delta}$ .

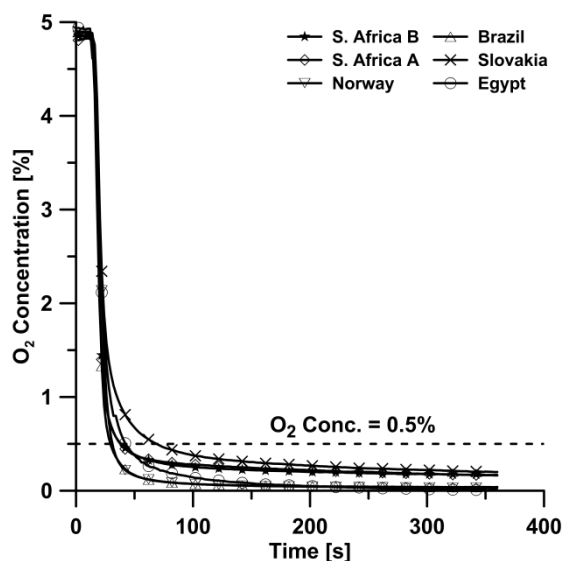


Figure 3.4 Oxygen concentrations for the manganese ores during inert cycles at 950°C.

Figure 3.4 shows the oxygen concentration during the inert gas cycles for the investigated manganese ores at 950°C after nine cycles. It should be mentioned that all of the manganese ores presented higher oxygen concentrations during the initial cycles, however during subsequent cycles, they released much less oxygen. It can be observed that the South African A and B, and the Slovakian manganese ores released little oxygen during the inert period, while the manganese ores from Norway, Brazil and Egypt released no oxygen after nine cycles.

### 3.2 Reactivity of the Oxygen Carriers for CLC and CLOU (Papers I, II, IV, V and VIII)

Figure 3.5 shows the concentration profiles for the C4A-950 sample for the 20 s reduction cycle at 900°C using methane. The decomposition of  $\text{CuO}$  during the short interval in inert gas prior to fuel injection was due to the spontaneous release of oxygen via the CLOU mechanism, similar to Figure 3.1. The fuel (methane) reacted exothermically with the oxygen released, producing  $\text{CO}_2$  and  $\text{H}_2\text{O}$ , with a concomitant increase in temperature due to the overall exothermic nature of the reactions; which is common for copper-based oxygen carriers.<sup>13</sup> The rise in temperature should raise the equilibrium oxygen concentration, although this is not observed in Figure 3.5, likely due to the fast reaction of methane with any excess of released oxygen. Since the water produced was removed

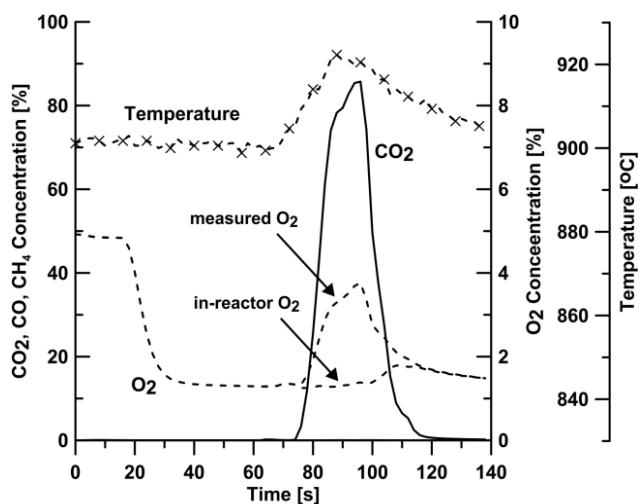


Figure 3.5 Gas concentration and temperature profiles for  $\text{CuO}/\text{Al}_2\text{O}_3$  (C4A-950) during reduction cycle at 900°C.

### 3. RESULTS AND DISCUSSION

before the gas measurement, the oxygen concentration in the reactor was considerably lower than the measured concentration.

Table 3.1 summarizes the results from the reactivity test of the copper-based oxygen carriers investigated. The materials lost approximately 3% of their mass as they were converted during 20 s of reduction with methane ( $\omega$  going from 1 to 0.97). During the oxidation cycle that followed, the carrier was expected to restore this amount of oxygen, meaning that  $\omega$  must revert from 0.97 to 1. Only then could a truly reversible redox behaviour of the oxygen carrier be anticipated. The incomplete recovery of  $\Delta\omega$  in the case of C4A-950 and C4A-1050 indicates that part of the active phase (CuO and  $\text{CuAl}_2\text{O}_4$ , respectively; Table 2.1) was not restored. However, for the C4MA, the oxygen carriers recovered nearly all the expected mass-based conversion, irrespective of the calcination temperature. This shows that the active CuO phase had remained intact when  $\text{MgAl}_2\text{O}_4$  was used as support material.

Under the experimental conditions employed, the theoretical change in the mass-based conversion,  $\Delta\omega$ , of CuO to Cu at the end of reduction with methane for 70 s should be 8%. As shown in Table 3.1, this was essentially obtained in the case with C4MA particles with full conversion of methane. Reduction times longer than 70 s did not increase the conversion any further for either of the two carriers, thus confirming that the limit of CuO reduction had been reached. On the contrary, in the cases of C4A-950 and C4A-1050 the change in  $\omega$  was less. This was associated with the incomplete methane conversion during the latter part of the reduction period.

It has been reported that the diffusion of  $\text{O}_2$  in the depleted oxygen carrier during the oxidation cycle can be hindered by the CuO layer partially surrounding the reduced  $\text{Cu}_2\text{O}$  and Cu grains.<sup>74, 91, 130</sup> Therefore the incomplete oxidation of C4A-950 could initially be connected with this resistance.

**Table 3.1 Summary of reactivity testing for the copper-based oxygen carriers.**

	C4A-950	C4A-1050	C4MA-950	C4MA-1050
<hr/>				
CH <sub>4</sub> for 20 s at 900°C				
Gas conversion [-]	Complete, $\gamma_{\text{CH}_4} = 1$			
Oxygen carrier conversion during reduction [%]	$\Delta\omega = 3$			
Oxygen carrier conversion during oxidation [%]	$\Delta\omega = 1$		$\Delta\omega = 3$	$\Delta\omega = 2.5$
<hr/>				
CH <sub>4</sub> for 70 s at 925°C				
Gas conversion [-]	Incomplete, $\gamma_{\text{CH}_4} < 1$		Complete, $\gamma_{\text{CH}_4} = 1$	
Oxygen carrier conversion during reduction [%]	$\Delta\omega = 4$		$\Delta\omega = 8$	
Oxygen carrier reversibility	Partially reversible		Reversible	
State of CuO active phase	Not intact	N/A	Intact	

However, the XRD patterns extracted at the end of experiment for C4A-950 only indicated the oxidized state of the oxygen carrier (i.e. only CuO) together with an increase in the content of  $\text{CuAl}_2\text{O}_4$  and  $\text{CuAlO}_2$ , see Paper I. Similarly, the C4A-1050 sample could not be completely oxidized, although it did not contain a significant amount of CuO in the fresh state. Moreover, the complete regain of  $\omega$  in oxidation for the C4MA samples indicates that the oxidation of  $\text{Cu}_2\text{O}$  to CuO in previous cycles was not subject to any resistance towards  $\text{O}_2$  diffusion in the depleted CuO layer as suggested previously.<sup>74, 91, 130</sup> Thus, as will be shown in the phase analysis in Section 3.4, the remaining deficiency in  $\Delta\omega$  in the case of C4A samples can be attributed to the fact that a part of the active phase ( $\text{CuO}$  or  $\text{CuAl}_2\text{O}_4$ ) was bound in the form of a ternary compound ( $\text{CuAlO}_2$ ), that is not readily converted back to the initial composition of the oxygen carrier upon oxidation.

Figure 3.6 shows the concentration profile during three typical reduction, inert and oxidation cycles for the  $\text{CuAl}_2\text{O}_4$  (C4A-1050) sample at  $925^\circ\text{C}$ . The concentrations have been corrected for the time-lag for gases reaching the analyser; however, the data have not been deconvoluted. Similar trends in concentration profiles were observed at  $900$  and  $950^\circ\text{C}$ , except for slight variations in peak concentrations. It is shown in Paper I that C4A-1050 is incapable of releasing oxygen when subjected to long inert- $\text{N}_2$  at  $900^\circ\text{C}$ . Thus it is likely that the low concentration of oxygen during the first 60 s prior to fuel injection, as shown in Figure 3.6, is due to the presence of the small amount of CuO in the oxygen carrier which decomposes into  $\text{Cu}_2\text{O}$  above  $850^\circ\text{C}$  (Figure 1.4).<sup>34</sup> The decrease in oxygen concentration to zero in the early phase of reduction is also likely connected with the free CuO in the oxygen carrier being exhausted. It was seen that the overall reduction of  $\text{CuAl}_2\text{O}_4$  with methane is exothermic as indicated by the rise in temperature during the initial stage of the reduction phase ( $t = 1-2$  min). Complete conversion of methane was obtained during the initial period of the reduction phase ( $t = 1-2$  min). Beyond this, unconverted  $\text{CH}_4$ , CO and  $\text{H}_2$  were

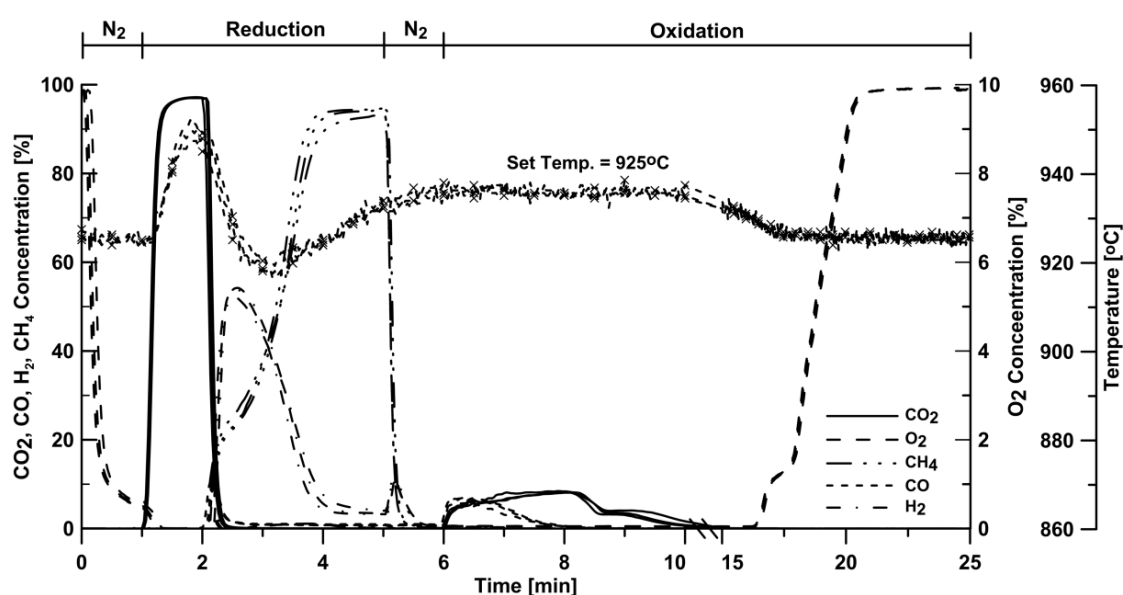


Figure 3.6 Gas concentrations and temperature profiles for  $\text{CuAl}_2\text{O}_4$  (C4A-1050) during three typical redox cycles at  $925^\circ\text{C}$ .

### 3. RESULTS AND DISCUSSION

observed in the exit stream as the carrier was being depleted of oxygen. In other words, the temperature decreased to below 920°C ( $t = 2\text{--}3.5$  min) due to the endothermic nature of the carbon formation on oxygen carrier particles.<sup>144</sup> The deposition of carbon may also be inferred from the increase in  $\text{H}_2$  concentration to approximately 50% due to the decomposition of methane during reduction and carbon burn-off during the following oxidation phase. Also worth noting in Figure 3.6, is that the oxygen concentration was zero for most of the oxidation period, i.e. more than 10 min, indicating that the oxidation reaction was limited by the flow of the oxygen-containing gas. Thus, the zero  $\text{O}_2$  concentration indicates that the oxidation occurred very fast. Furthermore, the low  $\text{O}_2$  concentration also reveals that there cannot be much CLOU effect for this material. Moreover, it appears here that the carbon burn-off was faster than the oxidation reaction, since the 10% oxygen consumed resulted in approximately 10%  $\text{CO}_2$  in the early part of the oxidation period.

A typical concentration profile during the reduction period for CLMF is shown in Figure 3.7. To begin with, the carrier was oxidized in 5%  $\text{O}_2$  but when the oxidizing stream was replaced with pure nitrogen (inert), the oxygen concentration decreased steadily in the same way as seen in Figure 3.2 for the oxygen uncoupling tests. Upon the addition of fuel,  $\text{CO}_2$  was evolved as a result of methane conversion; no  $\text{CO}$  or  $\text{CH}_4$  was detected. At the same time, the oxygen concentration decreased to zero. After the complete conversion of fuel in the early part of reduction, some methane could be detected in the reactor outlet. Also shown in Figure 3.7 is the oxygen concentration profile during oxidation in 5%  $\text{O}_2$  at 950°C, following the reduction period. Initially, the depleted oxygen carrier consumed all oxygen in the inlet stream. After about 1 min, oxygen broke through and increased steadily, finally approaching and levelling off at the inlet concentration (5%). The fact that no oxygen was seen during the initial stages of oxidation suggests that the oxygen carrier had experienced a high degree of reduction.

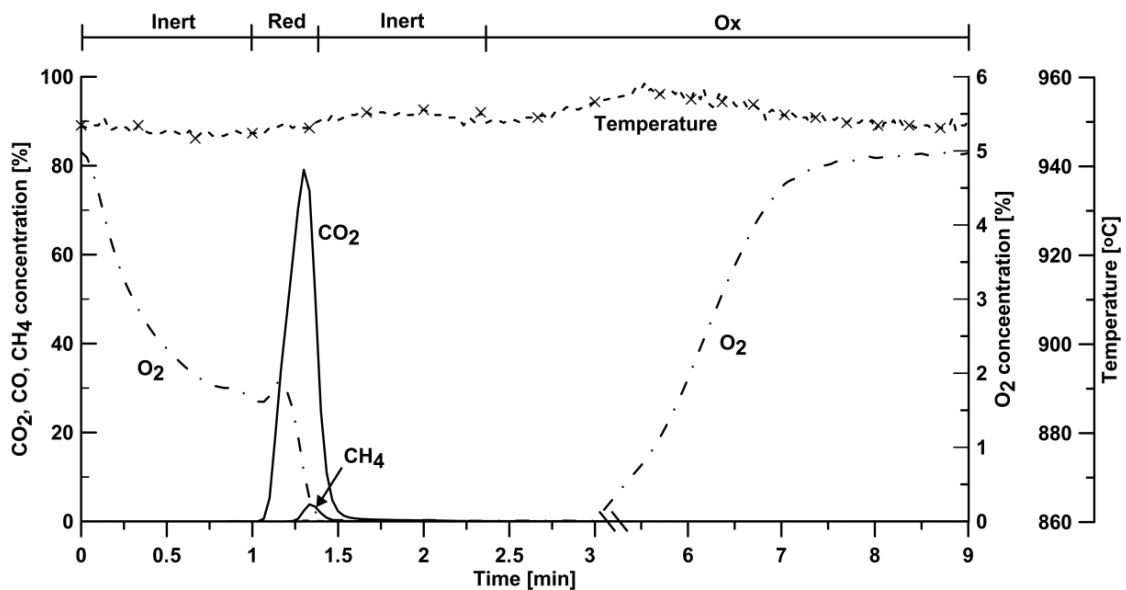


Figure 3.7 Gas concentration and temperature profiles for  $\text{Ca}_{0.9}\text{La}_{0.1}\text{Mn}_{0.9}\text{Fe}_{0.1}\text{O}_{3-\delta}$  (CLMF) during a typical redox cycle at 950°C.

Figure 3.8 shows the gas yield,  $\gamma_{CH_4}$ , as a function of the mass-based conversion degree,  $\omega$ , for the third methane period for the extruded perovskite-based oxygen carriers (except CLMC, which defluidized during reduction). Clearly, all materials showed a high gas yield which was more than 88% during the entire reducing period. The reactivity of the carriers was also investigated with synthesis gas (50% CO in H<sub>2</sub>) and the corresponding gas yield,  $\gamma_{CO}$ , with respect to CO was calculated. There was complete gas yield (100%) at 950°C for all of the formulations, with the solid conversion reaching 0.98, i.e. a change in  $\omega$  of 2%. The results of methane and syngas conversion, as well as the solid conversion compare rather well with those reported for freeze-granulated  $CaMn_{0.875}Ti_{0.125}O_{3-\delta}$ <sup>101</sup> and spray-dried  $CaMn_{0.9}Mg_{0.1}O_{3-\delta}$ <sup>104, 105</sup>

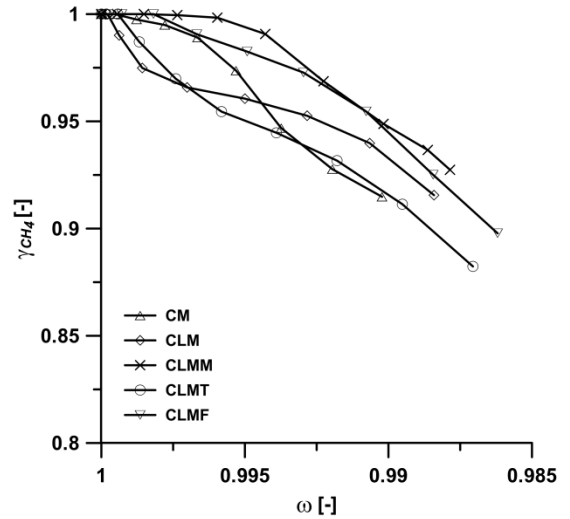


Figure 3.8 Gas yield,  $\gamma_{CH_4}$ , as a function of  $\omega$  for the different extruded perovskite-type oxygen carriers at 950°C using methane as the fuel.

The reactivity of the spray-dried perovskite-type oxygen carriers were similar to those produced by extrusion. To facilitate the comparison between the reactivity of the various spray-dried perovskite-based materials at different temperatures, the average gas yield,  $\gamma_{CH_4,ave}$ , is shown in Figure 3.9. Here, the presented  $\gamma_{CH_4,ave}$  in Figure 3.9 is representative of the average gas yield of all cycles at a given temperature. Three different effects are noticeable, i.e. the effect of calcium content, the effect of temperature and the effect of dopant. It can be seen that decreasing the calcium content in the materials generally results in a lower gas conversion. This would be expected since less active perovskite-type material is expected to be formed during synthesis in those materials. The reactivity increased with temperature for all of the investigated formulations and nearly complete gas yield was obtained at 1000°C. In this particular case, doping with Mg or Ti did not appear to significantly influence the reactivity.

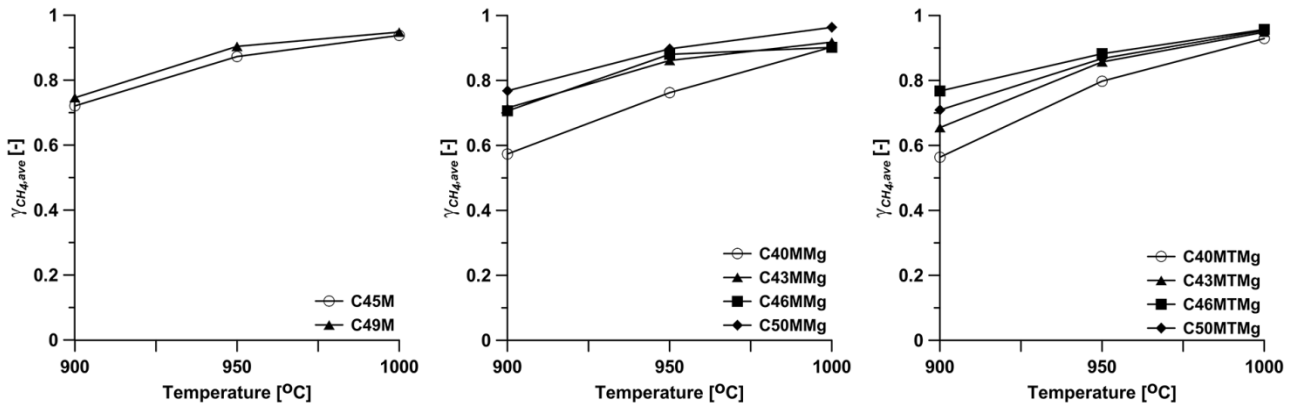


Figure 3.9 Average gas yield for CH<sub>4</sub>,  $\gamma_{CH_4,ave}$ , as a function of temperature during fuel cycles for various spray-dried perovskite-type oxygen carriers using 50% CH<sub>4</sub>-rest N<sub>2</sub> at 900, 950 and 1000°C.

### 3. RESULTS AND DISCUSSION

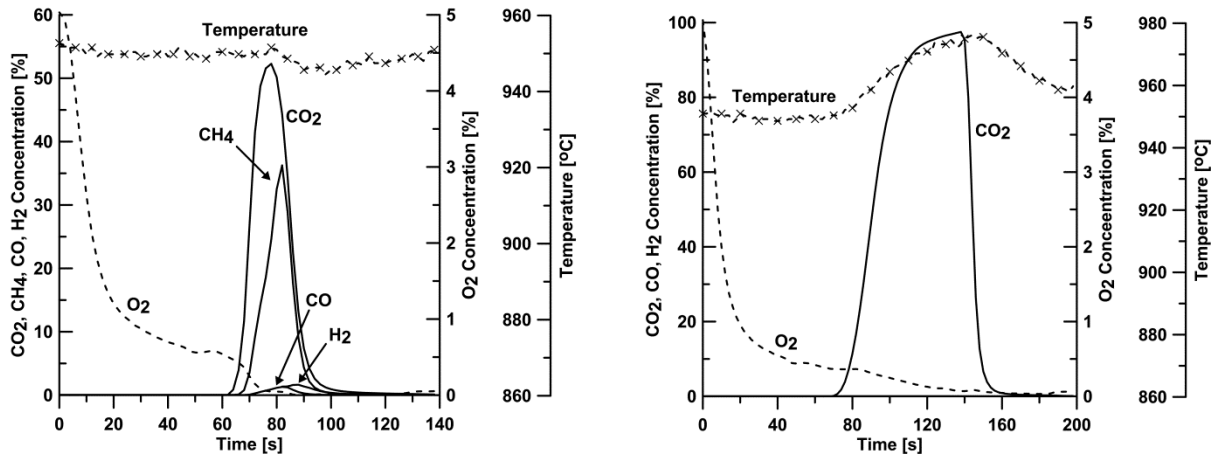


Figure 3.10 Gas concentration and temperature profiles for the Slovakian manganese ore during reduction at 950°C using (left) methane for 20 s and (right) syngas for 80 s as the fuel.

Figure 3.10 shows the concentration profiles of the Slovakian manganese ore for the 20 s reduction period using methane and 80 s reduction period using 50% CO in H<sub>2</sub> at 950°C. A small oxygen release from the Slovakian manganese ore could also be observed during the short interval in inert gas prior to the introduction of the fuels as in Figure 3.4. When methane was used as the fuel, Figure 3.10 (left), a significant part of the methane remained unreacted as it passed through the reactor. This behaviour has also been reported previously and is common for many oxygen carriers.<sup>133</sup> When 50% CO in H<sub>2</sub> was used as the fuel, all of the investigated manganese ores yielded complete conversion of the fuel, similar to Figure 3.10 (right) for the Slovakian manganese ore.

Figure 3.11 shows the reactivity (in terms of gas yield,  $\gamma_{CH_4}$  and  $\gamma_{CO}$ ) as a function of mass-based conversion of the oxygen carrier,  $\omega$ , for manganese ores at 950°C, when methane and 50% CO in H<sub>2</sub> were used as the fuel. For some of the ores, the reactivity with methane was stable during all three cycles, and for some, the reactivity decreased slightly with cycles, thus the plots in Figure 3.11 (left) show the third repeated cycle. None of the manganese ores were able to fully convert methane, thus

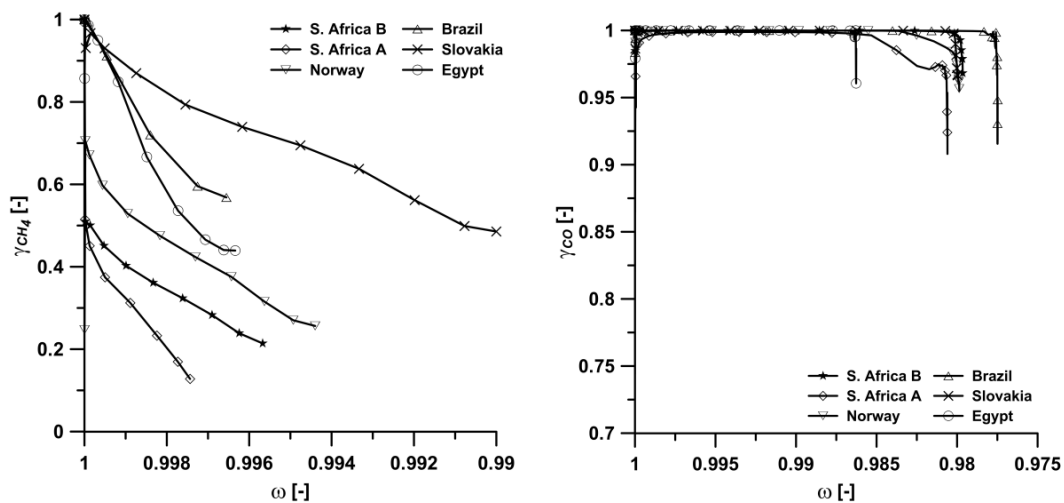


Figure 3.11 Gas yield,  $\gamma_{CH_4}$  and  $\gamma_{CO}$ , as a function of oxygen carrier mass-based conversion,  $\omega$ , for the manganese ores at 950°C using (left) methane, , and (right) 50% CO in H<sub>2</sub> as the fuel.

$\gamma_{CH_4} < 1$ . The Slovakian manganese ore had the highest and the South African B manganese ore had the lowest reactivity towards methane. In Figure 3.11 (right), it can be seen that for 50% CO in  $H_2$ , close to all of the fuel was converted for all of the manganese ores. On average, the manganese ores lose approximately 2% of their mass as they are converted during 80 s of reduction when using 50% CO in  $H_2$ , i.e.  $\omega$  goes from 1 to 0.98.

Figure 3.12 shows the total gas yield,  $\gamma_{CH_4,tot}$ , as a function of temperature for the investigated manganese ores using methane as the fuel and for the third repeated cycle. In all cases, the total gas yield for methane rose with temperature.

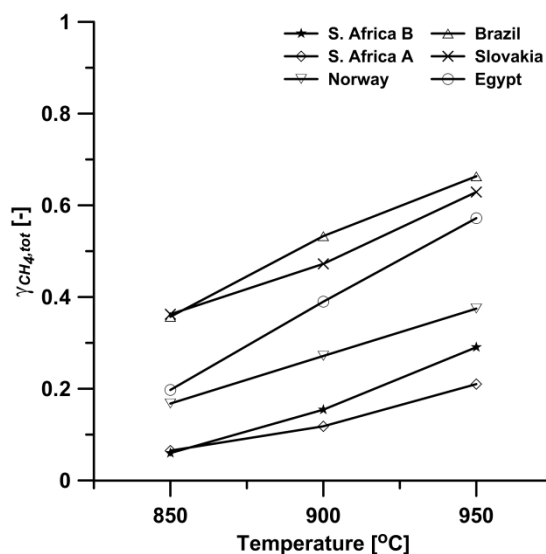


Figure 3.12 Total gas yield,  $\gamma_{CH_4,tot}$ , as a function of temperature for the manganese ores using methane as the fuel.

### 3.3 Standard Enthalpy of Formation, $\Delta H_f^0$ , of $CuAl_2O_4$ (Paper III)

The standard Gibbs free energy data,  $\Delta G^0$  of the Cu–Al–O system was first determined by Gadalla and White<sup>145</sup> using thermogravimetric analysis by measuring the dissociation temperatures of the compounds in the CuO–Al<sub>2</sub>O<sub>3</sub> system under different oxygen partial pressures, ranging from 0.21 to 1 atm. Later, Jacob and Alcock<sup>39</sup> investigated the standard Gibbs free energy,  $\Delta G^0$  of the formation of two ternary oxides (CuAl<sub>2</sub>O<sub>4</sub> and CuAlO<sub>2</sub>) in the range of 700–900°C using a solid-state galvanic cell. The thermodynamic data for the Cu–Al–O system have been tabulated in two thermodynamic databases, namely the Landolt–Brönstein database<sup>146</sup> and Knacke et al.<sup>147</sup>

Table 3.2 summarizes the standard enthalpy of formation,  $\Delta H_f^0$ , of CuAl<sub>2</sub>O<sub>4</sub> reported in these databases, in the literature and in this work. The data for standard enthalpy of formation,  $\Delta H_f^0$ , of CuAl<sub>2</sub>O<sub>4</sub> reported by Knacke et al.<sup>147</sup> has been taken from the study by Jacob and Alcock,<sup>39</sup> after being adjusted to the eutectoid formation temperature (617°C). However, the counterpart data reported in the Landolt–Brönstein database is considerably larger and is obtained from the Scientific Group Thermodata Europe (SGTE).<sup>146</sup> The discrepancy between the data reported by Landolt–Brönstein<sup>146</sup> and Knacke et al.<sup>147</sup> of approximately 134.5 kJ/mol is large enough to greatly influence

**Table 3.2 Summary of the standard enthalpy of formation,  $\Delta H_f^0$ , of  $CuAl_2O_4$  reported in different thermodynamic databases, studies and in this work.**

Standard enthalpy of formation, $\Delta H_f^0$ , of $CuAl_2O_4$ [kJ/mol]				
The Landolt–Brönstein database <sup>146</sup>	Knacke et al. <sup>147</sup>	Jacob and Alcock <sup>39</sup>	Gadalla and White <sup>145</sup>	This study
–1946.8	–1822.5	–1813.1	–1801.4	–1824.4±4.1

### 3. RESULTS AND DISCUSSION

the calculated reaction enthalpy of  $\text{CuAl}_2\text{O}_4$  with reducing gases, or the prediction of its formation in a mixture of  $\text{CuO}$  and  $\text{Al}_2\text{O}_3$  oxides at high temperatures. As an example, the standard enthalpy of reaction,  $\Delta H_r^0$ , of  $\text{CuAl}_2\text{O}_4$  with methane was reported to be endothermic and calculated as 282.2 kJ/mol,<sup>22</sup> based on the data from Landolt–Börnstein.<sup>146</sup> However, experimental observations in Papers I and II for the reduction of  $\text{CuAl}_2\text{O}_4$  with methane at 900–950°C, have instead shown a strongly exothermic reaction, see Figure 3.6, and the standard reaction enthalpy,  $\Delta H_r^0$ , was calculated as –252.0 kJ/mol, based on the data from Jacob and Alcock.<sup>39</sup>

As a result of the aforementioned discrepancy, an experiment was made to reassess the standard enthalpy of formation,  $\Delta H_f^0$ , of  $\text{CuAl}_2\text{O}_4$  using differential scanning calorimetry (DSC) by determining the reaction enthalpy,  $\Delta H_r$ , of  $\text{CuAl}_2\text{O}_4$  with CO as per the following reaction:



Figure 3.13 shows the TG and DSC curves of the reduction of the  $\text{CuAl}_2\text{O}_4$  sample at 900°C for three experiments. The reaction enthalpy,  $\Delta H_r$ , of the  $\text{CuAl}_2\text{O}_4$  sample with CO at 900°C was obtained by integrating the area under the DSC curve during the reduction period. Thus, by accounting for the mass fraction of the  $\text{CuAl}_2\text{O}_4$  phase in the sample, i.e. 0.86, the reaction enthalpy,  $\Delta H_r$ , of pure  $\text{CuAl}_2\text{O}_4$  with CO at 900°C was estimated. Consequently, the standard reaction enthalpy,  $\Delta H_r^0$ , of  $\text{CuAl}_2\text{O}_4$  with CO can be obtained by taking into account the change in the heat capacity of the species in Eq. (3.1).<sup>147, 148</sup> Using the standard reaction enthalpy,  $\Delta H_r^0$ , obtained and the standard enthalpy of formation,  $\Delta H_f^0$ , of Cu,  $\text{Al}_2\text{O}_3$ , CO and  $\text{CO}_2$ <sup>147, 148</sup> with Hess's law, the standard enthalpy of formation,  $\Delta H_f^0$ , of  $\text{CuAl}_2\text{O}_4$  has been determined as  $-1824.4 \pm 4.1$  kJ/mol. The standard enthalpy of formation,  $\Delta H_f^0$ , of  $\text{CuAl}_2\text{O}_4$  obtained in this work shows good agreement with the thermodynamic database by Knacke et al.<sup>147</sup> Based on the standard enthalpy of formation,  $\Delta H_f^0$ , of  $\text{CuAl}_2\text{O}_4$  determined here, the standard reaction enthalpy,  $\Delta H_r^0$ , of  $\text{CuAl}_2\text{O}_4$  with methane has been

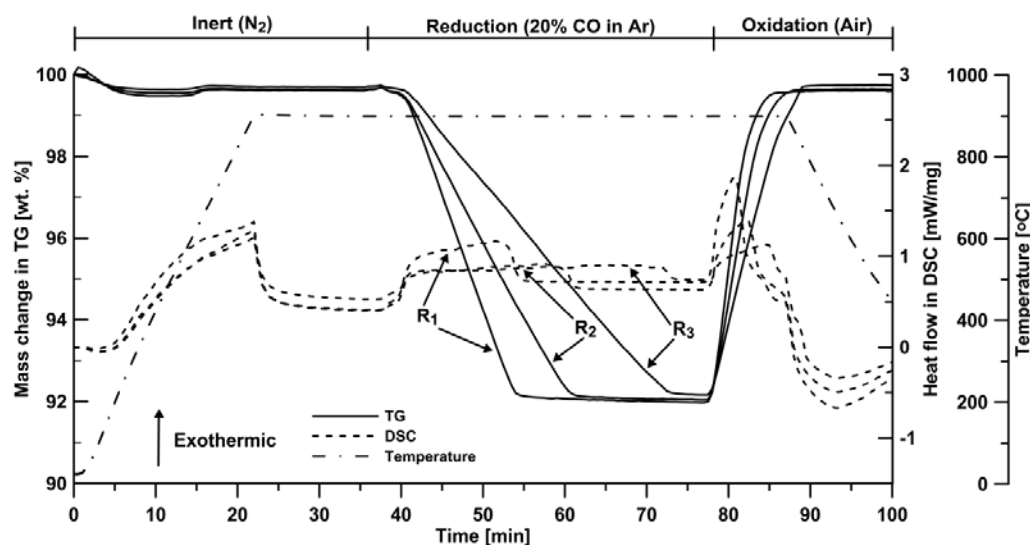


Figure 3.13 TG and DSC curves of the  $\text{CuAl}_2\text{O}_4$  sample heated in  $\text{N}_2$  to 900°C, followed by isothermal reduction in 20% CO in Ar and followed by oxidation and cooling in air for three experiments.

estimated to be  $-207.7$  kJ/mol, which corroborates the results presented in Figure 3.6 concerning the exothermic nature of this reaction.

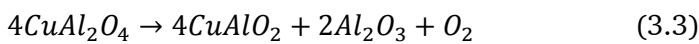
### 3.4 Phase Analysis of the Cu–Al–O System During Redox Cycle in CLC (Papers I and II)

The relationship among the various phases in the pseudobinary CuO–Al<sub>2</sub>O<sub>3</sub> system is of great relevance to the use of Al<sub>2</sub>O<sub>3</sub>-supported CuO oxygen carriers in the CLC process. Of importance is the formation of the CuAl<sub>2</sub>O<sub>4</sub> spinel during calcination or redox cycling of the oxygen carrier at high temperatures (around 800–1000°C),<sup>149–152</sup> as per the reaction:



As a result of the chemical-looping process, the phase field in the Cu–Al–O system becomes dependent on the oxygen partial pressure during the redox cycle in the temperature range of relevance. Figure 3.14 shows the equilibrium phase relationships at 1 atm total pressure using the Gibbs free energy data reported by Jacob and Alcock.<sup>39</sup>

In the context of the envisaged application of Al<sub>2</sub>O<sub>3</sub>-supported CuO oxygen carriers in continuous operation, other reactions in addition to those depicted in Figure 3.14 should be also considered. Figure 3.15 shows a series of  $P_{\text{O}_2}$ -dependent reactions in the temperature range of interest for CLC at a total pressure of 1 atm. The equilibrium lines shown in Figure 3.15 were also based on the Gibbs energy data of Jacob and Alcock.<sup>39</sup> Among these, of particular interest is the following reaction:



Reaction (3.3) indicates that CuAl<sub>2</sub>O<sub>4</sub> could potentially be a CLOU material by releasing O<sub>2</sub>, albeit at lower equilibrium partial pressure than CuO–Cu<sub>2</sub>O at temperatures above 900°C. Tsuboi et al.<sup>153</sup> have reported that at 1050°C, CuAl<sub>2</sub>O<sub>4</sub> undergoes reduction into CuAlO<sub>2</sub> in the case of thin copper films

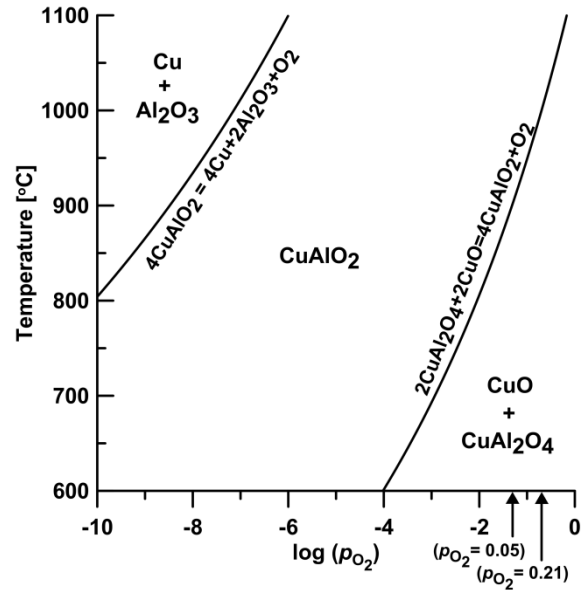


Figure 3.14 Equilibrium phase relationships in the ternary Cu–Al–O system in a 1:1 molar mixture of Cu and Al at 1 atm total pressure based on the Gibbs energy data reported by Jacob and Alcock.<sup>39</sup>

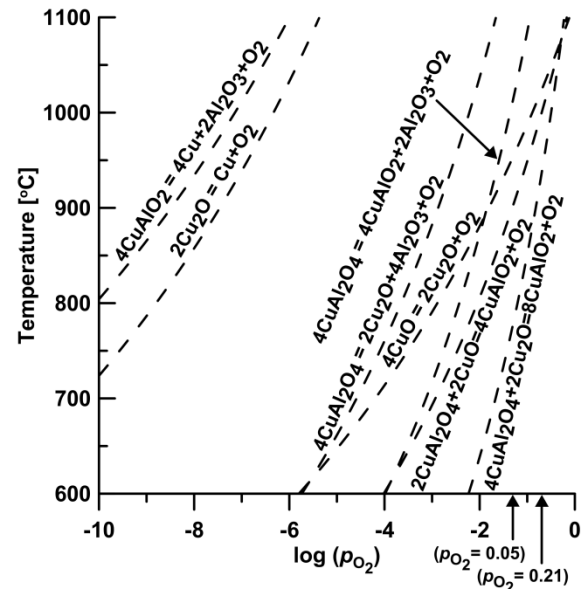


Figure 3.15 Possible  $P_{\text{O}_2}$ -dependent phase equilibria in the Cu–Al–O system at 1 atm total pressure based on the Gibbs energy data reported by Jacob and Alcock.<sup>39</sup>

### 3. RESULTS AND DISCUSSION

deposited on alumina substrate in a highly oxygen depleted vacuum. However, additional experiments in Paper I indicated that  $\text{CuAl}_2\text{O}_4$  subjected to a  $\text{N}_2$ -purge for 4 h at  $900^\circ\text{C}$  was incapable of releasing oxygen; no  $\text{CuAlO}_2$  could be observed either. On the other hand, it is well-established that  $\text{CuAl}_2\text{O}_4$  can be reduced by methane or syngas.<sup>43-45, 49, 50</sup> Thermogravimetric and temperature programmed reduction (TPR) studies<sup>49, 154-156</sup> on bulk samples also corroborate this. Thus, the observation of Tsuboi et al.<sup>153</sup> could perhaps be explained on the basis of the higher temperature than the study here, and the ease with which thin film samples undergo dissociation, compared to bulk samples such as those investigated here.

In order to understand the reducing and oxidizing pathways in the Cu–Al–O system and to analyse the reversibility of the phases during the redox process, the  $\text{CuAl}_2\text{O}_4$  (C4A-1050) oxygen carrier was further investigated. Figure 3.16 shows the XRD pattern of  $\text{CuAl}_2\text{O}_4$  subjected to isothermal step-wise reduction using methane at  $900^\circ\text{C}$  in a sequence of varying durations. Peaks belonging to  $\text{Cu}_2\text{O}$  appear in the sample reduced for the shortest duration (10 s). Longer (16 and 24 s) reduction is followed by a decrease in intensity, and consequently the amount of  $\text{CuAl}_2\text{O}_4$ , and an increase in intensity of  $\text{CuAlO}_2$  and  $\text{Cu}_2\text{O}$ . It should be

pointed out that in Paper I,  $\text{Cu}_2\text{O}$  was also seen during annealing in an inert environment, which was ascribed to the presence of a small amount of unreacted  $\text{CuO}$  in the fresh sample. A similar explanation is valid for the experiments here. However, the increase in the amount of  $\text{Cu}_2\text{O}$  seen in the diffraction patterns at 16 and 24 s in Figure 3.16, suggests that  $\text{Cu}_2\text{O}$  is not only formed from remnant  $\text{CuO}$  in the  $\text{CuAl}_2\text{O}_4$  oxygen carrier. Using TPR, Patrick et al.<sup>155, 156</sup> have shown that the reduction of  $\text{CuAl}_2\text{O}_4$  catalyst proceeds by the simultaneous formation of  $\text{CuAlO}_2$  and  $\text{Cu}_2\text{O}$  via reactions (3.3) and (3.4), respectively.



The formation and increase in amounts of  $\text{CuAlO}_2$  and  $\text{Cu}_2\text{O}$  via reactions (3.3) and (3.4), respectively, after 16 and 24 s in Figure 3.16 is also in agreement with the  $P_{\text{O}_2}$ –dependency shown

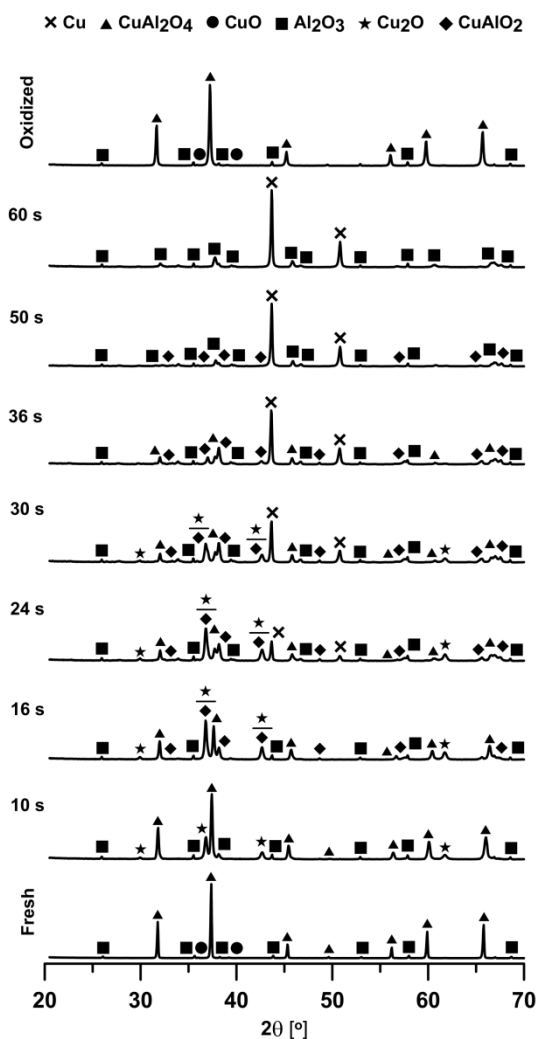
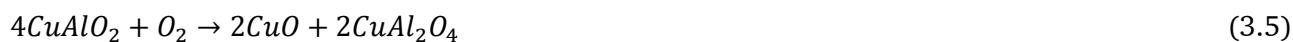


Figure 3.16 Systematic phase evolution in  $\text{CuAl}_2\text{O}_4$  oxygen carrier reduced by methane at  $900^\circ\text{C}$  for 60 s; the topmost XRD pattern is for the oxygen carrier oxidized in 10%  $\text{O}_2$  stream after being reduced for 60 s with methane.

in Figure 3.15, given the highly reducing environment created by methane. In the sample reduced for 24 s, the onset of the formation of elemental Cu was easily detected. The copper concentration increased with the time of reduction, as is evident from all of the diffraction patterns at  $t \geq 24$  s. In the case of reduction carried out for more than 36 s, the XRD pattern contains peaks for alumina and elemental copper with traces of delafossite ( $\text{CuAlO}_2$ ). In the samples reduced for 60 s, only metallic copper and alumina were present. This again is in complete conformity with Figures 3.14 and 3.15 in regard to the ultimate reduction of  $\text{CuAl}_2\text{O}_4$  to Cu and  $\text{Al}_2\text{O}_3$  as also reported elsewhere.<sup>156, 157</sup> Thus, the oxygen carrier was completely reduced by methane in 60 s. The intensity of the  $\alpha\text{-Al}_2\text{O}_3$  should increase during the consecutive reduction steps as it is formed from the  $\text{CuAl}_2\text{O}_4$ , however Figure 3.16 does not show this. A possible explanation for this may be that the alumina was still covered with the copper layer. The original phases ( $\text{CuAl}_2\text{O}_4$  and  $\text{Al}_2\text{O}_3$ ) were fully restored upon oxidation in 10%  $\text{O}_2$  as seen from the topmost XRD pattern in Figure 3.16.

From the foregoing discussion and the reactivity test presented in Sections 3.2, it is apparent that the  $\text{CuAl}_2\text{O}_4$  spinel functions well as an oxygen carrier. However, in a realistic CLC unit, the oxygen carrier is only partially reduced in order to avoid unconverted  $\text{CH}_4$ , CO and  $\text{H}_2$ . Recently, Kumekawa et al.<sup>158</sup> have shown that  $\text{CuAlO}_2$  is thermodynamically stable in air above 900–1000°C, which agrees reasonably with Figures 3.14 and 3.15. However, below this temperature range,  $\text{CuAlO}_2$  undergoes the following kinetically hindered reactions<sup>33, 36, 39</sup>



To investigate the kinetic aspect of reactions (3.5) and (3.6), oxygen carrier samples from the reactivity test consisting of alternating reduction (with methane) and oxidation at 900°C, albeit with a shorter reduction span (20 s) similar to that explained in Section 3.2, were used. Here, 1 g of the used sample (oxidized), which contained a considerable fraction of  $\text{CuAlO}_2$ , was re-oxidized in consecutive steps of 30 min in streams containing 5, 10, 15 and 21%  $\text{O}_2$  at 900°C. Figure 3.17 shows the phase evolution in each of the re-oxidation steps. To begin with, the oxidized sample

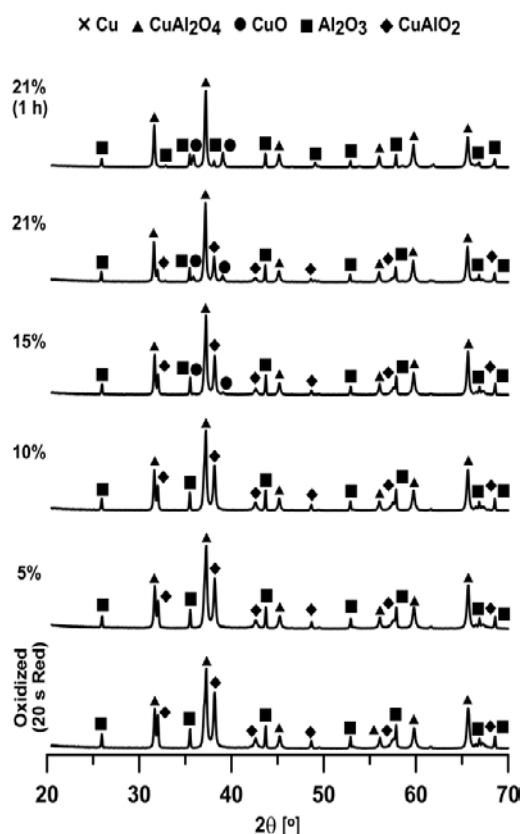


**Figure 3.17** Systematic phase evolution in  $\text{CuAl}_2\text{O}_4$  oxygen carrier during re-oxidation for 30 min in  $P_{\text{O}_2} = 5, 10, 15$  and 21%  $\text{O}_2$  streams at 900°C; the bottommost XRD pattern is for the oxidized sample from the reactivity test with shorter reduction span (20 s; methane); the topmost XRD pattern is for the sample re-oxidized in air (21%  $\text{O}_2$ ) for an additional 1 h.

from the reactivity test with a shorter reduction span (20 s; methane) contained a 3-phase mixture of  $\text{CuAl}_2\text{O}_4$ ,  $\text{CuAlO}_2$  and  $\text{Al}_2\text{O}_3$ . As is evident from the figure,  $\text{CuAlO}_2$  persisted under several re-oxidation attempts, indicating that the oxidation of  $\text{CuAlO}_2$  according to reaction (3.5) and/or (3.6) was kinetically hindered. This is further exemplified by the fact that complete conversion of the delafossite phase into the parent spinel ( $\text{CuAl}_2\text{O}_4$ ) was realized only after extended oxidation in air ( $P_{\text{O}_2} = 21\%$ ) at  $900^\circ\text{C}$  for an additional 1 h, i.e. a total of 3 h in varying oxygen concentrations. The increase in the CuO amount in the fully re-oxidized sample (topmost XRD pattern in Figure 3.17) compared to the fresh oxygen carrier (bottommost XRD pattern in Figure 3.16), is in agreement with reaction (3.5). It should be noted that in an actual CLC unit air is used for the oxidation of the depleted oxygen carrier; however the oxygen concentration at the outlet of the air reactor is much lower than 21%. Therefore part of the  $\text{CuAlO}_2$  phase resists oxidation.

### 3.5 Sulphur Tolerance of Perovskite-type Oxygen Carriers for CLOU (Paper V)

In this section, the influence of  $\text{SO}_2$  on oxygen release ability and the reactivity of the spray-dried perovskite-type materials are presented. As shown in Figure 3.18, in inert periods following reduction in the presence of  $\text{SO}_2$ , the average oxygen concentrations were considerably lower than the inert periods following reduction in the absence of  $\text{SO}_2$  (Figure 3.3), for undoped and Mg-doped materials. Thus, it can be inferred that  $\text{SO}_2$  had degraded the oxygen uncoupling properties of these materials. In the case of materials doped with both Mg and Ti materials, there was no substantial difference in the average oxygen concentration following reduction in the presence of  $\text{SO}_2$ .

Figure 3.19 shows the concentration and temperature profiles for C43MMg during the fifth fuel cycle with 50%  $\text{CH}_4$  and 0.5%  $\text{SO}_2$ -balance  $\text{N}_2$  at  $1000^\circ\text{C}$ . It can be seen that only a small fraction of  $\text{SO}_2$  passed through the reactor during the reduction period, whereas in the following inert and oxidation periods, more  $\text{SO}_2$  was detected in the off-gas. Possible mechanisms for the reaction of sulphur with the investigated perovskite-structured materials are discussed in the following. The first possible mechanism could be that CaS was formed during the reduction period via similar

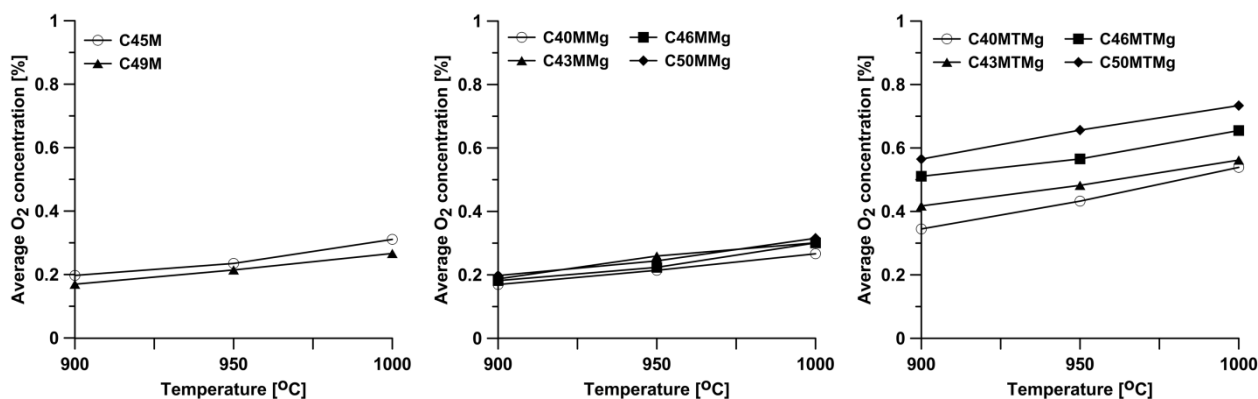


Figure 3.18 Average oxygen concentration as a function of temperature during inert cycles for various spray-dried perovskite-type oxygen carriers following fuel cycles using 50%  $\text{CH}_4$  and 0.5%  $\text{SO}_2$ -rest  $\text{N}_2$  at 900, 950 and  $1000^\circ\text{C}$ .

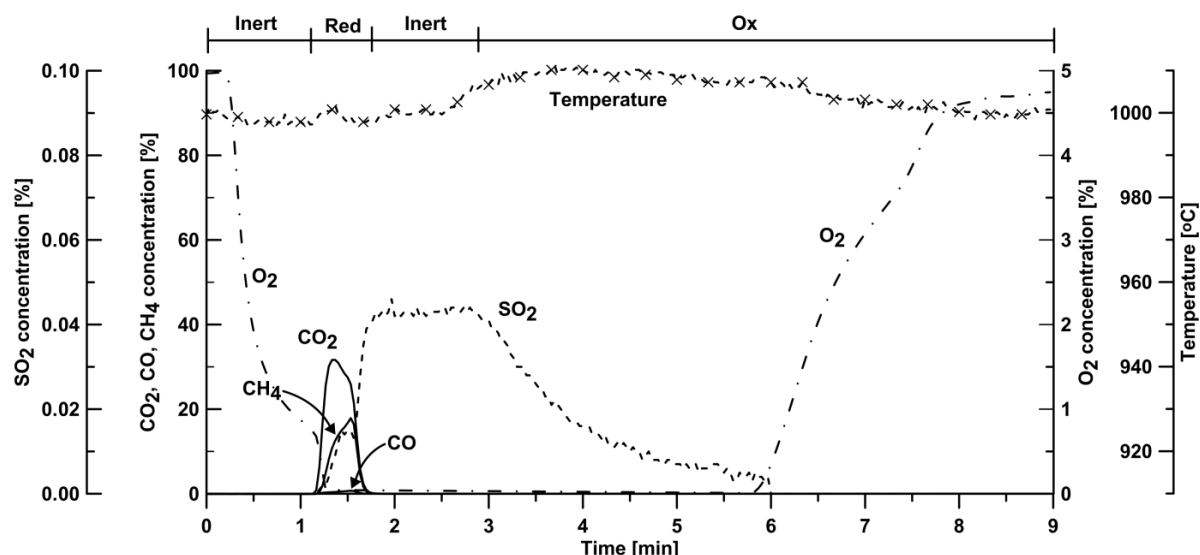


Figure 3.19 Concentration and temperature profiles for  $\text{Ca}_{0.75}\text{Mn}_{0.90}\text{Mg}_{0.10}\text{O}_{3-\delta}$  (C43MMg) as bed material during the fifth fuel cycle with 50%  $\text{CH}_4$  and 0.5%  $\text{SO}_2$ -rest  $\text{N}_2$  for 20 s at  $1000^\circ\text{C}$ .

reactions to Eq. (1.17) and (1.18), given the highly reducing potential of  $\text{CH}_4$ , in accordance with Figure 1.5. However, in the inert period following reduction,  $\text{SO}_2$  could be seen in the effluent as shown in Figure 3.19, despite the absence of any oxygen which could possibly oxidize  $\text{CaS}$  to  $\text{CaO}$  and  $\text{SO}_2$ , via reaction (1.9). This suggests that this mechanism cannot solely describe the formation of  $\text{SO}_2$  in the inert period subsequent to reduction, and instead,  $\text{CaSO}_4$  must be the source for the release of  $\text{SO}_2$ . A second possible mechanism could be that  $\text{CaS}$  reacted with  $\text{CaSO}_4$  via reaction (1.19) resulting in the formation of  $\text{SO}_2$ . This could be valid in later cycles when  $\text{CaSO}_4$  had already formed in the material during oxidation following methane cycles in the presence of  $\text{SO}_2$ . However, this was not the case, since a similar concentration profile for  $\text{SO}_2$ , as in Figure 3.19, was also seen in the inert period of the first methane cycle in the presence of  $\text{SO}_2$  at  $1000^\circ\text{C}$ , for which there was no  $\text{CaSO}_4$  in the material from the beginning. Nevertheless, it may be possible that both  $\text{CaS}$  and  $\text{CaSO}_4$  were formed during a reduction period. As shown in the early part of the reduction phase in Figure 3.19, some oxygen was present in the reactor, which could favour the formation of  $\text{CaSO}_4$ , while in the later part of the reduction  $\text{CaS}$  formation was more favoured due to the absence of oxygen, see Figure 1.5.

It is worth noting that even 4 h inert ( $\text{N}_2$ ) gas cycles for C45M following several methane cycles in the presence of  $\text{SO}_2$ , did not show any  $\text{SO}_2$  in the off-gas, which could indicate the spontaneous decomposition of  $\text{CaSO}_4$ . This indicates that a sufficiently reducing environment is required to allow  $\text{CaSO}_4$  to decompose. Thus, a third mechanism could be that the presence of a highly reduced bed material, e.g.  $\text{CaMnO}_2$  or  $\text{CaMnO}_{2.5}$ , following the reduction period, increases the reducing potential in the reactor in the subsequent inert period, thus enforcing the decomposition of  $\text{CaSO}_4$ . It is likely that the partial regeneration of the perovskite-type oxygen carriers occur via either the second or the third mechanism or a combination of both. Both mechanisms can be seen as the decomposition of  $\text{CaSO}_4$ , the reversed reaction (1.12) or (1.13), made possible by the presence of compounds that

### 3. RESULTS AND DISCUSSION

can readily react with any surplus of oxygen, e.g.  $\text{CaMnO}_2$ ,  $\text{CaMnO}_{2.5}$  or  $\text{CaS}$ . It can be speculated that such reactions could be facilitated by the high oxygen conductivity typical of perovskite-based materials.

Figure 3.20 shows the average gas yield,  $\gamma_{\text{CH}_4,ave}$ , and total  $\text{SO}_2$  yield,  $\eta_{\text{SO}_2}$ , as a function of temperature during fuel cycles in the presence of  $\text{SO}_2$  for C40MTMg at 900, 950 and 1000°C. It can be noted that there was a slight decrease in reactivity after every cycle. It was shown previously that a significant number of fuel cycles ( $\sim 30$ ) must be carried out in order to observe a significant decrease in reactivity due to sulphur deactivation.<sup>124</sup> However, carrying out such a large

number of cycles was outside the timeframe of this study, because of the large number of investigated materials. It can also be observed that at 1000°C, approximately 80% of the introduced  $\text{SO}_2$  passed through the reactor and was detected by the gas analyser. At 950°C this decreased to nearly 40% and at 900°C, only 10% of the introduced  $\text{SO}_2$  reached the gas analyser. Thus, it can be readily deduced that less  $\text{SO}_2$  was adsorbed to and/or reacted with the oxygen carrier with an increase in temperature. This is in accordance with Figure 1.5 given the fact that the stable region of  $\text{CaO}$  increased with temperature, meaning that the driving force for  $\text{CaSO}_4$  or  $\text{CaS}$  formation was weaker at high temperatures.

Figure 3.21 shows the total  $\text{SO}_2$  yield,  $\eta_{\text{SO}_2}$ , as a function of temperature during fuel cycles with 50%  $\text{CH}_4$  and 0.5%  $\text{SO}_2$  for all investigated materials at 900, 950 and 1000°C. Similar to Figure 3.20, it can be inferred that the amount of  $\text{SO}_2$  that passed through the reactor increased with an

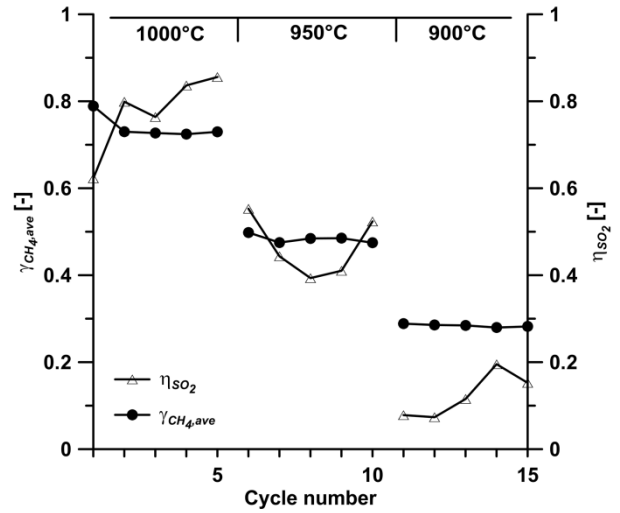


**Figure 3.20** Average gas yield,  $\gamma_{\text{CH}_4,ave}$  and total  $\text{SO}_2$  yield,  $\eta_{\text{SO}_2}$ , as a function of temperature during fuel cycles with 50%  $\text{CH}_4$  and 0.5%  $\text{SO}_2$ -rest  $\text{N}_2$  for  $\text{Ca}_{0.65}\text{Mn}_{0.90}\text{Mg}_{0.10}\text{O}_{3-\delta}$  (C40MTMg) as bed material at 900, 950 and 1000°C.

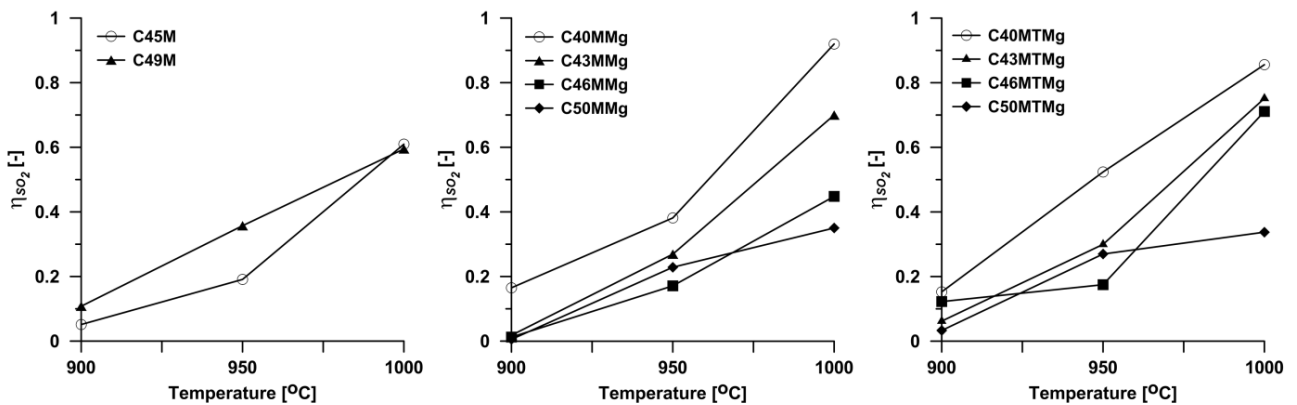


**Figure 3.21** Total  $\text{SO}_2$  yield,  $\eta_{\text{SO}_2}$ , as a function of temperature during fuel cycles for all investigated oxygen carriers using 50%  $\text{CH}_4$  and 0.5%  $\text{SO}_2$ -rest  $\text{N}_2$  at 900, 950 and 1000°C.

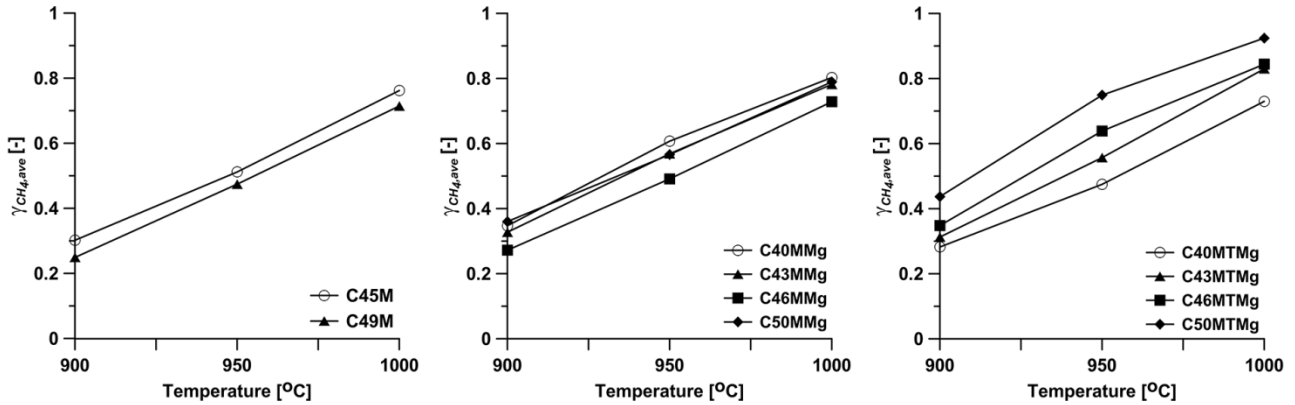


Figure 3.22 Average gas yield for  $\text{CH}_4$ ,  $\gamma_{\text{CH}_4,ave}$ , as a function of temperature during fuel cycles for all investigated oxygen carriers using 50%  $\text{CH}_4$  and 0.5%  $\text{SO}_2$ -rest  $\text{N}_2$  at 900, 950 and 1000°C.

increase in temperature. Moreover, the total  $\text{SO}_2$  yield,  $\eta_{\text{SO}_2}$ , increased with a decrease in the calcium content of the materials for both Mg- and Mg and Ti-doped materials. This may be expected since less calcium is available in the structure which could possibly result in the formation of  $\text{CaSO}_4$  or  $\text{CaS}$ . It should be mentioned however that this was not the case for the undoped materials.

Figure 3.22 shows the average gas yield,  $\gamma_{\text{CH}_4,ave}$ , as a function of temperature in the presence of  $\text{SO}_2$ . As indicated in Figure 3.20,  $\gamma_{\text{CH}_4,ave}$  decreased slightly with cycling during reactivity experiments in the presence of  $\text{SO}_2$  as a result of sulphur deactivation. Therefore, the presented  $\gamma_{\text{CH}_4,ave}$  in Figure 3.22 during reactivity testing in the presence of  $\text{SO}_2$  is representative of the gas yield of the last cycle at each temperature. It can be seen that in the experiments in the presence of  $\text{SO}_2$ , the drop in gas conversion for oxygen carriers with lower calcium content was less for the undoped and Mg-doped materials, than in the reactivity testing in the absence of  $\text{SO}_2$  as shown in Figure 3.9. Again this could be anticipated due to the lower chance for the formation of  $\text{CaSO}_4$  or  $\text{CaS}$  in samples with lower calcium content. This is also supported by their higher total  $\text{SO}_2$  yield,  $\eta_{\text{SO}_2}$ , as shown in Figure 3.21, as compared to materials with a higher calcium content. However, this was not the case for the doubly Mg and Ti-doped materials. Instead, for these materials, it was possible to maintain a lower drop in reactivity for materials with a higher calcium content, despite their lower total  $\text{SO}_2$  yield,  $\eta_{\text{SO}_2}$ , as shown in Figure 3.21. It is unclear at this point, whether this could be attributed to the substitution of the B-site with Ti in these materials, thus requiring additional study of the interaction of different perovskite-structured materials and sulphur species. However, it is clear that the reactivity had decreased in the presence of  $\text{SO}_2$  for all of the investigated oxygen carriers. The drop in reactivity increased at lower temperatures and was as large as 50% at 900°C, whereas at 1000°C, the largest decrease in reactivity was about 20%. This again could be ascribed to the lower thermodynamic favourability of  $\text{CaSO}_4$  or  $\text{CaS}$  formation at higher temperatures, as shown in Figure 1.5.

Since increasing the temperature had a more notable effect on decreasing the sulphur deactivation,

### 3. RESULTS AND DISCUSSION

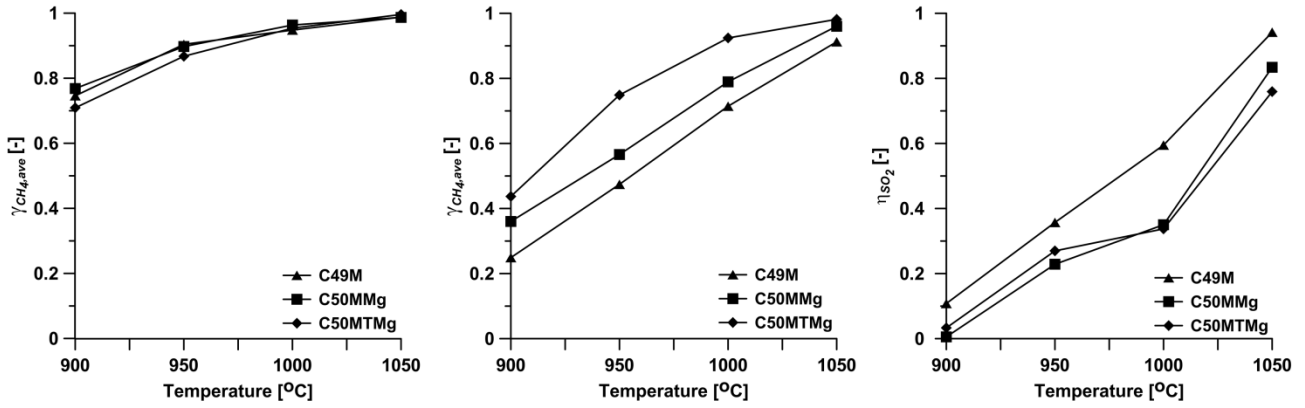


Figure 3.23 Average gas yield for  $\text{CH}_4$ ,  $\gamma_{\text{CH}_4,ave}$ , during fuel cycles for C49M, C50MMg and C50MTMg oxygen carriers using (left) 50%  $\text{CH}_4$ -rest  $\text{N}_2$  and (middle) 50%  $\text{CH}_4$  and 0.5%  $\text{SO}_2$ -rest  $\text{N}_2$  and (right) their respective total  $\text{SO}_2$  yield,  $\eta_{\text{SO}_2}$ , at 900, 950, 1000 and 1050°C.

additional experiments for the reactivity of three oxygen carriers were carried out at 1050°C, and the results are summarized in Figure 3.23. It could be observed that at 1050°C, the decrease in reactivity following the reduction in the presence of  $\text{SO}_2$  became minimal at only 1%. Furthermore, the doubly Mg- and Ti-doped material exhibited a lower decrease in reactivity in the presence of  $\text{SO}_2$  than the undoped and singly Mg-doped materials. The total  $\text{SO}_2$  yield,  $\eta_{\text{SO}_2}$ , at 1050°C could reach as high as 0.94. Experiments at even higher temperatures (e.g. 1100°C), could possibly result in a total  $\text{SO}_2$  yield,  $\eta_{\text{SO}_2}$ , of 1, and consequently entirely avoid any sulphur deactivation. However, it should be mentioned that a slight deactivation in the reactivity of  $\text{CaMn}_{0.9}\text{Mg}_{0.1}\text{O}_{3-\delta}$  (C50MMg) in the absence of  $\text{SO}_2$  has been reported at 1050°C,<sup>105</sup> which could become more severe at 1100°C.

Figure 1.5 also indicates that the perovskite-type oxygen carrier may be regenerable since  $\text{CaSO}_4$  or  $\text{CaS}$  can decompose to  $\text{CaO}$  and  $\text{SO}_2$ , where  $\text{CaO}$  can react again with  $\text{Mn}_3\text{O}_4$  and reconstruct the  $\text{CaMnO}_{3-\delta}$  phase. Here, the C45M oxygen carrier which had already been subjected to 43 fuel cycles in the presence of  $\text{SO}_2$  and thus its reactivity had decreased substantially compared to experiments in the absence of  $\text{SO}_2$  was used to investigate the possibility for regeneration. Figure 3.24 shows the  $\gamma_{\text{CH}_4,ave}$  as a function of cycle number at 1000°C in different conditions. The experiment consisted of seven fuel cycles with a considerably longer second inert period (~40 min) in the absence of  $\text{SO}_2$ . The rationale for using a longer second inert period was to decompose as much  $\text{CaSO}_4$  as possible. It can be observed that

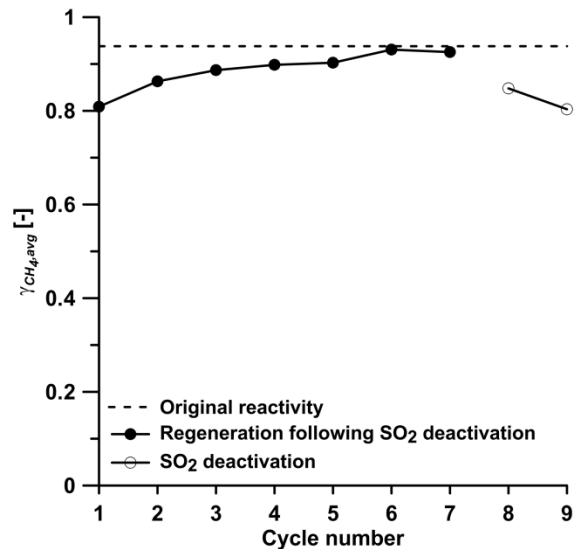


Figure 3.24 Average gas yield for  $\text{CH}_4$ ,  $\gamma_{\text{CH}_4,ave}$ , as a function of cycle number for  $\text{Ca}_{0.83}\text{MnO}_{3-\delta}$  (C45M) at 1000°C during regeneration and following sulphur deactivation of the oxygen carrier.

the  $\gamma_{CH_4,ave}$  increased to approximately that of the experiment without the presence of  $SO_2$  from the beginning, thus showing that the oxygen carrier could be regenerated. Similar observations have been reported for the partial regeneration of  $LaFe_{0.8}Cu_{0.2}O_3$  catalysts in 5%  $H_2$  in Ar.<sup>120</sup> When  $SO_2$  was included in the reduction period, see cycles 8 and 9, the reactivity towards methane decreased again.

### 3.6 Rate of Oxygen Release from Copper-based and Perovskite-type Oxygen Carriers for CLOU (Papers VI and IV)

In Paper VI, the rate of oxygen release of an oxygen carrier for the CLOU process was investigated. The experiments were designed in a way to avoid the equilibrium oxygen restriction and obtain a relevant rate of oxygen release as described in Section 2.2. The  $MgAl_2O_4$ -supported  $CuO$  oxygen carrier (C4MA-950) had shown stable chemical-looping properties for seventeen cycles in Paper I and was therefore considered suitable for this experiment.

The concentration profile measured during reduction at 900°C is shown as an example in Figure 3.25. The deconvoluted in-reactor concentrations obtained from the mass-balance over the reactor system is also included in the figure. The spontaneous decomposition of  $CuO$  during the 30 s inert span prior to the introduction of 0.1 g of the devolatilized wood char is confirmed by the release of oxygen which is consistent with the equilibrium oxygen release concentration for  $CuO$  oxygen carriers (Figure 1.4). Peaks of  $CH_4$ ,  $CO$  or  $H_2$  could not be seen during the introduction of fuel, which confirmed that the wood char was free of volatiles. This indicates that the fuel reacted with the gaseous oxygen released, producing  $CO_2$ . Note that the temperature was almost constant during the reduction phase, thus it is reasonable to assume isothermal conditions. Since the amount of fuel introduced (0.1 g) exceeded the carbon stoichiometric demand of the oxygen carrier which it can provide oxygen for during conversion of  $CuO$  to  $Cu_2O$  (0.012 g), the oxygen partial pressure dropped rapidly to approximately zero in less than a few seconds. The burn-off of the remaining carbon during the subsequent oxidation phase of every cycle confirmed the excess of carbon in the bed. The amount of carbon converted during the reduction was approximately 0.012 g which corroborates the stoichiometric carbon need for the reduction of  $CuO$  to  $Cu_2O$  in the oxygen carrier, and was almost constant in the different cycles. Although solid-solid reactions between the fuel and the oxygen carrier particles is possible,<sup>159</sup> it is very unlikely that such reactions are fast enough to affect these

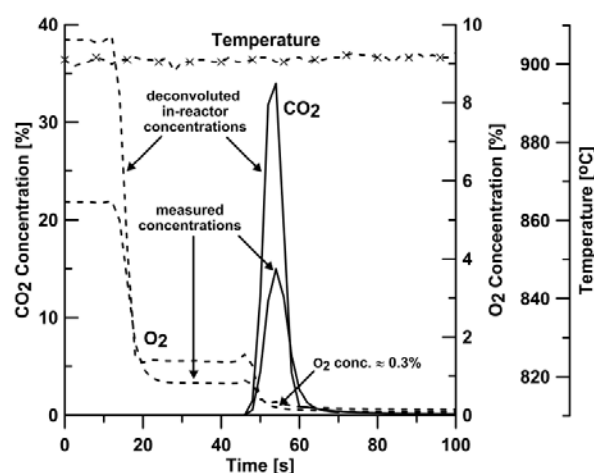


**Figure 3.25** Measured and deconvoluted (in-reactor) concentrations and temperature profile during oxygen release (reduction) cycle at 900°C using 1 g of  $CuO/MgAl_2O_4$  oxygen carrier in 10 g of quartz and 0.1 g of devolatilized wood char.

### 3. RESULTS AND DISCUSSION

measurements given the experimental conditions employed, i.e. a fluidized-bed reactor. Higher amounts of fuel (0.2 and 0.3 g) were also introduced to the bed in order to observe the rate of decrease in the oxygen concentration, and possibly achieve higher rates of oxygen release by the oxygen carrier. However, the concentration profiles were similar for the cases in which 0.1 g and 0.3 g of the fuel were added during reduction, indicating that the rate of reduction remained constant when using higher amounts of fuel. Therefore the addition of 0.1 g of the devolatilized wood char to a bed of 1 g of  $\text{CuO}/\text{MgAl}_2\text{O}_4$  oxygen carrier mixed in 10 g of quartz gives an adequately oxygen-deficient and isothermal condition inside the reactor to allow for the measurement of the maximum possible rate of oxygen release from the carrier. The general trend in  $\text{CO}_2$  and  $\text{O}_2$  concentration profiles seen in Figure 3.25 was similar at different temperatures. The oxygen release prior to the introduction of the fuel and the maximum  $\text{CO}_2$  concentration at the outlet of the reactor was essentially the only difference at the different investigated temperatures.

Figure 3.26 shows the conversion of the oxygen carrier as a function of time during reduction,  $X_{red}$ , in the temperature range of 850–900°C. The 30 s span before the introduction of the devolatilized wood char during the reduction of the oxygen carrier shown in Figure 3.26 was to allow the conditions in the reactor to reach close to equilibrium oxygen concentration and to avoid back-mixing from the previous oxidation. It is clear that the conversion of the oxygen carrier was slow during this time because the conditions in the reactor were close to thermodynamic equilibrium owing to the oxygen released. Upon insertion of the fuel, the oxygen surrounding the oxygen carrier was removed almost immediately, and the oxygen carrier released the remaining oxygen at the maximum rate possible. This resulted in the sudden increase in the rate of conversion of the oxygen carrier. The oxygen carrier was completely reduced to  $\text{Cu}_2\text{O}$  at 900°C. At lower temperatures however, the initial rate of reaction appears to have been slower, as seen from the slope of the plots in Figure 3.26 which means that the conversion,  $X_{red}$ , had not reached unity at the end of the reduction period.

In order to model the oxygen release, i.e. the decomposition of  $\text{CuO}$  to  $\text{Cu}_2\text{O}$  shown in Eq. (1.7), it was assumed that the experiments were conducted within the kinetically controlled regime, given oxygen being efficiently consumed by the devolatilized wood char. For details of the implication of such an assumption and its validation, see Paper VI. To determine which kinetic model best

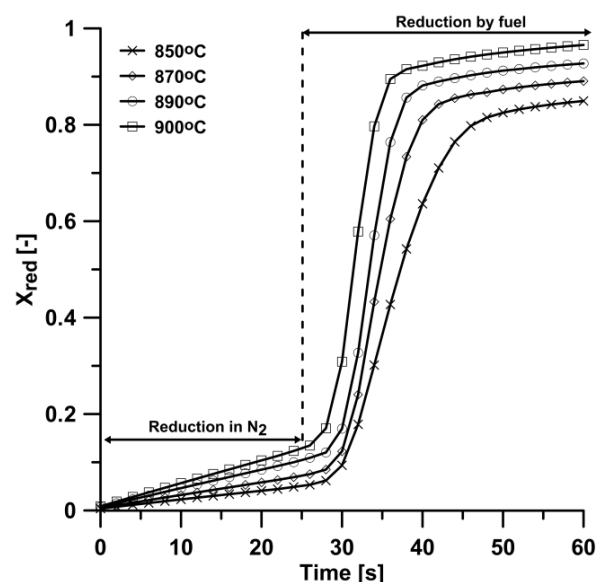


**Figure 3.26** Oxygen carrier conversion during oxygen release (reduction) period,  $X_{red}$ , as a function of time for 1 g of  $\text{CuO}/\text{MgAl}_2\text{O}_4$  in 10 g of quartz in the temperature range of 850–900°C using 0.1 g of devolatilized wood char.

describes the progress of reaction (1.7), common gas-solid reaction kinetic models were fit to the conversion,  $X_{red}$ , versus time data in Figure 3.26, including reaction order models, nucleation models, diffusion models and geometrical contraction models.<sup>160</sup> The results of the fitting of the different kinetic models are also presented in Paper VI. Of all the investigated models, the Avrami-Erofeev mechanism which assumes a two-dimensional nuclei growth ( $n = 2$ ) was found to describe the decomposition reaction best, with the coefficient of variance,  $R^2$ , of approximately 0.986. The rate equation for such a reaction model can be written as

$$\frac{dX_{red, norm}}{dt} = k_r 2(1 - X_{red, norm}) [-\ln(1 - X_{red, norm})]^{\frac{1}{2}} \quad (3.7)$$

where  $k_r$  is the rate constant of the forward reaction in Eq. (1.7).  $X_{red, norm}$  is the normalized measured conversion of the oxygen carrier shown in Figure 3.27 to obtain full conversion of the carrier. Figure 3.27 also shows the results of modelling the oxygen carrier conversion during oxygen release (reduction) using this model. The sigmoidal shape of the oxygen carrier conversion,  $X_{red, norm}$ , as a function of time shown in Figure 3.27 further indicates that the decomposition reaction, Eq. (1.7), proceeded via nucleation and nuclei growth.<sup>160</sup> Similar results have also been found for gas-solid reactions of CuO oxygen carriers<sup>50, 77</sup> and the decomposition of pure CuO powder.<sup>91</sup>

Figure 3.28 shows the derivative of the mass-based conversion,  $\frac{d\omega}{dt}$ , as a function of mass-based conversion,  $\omega$ , for the extruded perovskite-type oxygen carriers at 950°C. Similar to Figures 3.25 and 3.26, the non-variant regime of the plot during the first 60 s span before the introduction of fuel is indicative of the approach and establishment of near equilibrium conditions in the reactor with respect to oxygen concentration. Clearly, the reduction of the oxygen carrier was slow during this period. When

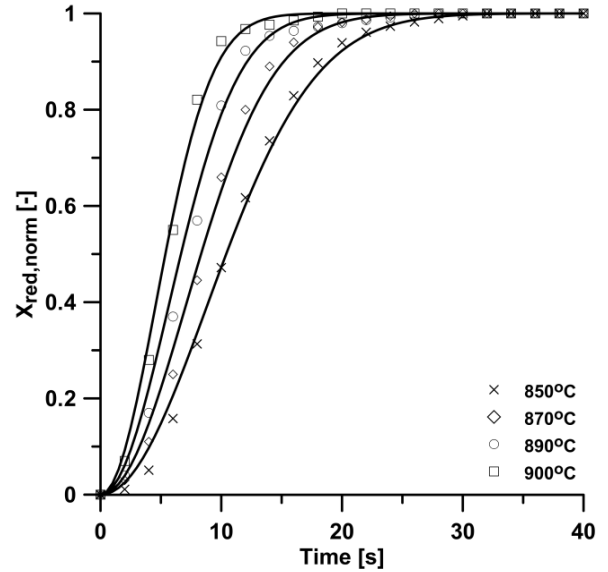


Figure 3.27 Normalized oxygen carrier conversion during oxygen release (reduction) cycle,  $X_{red, norm}$ , as a function of time and fitting of the Avrami-Erofeev model for 1 g of CuO/MgAl<sub>2</sub>O<sub>4</sub> in 10 g of quartz in the temperature range of 850–900°C using 0.1 g of devolatilized wood char.

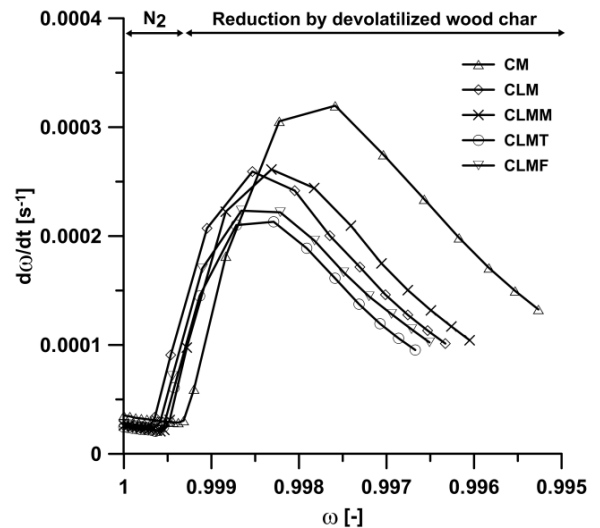


Figure 3.28 Variation of mass-based conversion derivative,  $\frac{d\omega}{dt}$ , with mass-based conversion,  $\omega$ , of the extruded perovskite-type oxygen carriers during conversion of 0.1 g of devolatilized wood char at 950°C (5 g sample in 10 g quartz).

fuel was added, the gaseous oxygen in the vicinity of the carrier was consumed by the fuel almost instantly. This again created a large chemical potential gradient, thus making the perovskite-structured materials release additional oxygen at the highest possible rate. This is supported by the sharp spike in the curves. Interestingly, CM and CLMT exhibited the highest and the lowest rate of oxygen release, respectively. It is also worth mentioning that the maximum oxygen release rate here ( $\sim 0.0002\text{--}0.0003\text{ 1/s}$ ) was about 20 times lower than that for 1 g of  $\text{MgAl}_2\text{O}_4$ -supported CuO ( $0.005\text{ 1/s}$ ) at  $900^\circ\text{C}$ . This was expected since it is well established that the rate of oxygen release for CuO-based carriers is very high. Although the rate numbers may appear low, it should be mentioned that they are based on total mass. Thus, a rate of  $0.005\text{ 1/s}$  means that oxygen corresponding to, for example, 2% of the mass is released in 4 s.

Figure 3.29 shows the variation of mass-based conversion,  $\omega$ , with time for the reduction with methane and 0.1 g of devolatilized wood char for the investigated extruded perovskite-type oxygen carriers. As can be seen, the amount of oxygen released by the CLOU mechanism was smaller than that available for reaction with gaseous fuels such as  $\text{CH}_4$  via the CLC process. This suggests that perovskite-based carriers are likely to react via a combination of CLC and CLOU mechanisms both; the relative extent of each of these would depend upon the degree of conversion of oxygen carrier in the reactor.

### 3.7 Rate of Oxidation of Copper-based Oxygen Carriers for CLOU (Paper VI)

Figure 3.30 shows the effect of the mass of the oxygen carrier on the derivative of conversion during oxidation,  $\frac{dX_{ox}}{dt}$ , for the  $\text{MgAl}_2\text{O}_4$ -supported CuO material following reduction in nitrogen. It can be seen that as the mass of the oxygen carrier was reduced from 4 to 1 g, while keeping the mass of the

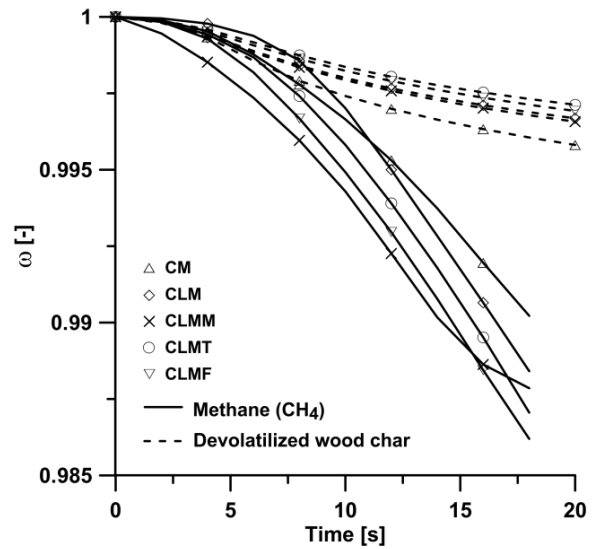


Figure 3.29 Variation of mass-based conversion,  $\omega$ , of the extruded perovskite-type oxygen carriers with time for reduction with methane and 0.1 g of devolatilized wood char at  $950^\circ\text{C}$ .

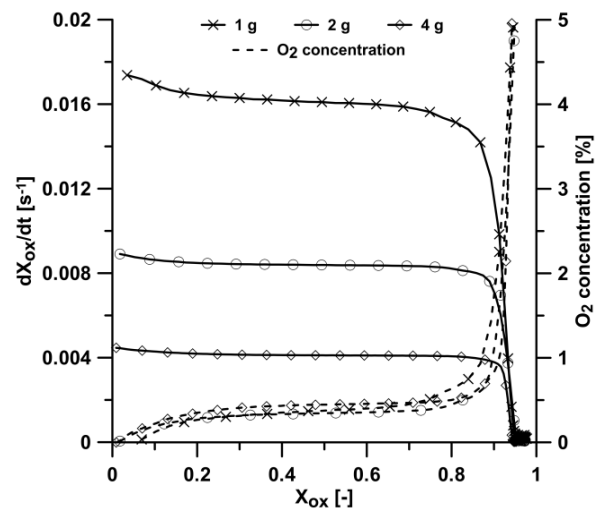


Figure 3.30 Oxygen carrier conversion derivative during oxidation cycle,  $\frac{dX_{ox}}{dt}$ , and oxygen concentration at the outlet of the reactor (not deconvoluted), as a function of oxygen carrier conversion,  $X_{ox}$ , for 1, 2 and 4 g of  $\text{MgAl}_2\text{O}_4$ -supported CuO oxygen carrier in 10 g of quartz at  $850^\circ\text{C}$  in 5%  $\text{O}_2$  stream.

quartz constant at 10 g, the initial reaction rate increased. Thus, even with a mass of 1 g of the oxygen carrier, the oxygen was rapidly consumed during the initial period of the oxidation phase. In addition, for all of these cases, the oxygen carrier was oxidized at the equilibrium partial pressure of oxygen (0.5%; Figure 1.4). These observations indicate that the rate of oxidation reaction was limited by the oxygen supply. This behaviour has also been observed previously by Mattisson et al.<sup>161</sup> for a Fe<sub>2</sub>O<sub>3</sub>-based oxygen carrier. Here, the mass of the oxygen carrier was also lowered to less than 1 g; however, it was observed that the resulting rates were extremely fast, with times shorter than the time needed for the oxygen containing gas to replace the reactor volume (15–20 s). Therefore, the determination of the oxidation rate was made using a bed mass of 1 g and thus the presented oxidation rates are only representative of the ‘minimum’ value possible to measure in this work due to the rapid oxidation reaction.

Figure 3.31 shows the derivative of the conversion of the MgAl<sub>2</sub>O<sub>4</sub>-supported CuO oxygen carrier during oxidation,  $\frac{dX_{ox}}{dt}$ , and the partial pressure of oxygen at the reactor’s outlet, with respect to the oxygen carrier conversion,  $X_{ox}$ . It can be seen that at any conversion degree, the derivative (reaction rate) was limited by the equilibrium oxygen concentration at each respective reaction temperature. Thus, the rapid oxidation reaction at all temperatures makes it difficult to obtain the rate of oxidation of Cu<sub>2</sub>O to CuO. As the oxygen carrier was exposed to a partial pressure of oxygen, the apparent rate equation during oxidation, assuming first-order dependency on a logarithmic average of oxygen concentration can be written as

$$\frac{dX_{ox}}{dt} = k_{-r} P_{O_2,ave} \quad (3.8)$$

Here,  $P_{O_2,ave}$  is based on the difference between actual oxygen concentration and the equilibrium oxygen concentration. Thus, the  $P_{O_2,ave}$  can be calculated as per Eq. (3.9),

$$P_{O_2,ave} = \frac{P_{O_2,in} - P_{O_2,out}}{\ln(P_{O_2,in} - P_{O_2,eq} / P_{O_2,out} - P_{O_2,eq})} \quad (3.9)$$

However, due to the fast oxidation reaction, the outlet partial pressure of oxygen is equal to equilibrium oxygen concentration at the respective temperature (Figure 3.31). This will give a value of  $P_{O_2,ave}$  of zero, and consequently  $k_{-r}$  will be infinite. Therefore, it is not possible to calculate a

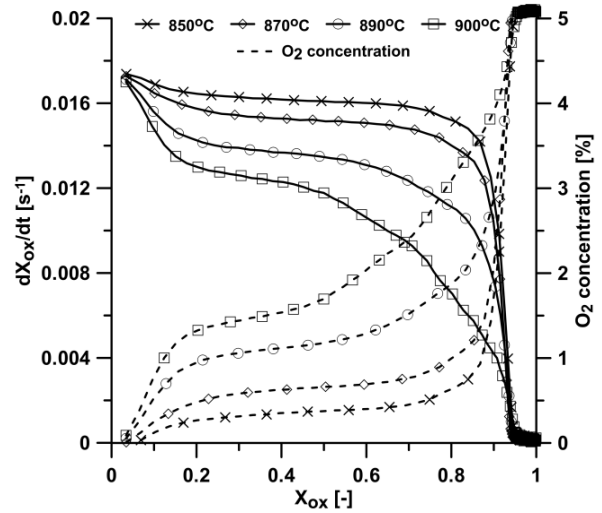


Figure 3.31 Oxygen carrier conversion derivative during oxidation cycle,  $\frac{dX_{ox}}{dt}$ , and the oxygen concentration (not deconvoluted) at the outlet of the reactor, as a function of oxygen carrier conversion,  $X_{ox}$ , for 1 g of oxygen carrier in 10 g of quartz for the temperature range of 850 to 900°C in 5% O<sub>2</sub> stream.

meaningful rate constant,  $k_{-r}$ , using Eq. (3.8) and (3.9). In order to obtain a “minimum value” of rate constant for the experiments in this work, an oxygen concentration of 1% is assumed at the outlet of the reactor in Eq. (3.9). As an example, the logarithmic average of the oxygen partial pressure,  $P_{O_2,ave}$ , is approximately 1.82% at 850°C assuming 5% O<sub>2</sub> at the inlet and 1% O<sub>2</sub> at the outlet of the air reactor. Therefore, using the corresponding value for  $\frac{dX_{ox}}{dt}$  in Figure 3.31, the minimum  $k_{-r}$  is estimated to be 0.89 1/s.atm at 850°C.

#### **3.8 Solids Circulation Rate and Inventory of Copper-based and Perovskite-type Oxygen Carriers for CLOU (Papers VI and IV)**

Using the reaction rates,  $k_r$  and  $k_{-r}$ , obtained in Sections 3.6 and 3.7, the amount of solids inventory needed for the CLOU process using the CuO/MgAl<sub>2</sub>O<sub>4</sub> (C4MA-950) oxygen carrier can be calculated. An oxygen carrier mass-based conversion difference,  $\Delta\omega$ , of 1–2% results in a recirculation rate of solids,  $\dot{m}_{OC}$ , between 4–8 kg/s.MW<sub>th</sub> for 1 MW<sub>th</sub> assuming carbon as a fuel with a lower heating value (LHV) of 32.8 MJ/kg.<sup>10</sup> This is also within the feasible range in a system of reactors similar to CFB boilers.<sup>162</sup> For details of the calculation method of the solids circulation rate and inventory, see Paper VI. Additionally, negligible mass transfer resistance between the bubbles and the emulsion phase in the fluidized-bed reactor and a first-order oxidation reaction with respect to oxygen concentration were assumed. Temperatures of 900 and 850°C were assumed for the fuel and the air reactor, respectively. Thus, the solids needed per MW<sub>th</sub> in the fuel reactor varied between 30–60 kg/MW<sub>th</sub> and in the air reactor between 43–87 kg/MW<sub>th</sub>, giving a total of 73–147 kg/MW<sub>th</sub>.

The required solids inventory in the fuel reactor obtained here was lower than both previously reported investigations for a 40 wt.% CuO on ZrO<sub>2</sub> support using petcoke as the fuel (120–200 kg/MW<sub>th</sub>)<sup>82</sup> and recent studies in continuous operation using a spray-dried 60 wt.% CuO on MgAl<sub>2</sub>O<sub>4</sub> support (235 kg/MW<sub>th</sub> at 960°C).<sup>35</sup> On the other hand, a lower value was obtained from batch fluidized-bed experiments for the spray-dried 60 wt.% CuO on MgAl<sub>2</sub>O<sub>4</sub> support (39 kg/MW<sub>th</sub> at 930°C),<sup>37</sup> the latter being closer to the results of this study.

The required solid inventory for the perovskite-based oxygen carriers in a fuel reactor operating at 950°C was estimated to be 325 kg/MW<sub>th</sub>, assuming an average  $R_O$  or  $\Delta\omega$  of 0.5% for the oxygen carriers and a solids circulation rate of 16 kg/s.MW<sub>th</sub>.

#### **3.9 Rate of Steam Gasification of Char for Manganese Ores in CLC (Papers VII and VIII)**

Figure 3.32 shows the dry gas concentrations for a reduction period at 970°C for the Egyptian manganese ore with petcoke and wood char as the fuel. The initial peaks of CH<sub>4</sub> and H<sub>2</sub> are due to devolatilization of the fuels. It is likely that devolatilization mainly occurred above the bed as the fuel particles were introduced at the top of the reactor, meaning that a large part of the volatiles

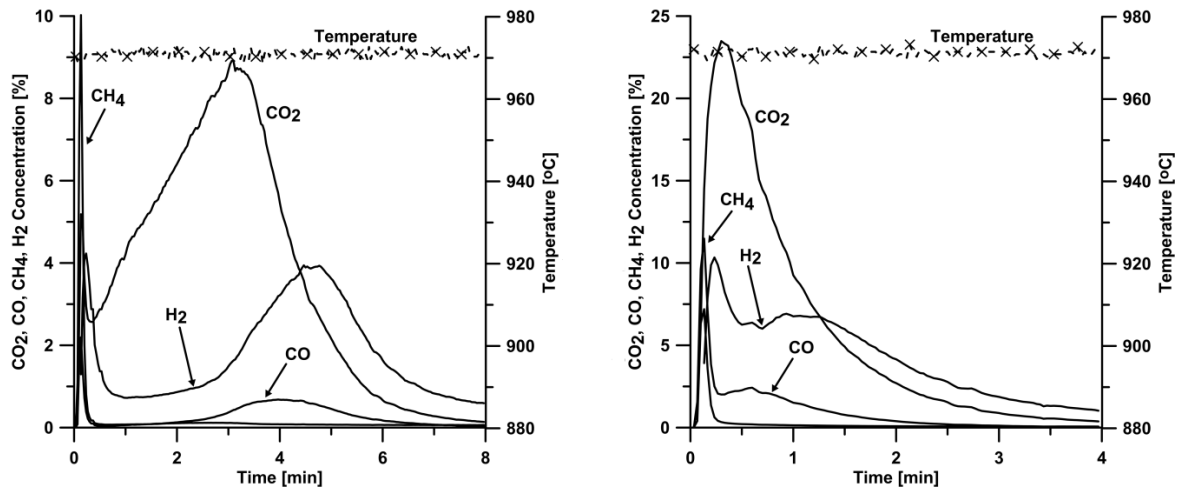


Figure 3.32 Dry gas concentration and temperature profiles at 970°C for reduction of Egyptian manganese ore using 0.1 g of (left) petcoke and (right) wood char as the fuel. The inlet gas was 50% H<sub>2</sub>O in N<sub>2</sub>.

had little opportunity to react with the oxygen carrier. The remaining char from both fuels then reacted with the steam to generate CO and H<sub>2</sub>, which the oxygen carrier converted to CO<sub>2</sub> and H<sub>2</sub>O. The trends in the concentration profiles between different bed materials were similar and only differed in time for complete conversion of the fuel.

Figure 3.33 shows the instantaneous rate of char conversion,  $r_{inst}$ , for the manganese ores as well as ilmenite and Mn-oxide oxygen carrier using petcoke (left) and wood char (right). For reasons of clarity, the fraction of carbon conversion,  $X_C$ , has been scaled to show only the conversion degrees from 0.3 to 0.7, where stable carbon conversion had been achieved. It can be noted that the gasification rate was higher for wood char than for petcoke. This is likely because wood char has a higher surface area and thus the cleavage of the carbon bonds by the gasifying agent (steam) was easier than in petcoke, which has a denser char structure. Thus for wood char, the rate of steam

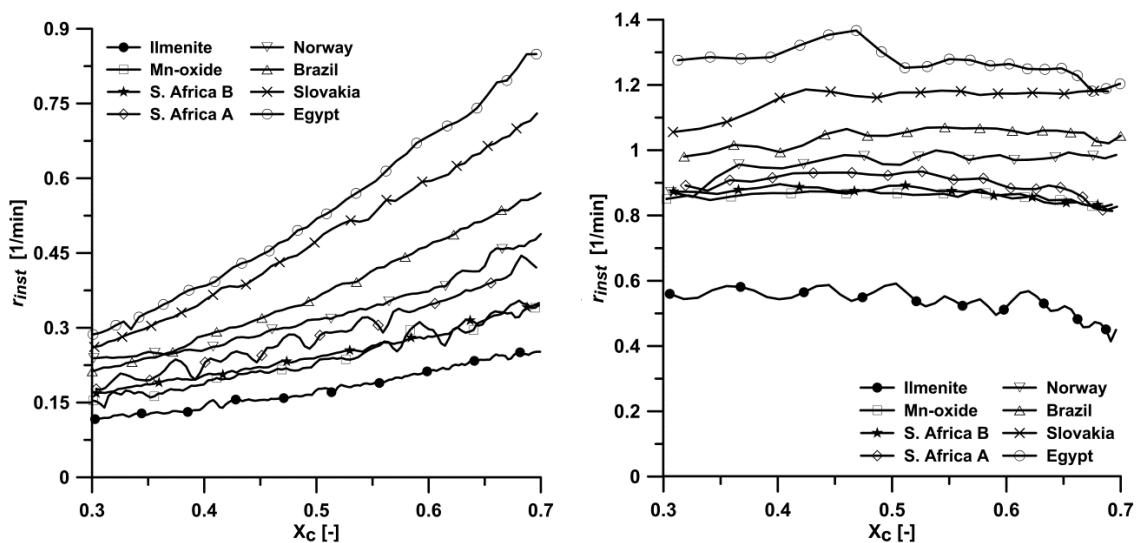


Figure 3.33 Instantaneous rate of char gasification,  $r_{inst}$ , as a function of char conversion,  $X_C$ , for manganese ores, ilmenite and Mn-oxide using 0.1 g of (left) petcoke and (right) wood char as the fuel at 970°C. The inlet gas was 50% H<sub>2</sub>O in N<sub>2</sub>.

### 3. RESULTS AND DISCUSSION

gasification was almost constant and did not change with fuel conversion. However, as gasification progressed through the petcoke particles, the char structure broke up and became more porous, and as a result, the gasification rate increased with fuel conversion. For both fuels, the manganese ores and the Mn-oxide oxygen carrier exhibited a higher rate of char gasification than ilmenite. Thus, the order of the gasification rate for the investigated materials is as follows: Egypt > Slovakia > Brazil > Norway > South Africa A > South Africa B manganese ores > Mn-oxide > Ilmenite.

One explanation for the higher rate of char gasification in the presence of the manganese ores is the contribution by the release of oxygen from the ores, meaning that some of the char was converted through the CLOU effect. As shown in Figure 3.4, only some of the manganese ores, i.e. Slovakian and South African A and B, indicated small concentrations of oxygen during the inert periods. However, manganese ores from Norway, Brazil and Egypt which did not release any oxygen showed similarly high rates of char gasification for both of the solid fuels as illustrated in Figure 3.33. Therefore, the increase in char gasification when using manganese ores may not be solely connected with the small amount of oxygen that is released from some of the ores.

The higher rate of char gasification in the presence of the manganese ores could also be associated with the weakened  $H_2$  inhibition of steam gasification, because  $H_2$  is oxidized by the oxygen carrier. It has been reported that the rate of char gasification can be enhanced in the presence of an oxygen carrier ( $MgAl_2O_4$ -supported  $Fe_2O_3$ ) as compared to sand.<sup>33</sup> An increase by a factor of two in the rate of char gasification in beds of ilmenite and Fe-based oxygen carriers have been reported.<sup>163</sup> This is ascribed to the oxygen carriers effectively removing  $H_2$  which is a known inhibitor for steam gasification of carbon.<sup>164</sup> A decrease in CO inhibition by the oxygen carrier also enhances the rate of char gasification when  $CO_2$  is used as the gasifying agent,<sup>24</sup> but the CO inhibition appeared to be less important than  $H_2$  inhibition when gasification was carried out using steam.<sup>165</sup> It is known that manganese-based oxygen carriers have a higher reactivity towards CO and  $H_2$  gases than iron-based oxygen carriers.<sup>133</sup> Figure 3.34 shows the gas conversion,  $\eta_{gas}$ , as a function of carbon conversion,  $X_C$ , during experiments with gasification of petcoke for all tested materials. It can clearly be seen that the gas conversion was higher for the manganese ores and was close to the gas conversion for the Mn-oxide oxygen carrier. This suggests that the  $H_2$  inhibition for manganese-based oxygen carriers was lower than for ilmenite. Therefore for manganese-based oxygen carriers, a decrease in the average  $H_2$  concentration in

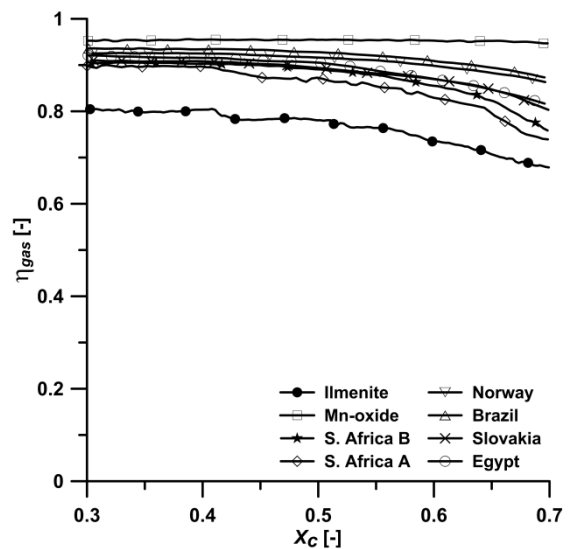


Figure 3.34 Gas conversion,  $\eta_{gas}$ , as a function of char conversion,  $X_C$ , using 0.1 g of petcoke for manganese ores, ilmenite and Mn-oxide.

the bed would be expected for a higher rate of char gasification, in accordance with  $H_2$  inhibition models.<sup>163</sup>

Figure 3.35 shows the arithmetic average of the instantaneous rate of char conversion,  $\bar{r}_{inst}$ , as a function of the arithmetic average of  $H_2$  concentration in the bed using petcoke, and for the char conversion degree,  $X_C$ , between 0.3 and 0.7, for all of the investigated materials. In comparison to ilmenite, the Mn-oxide oxygen carrier and manganese ores from Norway and Brazil show a combination of a higher rate of char gasification and a lower average  $H_2$  concentration in the bed. However, in the presence of South African A and B, Slovakian and Egyptian manganese ores, the arithmetic average of  $H_2$  concentration in the bed is equal to or higher than ilmenite. Interestingly, the Slovakian and the Egyptian manganese ores had a higher rate of gasification for petcoke than the Norwegian and the Brazilian ores, although the former materials actually have higher average  $H_2$  concentrations in the bed, as can be seen in Figure 3.35. These

results indicate that the decrease in  $H_2$  inhibition was not the only and determining mechanism by which the manganese ores obtained a higher rate of char gasification compared to ilmenite.

The final possibility considered is that the manganese ores have a catalytic effect on char gasification. It is well known that alkali metal salts may catalyse the char gasification reaction.<sup>166-173</sup> Among these, potassium salts are well-known gasification catalysing agents.<sup>166-169</sup> The use of  $K_2CO_3$ -impregnated iron ore as oxygen carrier in CLC has also shown to increase the rate of steam gasification of anthracite coal.<sup>174</sup> Sodium salts are another known catalysing agents for the char gasification reaction.<sup>166-173</sup> Some investigations have also reported  $Na_2CO_3$  as a more potent catalysing agent than  $K_2CO_3$ ,<sup>168, 169</sup> although the order of the catalytic activity of these salts seems

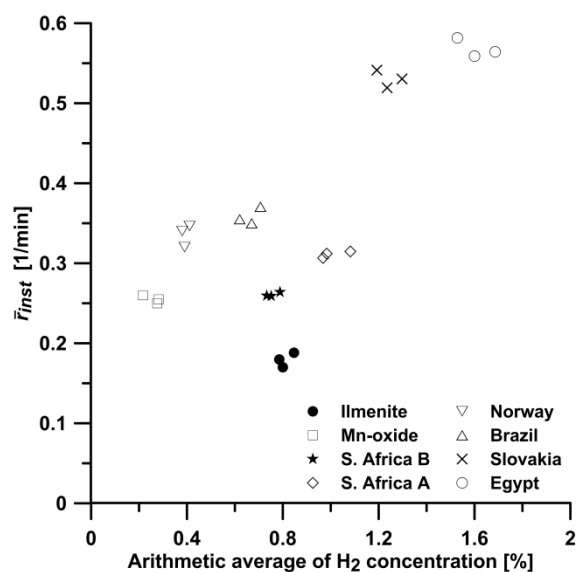


Figure 3.35 Arithmetic average of instantaneous rate of carbon conversion,  $\bar{r}_{inst}$ , as a function of arithmetic average of dry gas  $H_2$  concentration using 0.1 g of petcoke for manganese ores, ilmenite and Mn-oxide.

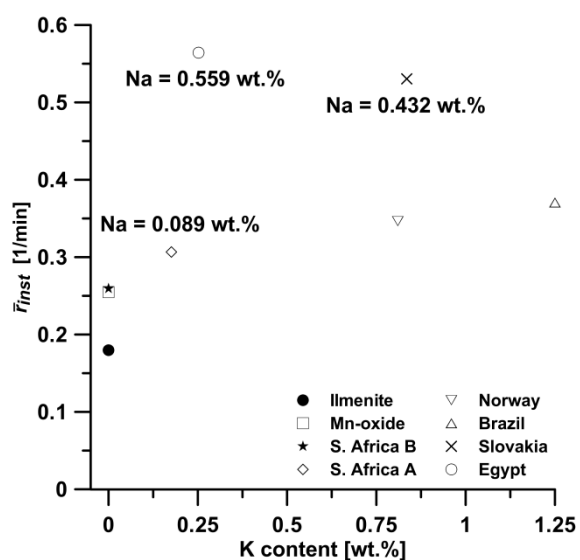
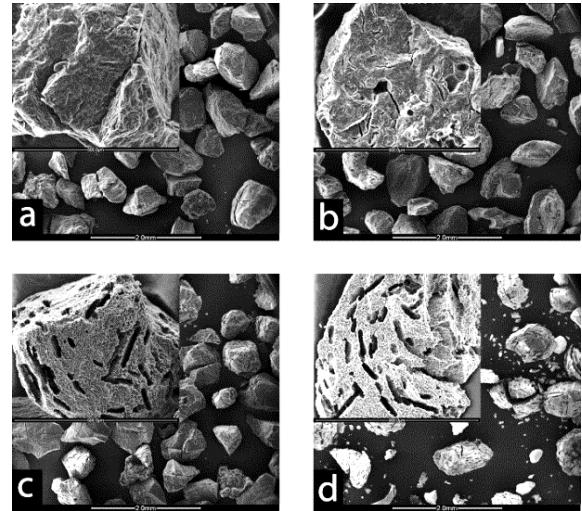


Figure 3.36 Arithmetic average of instantaneous rate of carbon conversion,  $\bar{r}_{inst}$ , using 0.1 g of petcoke as a function of potassium and sodium content in the investigated manganese ores. The concentration of potassium in South African B manganese ore, ilmenite and Mn-oxide oxygen carrier was assumed to be zero (Table 2.5).

### 3. RESULTS AND DISCUSSION

to be affected by pre-treatment conditions.<sup>175</sup> It can be inferred from Figure 3.36 that the arithmetic average of the instantaneous rate of char conversion,  $\bar{r}_{inst}$ , for petcoke increased with the content of potassium in the manganese ores. Moreover, the Slovakian and the Egyptian manganese ores, which showed the highest rate of char gasification, also have the highest content of sodium (Table 2.5).

Figure 3.37 shows the ESEM images of partially gasified petcoke particles (sized 500–750  $\mu\text{m}$ ) in different bed materials. It can be seen in Figure 3.37 (a–b) that the surface of the fuel particles in the bed of Mn-oxide oxygen carrier and South African B manganese ore underwent edge recession and erosion; a common behaviour in the gasification of solid fuels.<sup>176</sup> However, when the Slovakian and



**Figure 3.37** ESEM images of partially gasified petcoke particle in the bed of (a) Mn-oxide oxygen carrier (b) South African B, (c) Slovakian and (d) Egyptian manganese ores. The micrometer bars in the inset and outset ESEM images are 500  $\mu\text{m}$  and 2 mm, respectively.

Egyptian manganese ores were used as the bed material, cavities and channels appear on the surface of the fuel particles, Figure 3.37 (c–d); a common phenomenon in catalytic gasification.<sup>176,</sup>

177

Figure 3.38 shows the corresponding EDX spectrums from surface elemental mapping of the partially gasified petcoke particles in different beds. The only elements found on the surface of the partially gasified fuel particles in the bed of the Mn-oxide oxygen carrier and South African B manganese ore were carbon, oxygen, vanadium and sulphur elements, which are inherent to the petcoke particles. However, with the Slovakian and Egyptian manganese ores as the bed material, potassium and sodium elements were additionally found on the surface of the fuel particles.

Figure 3.39 shows the surface EDX mapping of a partially gasified petcoke particle in a bed of Egyptian manganese ore. A small manganese ore particle can be seen on the surface of the petcoke particle, which was rich in the occurring elements of the ore, i.e. calcium, magnesium, silicon, manganese and aluminium. However, the potassium and sodium elements were well distributed throughout the

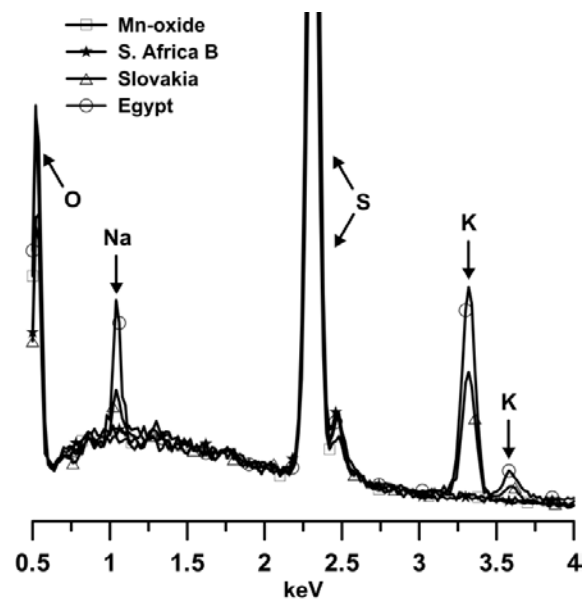


**Figure 3.38** EDX spectrums of partially gasified petcoke particles in different bed materials.

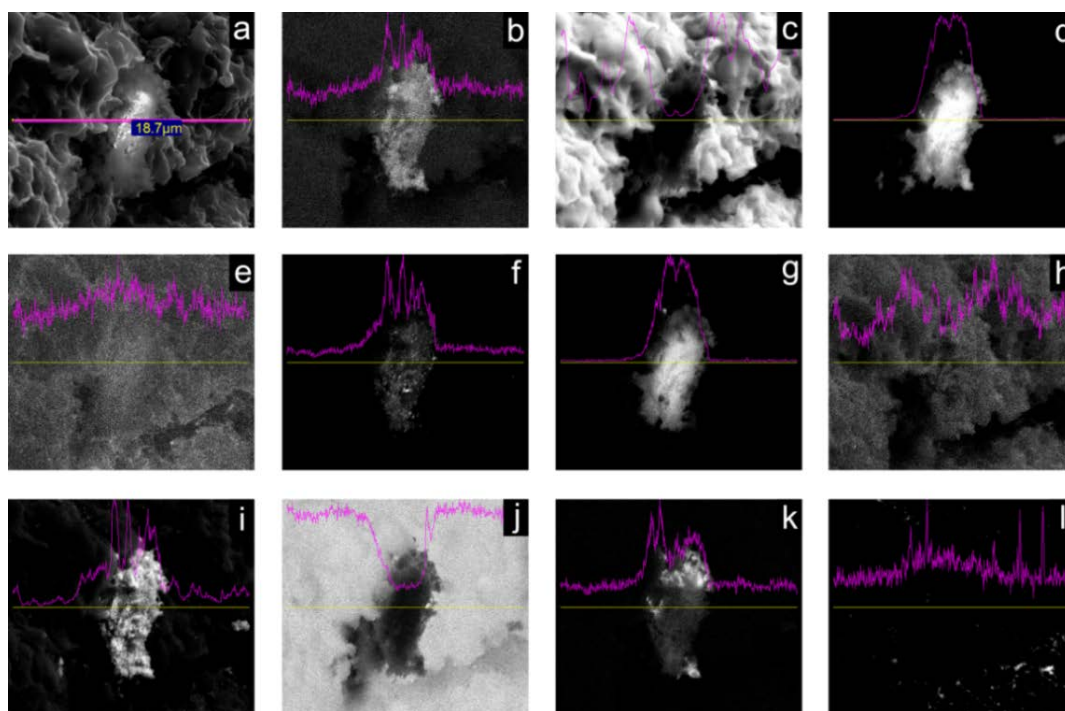


Figure 3.39 EDX mapping of a partially gasified petcoke particle in a bed of Egyptian manganese ore. (a) electron image, (b) aluminium, (c) carbon, (d) calcium, (e) potassium, (f) magnesium, (g) manganese, (h) sodium, (i) oxygen, (j) sulphur, (k) silicon, (l) vanadium. The width of the electron image map is  $18.7 \mu\text{m}$ .

surface of the fuel particle along with the inherent elements of petcoke, i.e. carbon, oxygen, vanadium and sulphur. The catalytic effect of either potassium or sodium compounds on the char gasification has been thoroughly studied in the literature. A review of the possible mechanisms for catalytic gasification can be found in the work by Moulijn et al.<sup>178</sup> It should be noted however, that the experimental conditions in this work are rather different from those in catalytic gasification in which the char is directly loaded or impregnated with the catalysing agent. Yet, carbonates, oxides and hydroxides of potassium and sodium have melting and boiling temperatures close to the operating temperature used in this work ( $970^\circ\text{C}$ ).<sup>167</sup> Therefore, one possible mechanism may be that the catalysing agents were released in the gas phase, after which they were bound to the surface of the char and induced catalytic activity. This may be inferred from the uniform distribution of sodium and potassium elements on the surface of the partially gasified petcoke particles, as shown in Figure 3.39. These findings are also in conformity with a recent study of the effect of potassium on fuel particles using the Brazilian manganese ore as bed material.<sup>179</sup>

### 3.10 Characteristics of Oxygen Carriers Before and After Redox Cycle (Papers I, II, IV, V and VIII)

Recent studies have highlighted the significance of using different characterization techniques in CLC.<sup>180, 181</sup> It is important to examine the changes in physical and chemical properties as well as integrity of the oxygen carrier particles for any possible occurrence of fragmentation and/or agglomeration as well as deactivation or formation of ternary phases after reactivity testing. For

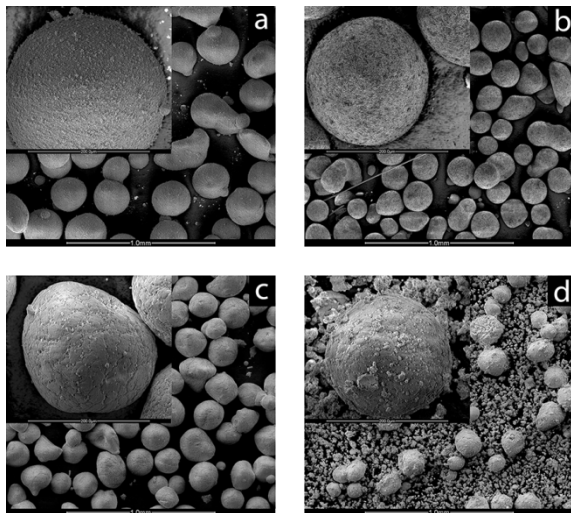


Figure 3.40 ESEM images of (a) C4A-950, (b) C4A-1050, (c) C4MA-950 and (d) C4MA-1050 after reactivity test. The micron bars in the inset and outset images are 200  $\mu\text{m}$  and 1 mm, respectively.

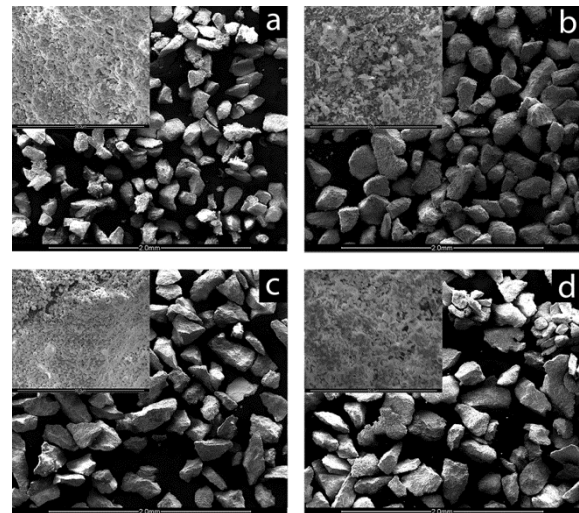


Figure 3.41 ESEM images of fresh and used (a-b) Slovakian and (c-d) South African A manganese ores. The micron bars in the inset and outset figures are 50  $\mu\text{m}$  and 2 mm, respectively.

detailed results on changes in morphology, apparent density, BET specific surface area, particle size distribution (PSD), and crystalline structure of the oxygen carriers, see Papers I, II, IV, V and VIII. Below, some examples of the characterization and material analysis of some of the oxygen carriers are presented.

The ESEM images of the copper-based oxygen carriers after the reactivity test and fresh and used manganese ores are shown, respectively in Figure 3.40 (a–d) and Figure 3.41 (a–d). Compared to the fresh sample, the surface morphology of the C4A-1050 and C4MA-950 particles did not change appreciably. For the C4MA-1050 sample, most of the particles disintegrated forming a considerable amount of fines. The used C4A-950 particles also exhibited slight fragmentation. The surface morphology of the manganese ore particles did not appear to have changed noticeably when examined with ESEM. For all tested manganese ores after either gaseous or solid fuel experiments, small agglomerates of a few particles were observed when the particles were extracted from the reactor. However, this had not affected the fluidization of the particles as indicated by the pressure fluctuations over the bed.

The changes in BET specific surface area or density were in general unique to every oxygen carrier. For example, for the  $\text{CuAl}_2\text{O}_4$  (C4A-1050) sample, a decrease in the apparent density and a slight increase in the BET specific surface area for the used particles were observed after every set of 15 cycles, suggesting that the particles had slightly swelled. This decreasing trend in the apparent density is adverse to the general consensus that materials become densified upon heat treatment. However, it is worth noting that the conditions in a redox operation are different from those during calcination. For the manganese ores investigated, a decrease in the density of the particles was also found. The BET specific surface area also decreased considerably which could suggest a change in

pore size distribution towards larger pores. For the spray-dried perovskite-type materials, there was no or little change in either density or BET specific surface area of the materials. The BET specific surface area did not change for the extruded perovskite-structured materials, however, the bulk density decreased substantially.

The particle size distributions (PSD) of the extruded perovskite-type oxygen carriers before and after reactivity tests are shown in Figure 3.42, as an example. In the case of CLMT, the presence of fine particles in the fresh samples is noticeable. These fine particles were most likely entrained from the reactor during the reactivity test. The PSDs for the rest of the oxygen carriers are quite similar, before and after the reactivity tests.

Only a few of the studied materials showed reasonable mechanical stability, as indicated by the crushing strength measured prior to the reactivity tests shown in Tables 2.1–2.5. It should be noted that the crushing strength might not correlate linearly with attrition and fragmentation behaviour in a real CLC system. Dust formation or particle fragmentation was generally not observed during batch fluidized-bed experiments. However, given that the total number of cycles and the gas velocities employed in this setup were rather low, further long-term tests in continuous operation will be needed in order to confirm the mechanical stability of the materials. Figure 3.43 shows the rate of attrition of the used extruded perovskite-type oxygen carriers during testing in a jet-cup attrition rig for 1 h. It can be noted that up to approximately 30 min, the rate of attrition was quite high. This is likely due to the erosion of sharp edges, which were then entrained in the early stages of the test. Here, the attrition index,  $A_i$ , is defined as the slope of the attrition in the last 30 min of the test period, where more stable values of attrition rates were achieved. Although the rates presented are still not sufficiently low for a realistic CLC unit, they are within the range of other oxygen carriers tested in the same rig with satisfactory operation during hot experiments.<sup>142</sup>

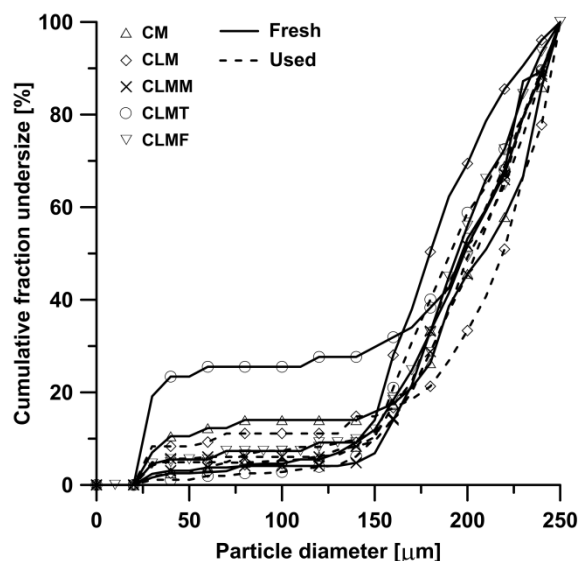


Figure 3.42 Particle size distributions (PSD) of the fresh and used extruded perovskite-structured oxygen carriers.

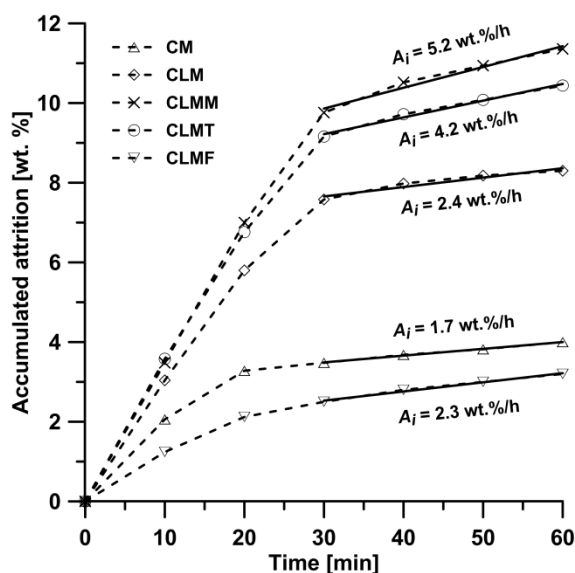
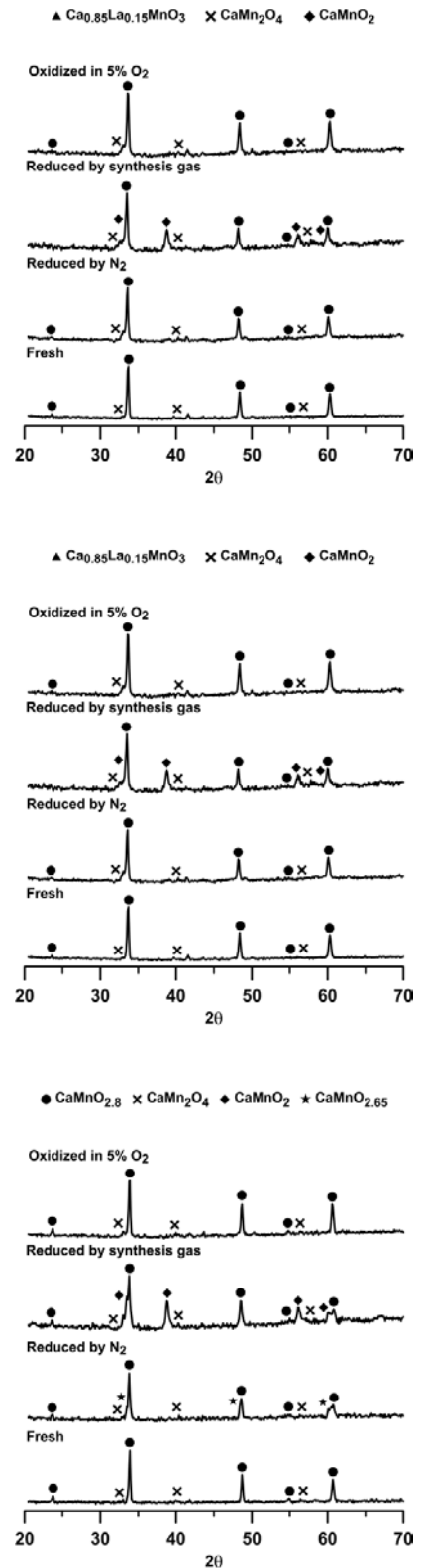


Figure 3.43 Attrition rates of the extruded perovskite-type oxygen carriers following the reactivity test.

### 3. RESULTS AND DISCUSSION

However, it is clear that for use in a full scale plant, the mechanical resistance of these particles would need to be increased, e.g. by changing or optimizing the manufacturing technique. The spray-dried perovskite-type oxygen carriers also had rates of attrition similar to those for  $\text{CaMn}_{0.9}\text{Mg}_{0.1}\text{O}_{3-\delta}$  (C50MMg), that has shown excellent functionality in continuous operation in a 10 kW unit.<sup>112</sup> Consequently, equally good results could be expected for these materials.

The XRD analysis of fresh as well as used samples for some of the extruded perovskite-type oxygen carriers are shown in Figure 3.44 as an example. It has been reported in the literature<sup>109, 110</sup> that undoped  $\text{CaMnO}_{3-\delta}$  undergoes decomposition to  $\text{CaMn}_2\text{O}_4$  and  $\text{Ca}_2\text{MnO}_{4-\delta}$  when subject to low oxygen partial pressure at sufficiently high temperatures. Although this decomposition is reported as reversible with respect to other applications, it had not been investigated in CLC. In the case of the used samples, the reactivity cycles ended in  $\text{N}_2$ , synthesis gas and oxidation (5%  $\text{O}_2$ ) streams at 950°C. A thorough analysis of the XRD patterns was made difficult due to the superimposition of several diffraction peaks. Also, in the case of B-site doped materials,  $\text{Ca}_{0.85}\text{La}_{0.15}\text{MnO}_3$  or  $\text{Ca}_{0.9}\text{La}_{0.1}\text{Mn}_{0.8}\text{Ti}_{0.2}\text{O}_3$  compounds are suggested by the XRD database, even though the doping in either case was only 10 mol.%. Other oxygen-deficient perovskite structures, however, could be identified in terms of their distinct peaks. In all cases, oxidation of the reduced samples restored a composition similar to that of the fresh oxygen carrier. A minor amount of the  $\text{CaMn}_2\text{O}_4$  spinel in the oxidized and reduced samples was also detected. In light of the XRD patterns, the phase evolution could be classified into two categories, corresponding to two different behaviours predominantly in the synthesis gas environment: (1) The  $\text{CaMnO}_{3-\delta}$  (CM) and A-site doped  $\text{Ca}_{0.9}\text{La}_{0.1}\text{MnO}_{3-\delta}$  (CLM) samples were reduced with synthesis gas, forming a  $\text{CaMnO}_2$  phase (characterized by peak splitting at  $2\theta = 34.5^\circ$  and  $60.5^\circ$ ). The regeneration of the parent perovskite-type CM upon oxidation (Figure 3.44; bottom) was in accordance with several studies.<sup>109, 110, 182, 183</sup> The formation of  $\text{CaMnO}_2$  was visually verified by the characteristic olive-green colour<sup>182, 184</sup> of the particles after the



**Figure 3.44** XRD patterns of fresh, reduced in  $\text{N}_2$ , reduced by syngas and oxidized samples of extruded perovskite-structured materials: (bottom) CM (middle) CLM and (top) CLMT.

reduction of CM with synthesis gas. Thus, in the case of  $\text{CaMnO}_{3-\delta}$  (CM) and  $\text{Ca}_{0.9}\text{La}_{0.1}\text{MnO}_{3-\delta}$  (CLM), Mn changed from  $\text{Mn}^{4+}$  to  $\text{Mn}^{2+}$  as they transformed into  $\text{CaMnO}_2$  upon reduction at high temperatures. (2) In the case of A- and B-site doped particles (CLMT, CLMF, CLMM), the XRD patterns looked very similar to each other in all cases without any evidence of  $\text{CaMnO}_2$  formation after reduction with synthesis gas. This suggests that the doubly-doped compounds are less prone to phase separation as opposed to their undoped and the singly-doped analogues.

For the spray-dried perovskite-type oxygen carriers, the intensity of characteristic peaks for marokite ( $\text{CaMn}_2\text{O}_4$ ) increased with a concomitant decrease in the intensity for peaks associated with the active perovskite-based material, e.g.  $\text{CaMnO}_{3-\delta}$ , following reactivity testing both in the presence and absence of  $\text{SO}_2$ . This was the case for all samples except for the Mg and Ti-doped materials. In all Mg-containing samples, MgO was also found as a separate phase, and was not incorporated into the perovskite structure, likely due to a mismatch in the ionic radii of Mg and Mn,<sup>185</sup> which has also been reported elsewhere<sup>104, 105, 112</sup> for  $\text{CaMn}_{0.9}\text{Mg}_{0.1}\text{O}_{3-\delta}$  (C50MMg).

The XRD analysis of the copper-based materials indicated that, except for C4A-950, it was possible to oxidize the reduced samples to a composition similar to the fresh oxygen carrier. For the manganese ores,  $\text{Mn}_2\text{O}_3$ ,  $\text{Mn}_3\text{O}_4$ ,  $\text{MnO}_2$  and  $\text{Fe}_2\text{O}_3$  were identified as active oxides in most of the fresh ores using XRD. However, after the reactivity test using gaseous fuels, only  $\text{Mn}_3\text{O}_4$  and  $\text{Fe}_2\text{O}_3$  were seen. This would be expected since, in the range of the temperatures investigated here,  $\text{Mn}_3\text{O}_4$  is the stable oxidized phase of Mn after oxidation at 5%  $\text{O}_2$ , see Figure 1.4.

Figure 3.45 shows the oxygen-carrying capacity of the extruded perovskite-based materials for CLOU after the reactivity tests using a thermogravimetric analyser, when cycled between synthetic air (20.8%  $\text{O}_2$ ) and high purity  $\text{N}_2$ . The slightly higher capacities

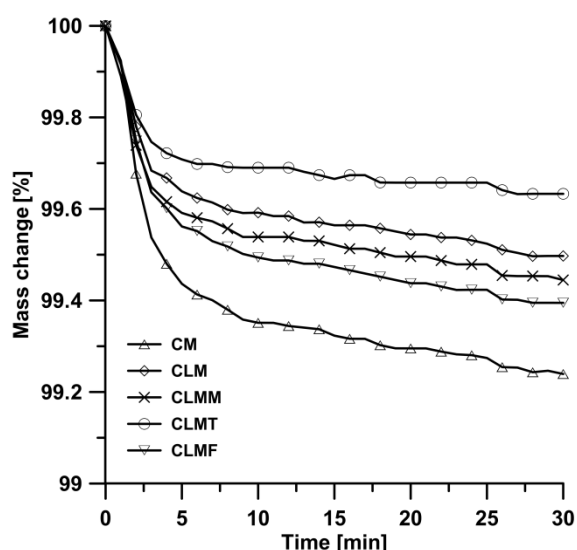


Figure 3.45 Oxygen capacity ( $R_O$ ) of the extruded perovskite-type oxygen carriers during cycling between synthetic air (20.8%  $\text{O}_2$ ) and high purity inert gas ( $\text{N}_2$ ) at 950°C in a thermogravimetric analyser.

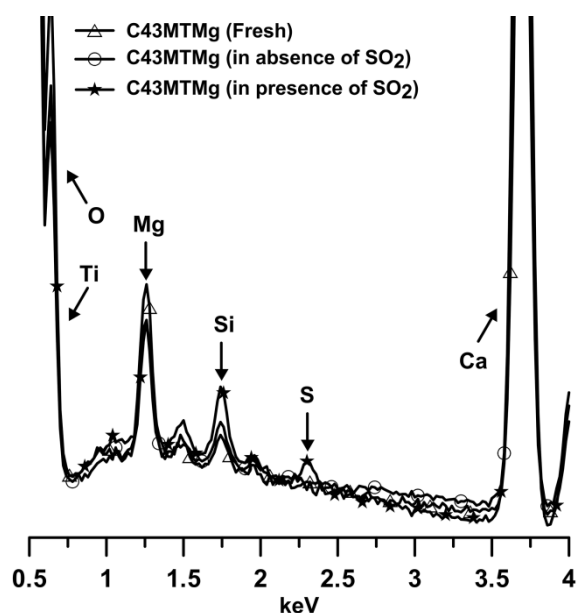


Figure 3.46 Partial EDX spectrums of fresh  $\text{Ca}_{0.75}\text{Mn}_{0.775}\text{Mg}_{0.10}\text{Ti}_{0.125}\text{O}_{3-\delta}$  (C43MTMg), and particles subjected to reactivity tests in the absence and presence of  $\text{SO}_2$ .

### 3. RESULTS AND DISCUSSION

---

than those in Figures 3.21 and 3.22 were expected due to the higher oxygen partial pressure (20.8% vs. 5%) used here. As can be seen,  $R_o$  varied from 0.37% (for CLMT) to 0.76% (for CM). The  $R_o$  for CM corresponds well with the expected change in  $3-\delta$  reported by Bakken et al.<sup>109</sup> and Leonidova et al.<sup>108</sup> Doping at the A- and the B-sites both resulted in a decrease in oxygen-carrying capacity. Rørmark et al.<sup>110</sup> have also reported a lower oxygen transfer capacity for  $\text{Ca}_{0.9}\text{La}_{0.1}\text{MnO}_{3-\delta}$  than for  $\text{CaMnO}_{3-\delta}$ .

Partial EDX analysis of the surface of the fresh and used spray-dried perovskite-based samples after reactivity testing in the presence and absence of  $\text{SO}_2$  is shown in Figure 3.46. Following the reactivity experiments in the presence of  $\text{SO}_2$ , a uniform distribution of sulphur could be found on the surface of the materials in addition to the inherent elements of the oxygen carrier, i.e. calcium, titanium, magnesium, manganese and oxygen. However, analysis of the bulk cross sections did not show the presence of sulphur, despite reports of the complete destruction of the perovskite-based bulk catalysts when deactivated with  $\text{SO}_2$ .<sup>118-120</sup> This could again be attributed to the limited number of reactivity cycles in the presence of  $\text{SO}_2$  carried out in this work.

## 4. CONCLUSIONS

---

Copper- and manganese-based oxygen carriers were investigated for the CLC and the CLOU processes. Their chemical-looping performance was examined in a laboratory-scale fluidized-bed reactor at different temperatures under alternating reducing and oxidizing conditions. The materials were generally evaluated with respect to oxygen release, reactivity and performance. Detailed material analysis and characterization of various oxygen carriers were carried out. Different gaseous fuels such as methane and syngas (50% CO in H<sub>2</sub>) as well as solid fuels such as petroleum coke and wood char were used.

Investigation of four copper-based oxygen carriers showed that:

- Freeze-granulated oxygen carriers consisting of CuO supported on Al<sub>2</sub>O<sub>3</sub> and MgAl<sub>2</sub>O<sub>4</sub> yielded complete conversion of methane during short reduction cycles in the temperature range of 900–925°C. Three of these materials also featured the rapid release of oxygen in an inert environment (CLOU).
- Using Al<sub>2</sub>O<sub>3</sub> as support material, the CuO reacted with Al<sub>2</sub>O<sub>3</sub>, thus forming CuAl<sub>2</sub>O<sub>4</sub>, which is also a viable oxygen carrier, although only for CLC and not CLOU. Furthermore, part of the CuO and CuAl<sub>2</sub>O<sub>4</sub> active phases were not restored upon oxidation due to the formation of CuAlO<sub>2</sub>.
- During longer reduction cycles of the MgAl<sub>2</sub>O<sub>4</sub>-supported oxygen carriers, it was found that the active CuO phase was retained by avoiding interaction between CuO and the support material, thus offering stable oxygen release and stability in reactivity and performance.

The CuAl<sub>2</sub>O<sub>4</sub> oxygen carrier was further investigated in a larger number of cycles and in the temperature range of 900–950°C for CLC. Systematic phase analysis of the Cu–Al–O system during the redox cycle was carried out as a function of duration of reduction and oxygen concentration during the re-oxidation period. The phase relationships in the Cu–Al–O system for CLC was established by reassessing the standard enthalpy of formation,  $\Delta H_f^0$ , of CuAl<sub>2</sub>O<sub>4</sub> using TGA/DSC. The reassessment was motivated by a discrepancy between thermodynamic databases. It was concluded that:

- Agglomeration or defluidization was not encountered during experiments at 900 and 925°C. However, after reactivity testing at 950°C, soft agglomeration and particle fragmentation were observed.
- The reduction of the spinel (CuAl<sub>2</sub>O<sub>4</sub>) involves the formation of CuAlO<sub>2</sub>, Cu<sub>2</sub>O and elemental Cu. The CuAlO<sub>2</sub> has slow kinetics for re-oxidation which results in partial loss of the active

#### 4. CONCLUSIONS

---

phase after several redox cycles. Thus, a decrease in the oxygen-carrying capacity of the material could be expected; although, this may be compensated by a larger solids inventory.

The effect of doping at the A- and/or B-site on the oxygen-carrying capacity, performance, reactivity and stability of perovskite-type oxygen carriers synthesized by extrusion was investigated. The following observations were made:

- It was found that doping can significantly affect the aforementioned properties.
- With the exception of Cu-doped material which defluidized, nearly complete gas yield was obtained for methane at 950°C. With synthesis gas, complete gas yield was obtained for all materials at the same temperature.
- All particles exhibited CLOU behaviour and the reactivity tests showed that this class of oxygen carriers reacted both via CLC and CLOU in the fuel reactor.

The effect of calcium content and dopant in spray-dried perovskite-type oxygen carriers was evaluated with respect to reactivity and performance as well as tolerance towards deactivation with sulphur. The following conclusions could be drawn:

- The reactivity of the materials with methane was high and increased with temperature and calcium content, approaching complete gas yield at 1000°C. However, the reactivity decreased in the presence of SO<sub>2</sub> for all of the oxygen carriers investigated. All materials also exhibited CLOU behaviour.
- Decreasing the calcium content in the materials generally resulted in a lower decrease in reactivity in the presence of SO<sub>2</sub>, with the exception of materials doped with both Mg and Ti, where a higher resistance to sulphur deactivation could be maintained even at higher calcium contents. The drop in reactivity in the presence of SO<sub>2</sub> also decreased at higher temperatures, and at 1050°C the decrease in the reactivity of the Mg and Ti-doped material was minimal.
- Sulphur balance over the reactor system indicated that the fraction of the SO<sub>2</sub> introduced which passed through the reactor increased with temperature. It was shown that it is possible to regenerate the oxygen carriers during reduction in the absence of SO<sub>2</sub>. Most of the materials developed also showed relatively low attrition rates. Nevertheless, any safe assessment of the sulphur tolerance of perovskite-type oxygen carriers would require further investigation in continuous operation.

A method for obtaining the rate of oxygen release for CLOU was developed and was applied to the MgAl<sub>2</sub>O<sub>4</sub>-supported CuO oxygen carrier as well as the extruded perovskite-type materials. In this method, devolatilized wood char was added to facilitate oxygen release from the oxygen carrier in N<sub>2</sub>-fluidization by maintaining a low oxygen concentration around the particles. The oxidation rate

---

of the  $\text{MgAl}_2\text{O}_4$ -supported CuO oxygen carrier for CLOU was also studied. The main conclusions were:

- The Avrami-Erofeev mechanism was found to best describe the rates of oxygen release for the  $\text{CuO}/\text{MgAl}_2\text{O}_4$  oxygen carrier. However, during oxidation it was observed that the rate was limited by oxygen supply, indicating rapid conversion of the oxygen carrier. Based on the rates obtained, the minimum solids inventory was determined for a CLOU unit operating at a temperature of  $900^\circ\text{C}$  in the fuel reactor and at  $850^\circ\text{C}$  in the air reactor. The total inventory of solids required in the fuel and the air reactor was estimated to be between 73–147  $\text{kg}/\text{MW}_{\text{th}}$ .
- Compared to the  $\text{CuO}/\text{MgAl}_2\text{O}_4$  oxygen carrier, the rate of oxygen release in the CLOU regime was approximately 20 times lower at  $950^\circ\text{C}$  for the extruded perovskite-type oxygen carrier materials. The required solids inventory in the fuel reactor using these materials was estimated to be 325  $\text{kg}/\text{MW}_{\text{th}}$ .

Six different manganese ores were investigated for application with CLC for solid fuels and the results were compared to ilmenite and a Mn-oxide oxygen carrier. It was found out that:

- Three of the manganese ores showed a small oxygen release in the inert environment.
- Using methane as the fuel, it was observed that the gas yield increased with temperature for all of the manganese ores. In the case of 50% CO in  $\text{H}_2$ , all of the manganese ores yielded complete conversion of the fuel.
- The manganese ore and the Mn-oxide oxygen carrier exhibited a higher rate of char gasification than ilmenite. The gas conversion during the gasification of petcoke was also higher with these materials than with ilmenite. This suggests that manganese-based oxygen carriers have higher reactivity towards the gasification products, i.e. CO and  $\text{H}_2$ , compared to ilmenite.
- Surface comparison of partially gasified petcoke particles in different beds suggested that when alkali-containing manganese ores are used as bed material, cavities and channels are formed on the surface of the fuel particles, which is a common behaviour in catalytic gasification. Surface elemental analysis of the partially gasified petcoke particles in the bed of Slovakian and Egyptian manganese ores indicated the presence of potassium and sodium. These elements were also thoroughly distributed throughout the surface of the fuel particles.
- The rates of char gasification could be correlated to the concentration of potassium and sodium in the manganese ores, i.e. the rate of char gasification increased with the content of potassium and sodium impurities in the ores, which are well-known catalysing agents for the char gasification reaction.



## NOMENCLATURE

---

$R_O$	Oxygen-carrying capacity [%]
$\gamma_{CH_4}$	Gas yield or conversion efficiency for methane [-]
$\gamma_{CO}$	Gas yield or conversion efficiency for 50% CO in H <sub>2</sub> [-]
$\gamma_{CH_4,tot}$	Total gas yield or conversion efficiency for methane during entire reduction [-]
$\gamma_{CH_4,ave}$	Average gas yield or conversion efficiency for methane during $\omega = 1 - 0.99$ [-]
$y_i$	Gas concentration of the $i$ species as measured by the analyser [vol.%]
$y_{i,act}$	Deconvoluted gas concentration of the $i$ species [vol.%]
$\frac{dy_i}{dt}$	Change in gas concentration of the $i$ species over a time interval [vol.%/s]
$\omega$	Mass-based conversion of the oxygen carrier [%]
$\Delta\omega$	Change in mass-based conversion of the oxygen carrier [-]
$m_{ox}$	Mass of the oxygen carrier in oxidized state [g]
$m$	Actual mass of the oxygen carrier during the experiments [g]
$n_o$	Number of moles of molecular oxygen in the oxygen carrier [-]
$X_{red}$	Conversion of the oxygen carrier during reduction [-]
$X_{red,norm}$	Normalized conversion of the oxygen carrier during reduction [-]
$X_{ox}$	Conversion of the oxygen carrier during oxidation [-]
$\tau$	Time constant [s]
$\frac{dX_{red}}{dt}$	Conversion rate of the oxygen carrier during reduction [1/s]
$\dot{n}_{out}$	Molar flow rate of dry gas at the outlet of the reactor [mol/s]
$\frac{dX_{ox}}{dt}$	Conversion rate of the oxygen carrier during oxidation [1/s]
$\dot{n}_{in}$	Molar flow rate of dry gas at the inlet of the reactor [mol/s]
$\dot{n}_{out,corr}$	Corrected molar flow rate at the outlet of the reactor [mol/s]
$t$	Time [s]
$\frac{d\omega}{dt}$	Derivate of change in mass-based conversion of the oxygen carrier [1/s]
$M_O$	Molar mass of oxygen [g/mol]

## NOMENCLATURE

---

$\Delta H_f^0$	Standard enthalpy of formation (at 25°C) [kJ/mol]
$\Delta H^0$	Standard enthalpy of reaction (at 25°C) [kJ/mol]
$\Delta H$	Enthalpy of reaction [kJ/mol]
$\Delta G^0$	Standard Gibbs free energy [kJ/mol]
$k_r$	Rate constant during oxygen release (reduction) of CuO [1/s]
$\frac{dX_{red,norm}}{dt}$	Normalized conversion derivative of the oxygen carrier during reduction [1/s]
$k_{-r}$	Rate constant during oxidation of Cu <sub>2</sub> O [1/s.atm]
$P_{O_2,ave}$	Logarithmic average of partial pressure of oxygen [atm]
$P_{O_2,eq}$	Equilibrium partial pressure of oxygen [atm]
$P_{O_2,in}$	Partial pressure of oxygen at the inlet of the reactor [atm]
$P_{O_2,out}$	Partial pressure of oxygen at the outlet of the reactor [atm]
$\dot{m}_{OC}$	Rate of solid flow between the two reactors [kg/s.MW <sub>th</sub> ]
$X_C$	Fraction of char conversion [-]
$m_C(t)$	Mass of carbon converted at time $t$ [g]
$m_{tot}$	Cumulative mass of carbon converted during one cycle [g]
$M_C$	Molar mass of carbon [g/mol]
$r_{inst}$	Instantaneous rate of char conversion (gasification) [1/min]
$\frac{dX_C}{dt}$	Derivative of fraction of char conversion (gasification) [1/min]
$\bar{r}_{inst}$	Arithmetic average of rate of char conversion (gasification) [1/min]
$\eta_{gas}$	Gas conversion during experiments with steam gasification of petcoke [-]
$A_i$	Attrition index [wt.%/h]
$\eta_{SO_2}$	SO <sub>2</sub> yield [-]
$n_{SO_2,in}$	Moles of SO <sub>2</sub> introduced to the reactor
$n_{SO_2,out}$	Moles of SO <sub>2</sub> in the effluent

## BIBLIOGRAPHY

---

- (1) Hansen, J. Defusing the Global Warming Time Bomb, *Scientific American*, 2004, 290, 68-77.
- (2) Shakun, J. D.; Clark, P. U.; He, F.; Marcott, S. A.; Mix, A. C.; Liu, Z.; Otto-Bliesner, B.; Schmittner, A.; Bard, E. Global warming preceded by increasing carbon dioxide concentrations during the last deglaciation, *Nature*, 2012, 484 (7392), 49-54.
- (3) Basu, P. *Combustion and Gasification in Fluidized Beds*, CRC Press, Taylor & Francis Group: Boca Raton, 2006.
- (4) Friedlingstein, P.; Houghton, R. A.; Marland, G.; Hackler, J.; Boden, T. A.; Conway, T. J.; Canadell, J. G.; Raupach, M. R.; Ciais, P.; Le Quere, C. Update on CO<sub>2</sub> emissions, *Nature Geosci*, 2010, 3 (12), 811-812.
- (5) *Fourth Assessment Report: Climate Change (Synthesis Report)*, Pachauri, R. K.; Reisinger, A. (Ed.), Intergovernmental Panel on Climate Change: Geneva, 2007.
- (6) Herzog, H. J. *CO<sub>2</sub> capture and storage: Costs and market potential*, Greenhouse Gas Control Technologies 7, Rubin, E. S.; Keith, D. W.; Gilboy, C. F.; Wilson, M.; Morris, T.; Gale, J.; Thambimuthu, K.; Thambimuthu, K. (Ed.), Elsevier Science Ltd: Oxford, 2005.
- (7) Toftegaard, M. B.; Brix, J.; Jensen, P. A.; Glarborg, P.; Jensen, A. D. Oxy-fuel combustion of solid fuels, *Progress in Energy and Combustion Science*, 2010, 36 (5), 581-625.
- (8) Li, B.; Duan, Y.; Luebke, D.; Morreale, B. Advances in CO<sub>2</sub> capture technology: A patent review, *Applied Energy*, 2013, 102, 1439-1447.
- (9) *Special Report: Carbon Dioxide Capture and Storage*, Metz, B.; Davidson, O.; de Coninck, H.; Loos, M.; Meyer, L. (Ed.), Intergovernmental Panel on Climate Change: Cambridge, 2005.
- (10) Lyngfelt, A.; Leckner, B.; Mattisson, T. A fluidized-bed combustion process with inherent CO<sub>2</sub> separation; application of chemical-looping combustion, *Chemical Engineering Science*, 2001, 56 (10), 3101-3113.
- (11) Ishida, M.; Jin, H. A Novel Chemical-Looping Combustor without NO<sub>x</sub> Formation, *Industrial & Engineering Chemistry Research*, 1996, 35 (7), 2469-2472.
- (12) Kronberger, B.; Johansson, E.; Löffler, G.; Mattisson, T.; Lyngfelt, A.; Hofbauer, H. A Two-Compartment Fluidized Bed Reactor for CO<sub>2</sub> Capture by Chemical-Looping Combustion, *Chemical Engineering & Technology*, 2004, 27 (12), 1318-1326.
- (13) Jerndal, E.; Mattisson, T.; Lyngfelt, A. Thermal Analysis of Chemical-Looping Combustion, *Chemical Engineering Research and Design*, 2006, 84 (9), 795-806.
- (14) Lewis, K. W.; Gilliland, E. R.; Sweeney, M. P. Gasification of Carbon Metal Oxides in a Fluidized Powder Bed, *Chemical Engineering Progress*, 1951, 47 (5), 251-256.
- (15) Ishida, M.; Jin, H. A new advanced power-generation system using chemical-looping combustion, *Energy*, 1994, 19 (4), 415-422.
- (16) Lyngfelt, A.; Thunman, H. *Construction and 100 h of operational experience of a 10 kW chemical looping combustor*, The CO<sub>2</sub> Capture and Storage Project (CCP) for Carbon Dioxide Storage in Deep Geologic Formations For Climate Change Mitigation, Thomas, D. (Ed.), Elsevier Science: London, 2003, 1-36.
- (17) Lyngfelt, A. Oxygen Carriers for Chemical Looping Combustion – 4000 h of Operational Experience, *Oil & Gas Science and Technology*, 2011, 66 (2), 161-172
- (18) Lyngfelt, A. Chemical-looping combustion of solid fuels – Status of development, *Applied Energy*, 2014, 113, 1869-1873.

- (19) Lyngfelt, A.; Mattisson, T. *Materials for chemical-looping combustion*, Efficient Carbon Capture for Coal Power Plants, Chapter 17, Stolten, D.; Sherer, V. (Ed.), WILEY-VCH Verlag GmbH & Co. KGaA: Weinheim, 2011.
- (20) Lyngfelt, A. *Chemical looping combustion*, Chapter 20 in Fluidized-bed technologies for near-zero emission combustion and gasification, Scala, F. (Ed.), Woodhead Publishing Limited: Cambridge, 2013, 895-930.
- (21) Hossain, M. M.; de Lasa, H. I. Chemical-looping combustion (CLC) for inherent CO<sub>2</sub> separations – a review, *Chemical Engineering Science*, 2008, 63 (18), 4433-4451.
- (22) Adánez, J.; Abad, A.; García-Labiano, F.; Gayán, P.; de Diego, L. F. Progress in Chemical-Looping Combustion and Reforming technologies, *Progress in Energy and Combustion Science*, 2012, 38 (2), 215-282.
- (23) Fan, L.-S.; Zeng, L.; Wang, W.; Luo, S. Chemical looping processes for CO<sub>2</sub> capture and carbonaceous fuel conversion – prospect and opportunity, *Energy & Environmental Science*, 2012, 5 (6), 7254-7280.
- (24) Brown, T. A.; Dennis, J. S.; Scott, S. A.; Davidson, J. F.; Hayhurst, A. N. Gasification and Chemical-Looping Combustion of a Lignite Char in a Fluidized Bed of Iron Oxide, *Energy & Fuels*, 2010, 24 (5), 3034-3048.
- (25) Dennis, J. S.; Scott, S. A.; Hayhurst, A. N. In situ gasification of coal using steam with chemical looping: a technique for isolating CO<sub>2</sub> from burning a solid fuel, *Journal of the Energy Institute*, 2006, 79, 187-190.
- (26) Dennis, J. S.; Müller, C. R.; Scott, S. A. In situ gasification and CO<sub>2</sub> separation using chemical looping with a Cu-based oxygen carrier: Performance with bituminous coals, *Fuel*, 2010, 89 (9), 2353-2364.
- (27) Dennis, J. S.; Scott, S. A. In situ gasification of a lignite coal and CO<sub>2</sub> separation using chemical looping with a Cu-based oxygen carrier, *Fuel*, 2010, 89 (7), 1623-1640.
- (28) Scott, S. A.; Dennis, J. S.; Hayhurst, A. N.; Brown, T. In situ gasification of a solid fuel and CO<sub>2</sub> separation using chemical looping, *AIChE Journal*, 2006, 52 (9), 3325-3328.
- (29) Leion, H.; Jerndal, E.; Steenari, B.-M.; Hermansson, S.; Israelsson, M.; Jansson, E.; Johnsson, M.; Thunberg, R.; Vadenbo, A.; Mattisson, T.; Lyngfelt, A. Solid fuels in chemical-looping combustion using oxide scale and unprocessed iron ore as oxygen carriers, *Fuel*, 2009, 88 (10), 1945-1954.
- (30) Leion, H.; Lyngfelt, A.; Mattisson, T. Solid fuels in chemical-looping combustion using a NiO-based oxygen carrier, *Chemical Engineering Research and Design*, 2009, 87 (11), 1543-1550.
- (31) Leion, H.; Mattisson, M.; Lyngfelt, A. Chemical Looping Combustion of Solid Fuels in a Laboratory Fluidized-bed Reactor, *Oil & Gas Science and Technology – Rev. IFP Energies nouvelles*, 2011, 66 (2), 201-208.
- (32) Leion, H.; Mattisson, T.; Lyngfelt, A. Solid fuels in chemical-looping combustion, *International Journal of Greenhouse Gas Control*, 2008, 2 (2), 180-193.
- (33) Leion, H.; Mattisson, T.; Lyngfelt, A. The use of petroleum coke as fuel in chemical-looping combustion, *Fuel*, 2007, 86 (12–13), 1947-1958.
- (34) Mattisson, T.; Lyngfelt, A.; Leion, H. Chemical-looping with oxygen uncoupling for combustion of solid fuels, *International Journal of Greenhouse Gas Control*, 2009, 3 (1), 11-19.
- (35) Abad, A.; Adánez-Rubio, I.; Gayán, P.; García-Labiano, F.; de Diego, L. F.; Adánez, J. Demonstration of chemical-looping with oxygen uncoupling (CLOU) process in a 1.5 kW<sub>th</sub> continuously operating unit using a Cu-based oxygen-carrier, *International Journal of Greenhouse Gas Control*, 2012, 6, 189-200.

- (36) Adánez, J.; Gayán, P.; Adánez-Rubio, I.; Cuadrat, A.; Mendiara, T.; Abad, A.; García-Labiano, F.; De Diego, L. Use of Chemical-Looping processes for coal combustion with CO<sub>2</sub> capture, *Energy Procedia*, 2013, 37, 540-549.
- (37) Adánez-Rubio, I.; Abad, A.; Gayán, P.; de Diego, L. F.; García-Labiano, F.; Adánez, J. Identification of operational regions in the Chemical-Looping with Oxygen Uncoupling (CLOU) process with a Cu-based oxygen carrier, *Fuel*, 2012, 102, 635-645.
- (38) Adánez-Rubio, I.; Abad, A.; Gayán, P.; de Diego, L. F.; García-Labiano, F.; Adánez, J. Performance of CLOU process in the combustion of different types of coal with CO<sub>2</sub> capture, *International Journal of Greenhouse Gas Control*, 2013, 12, 430-440.
- (39) Jacob, K. T.; Alcock, C. B. Thermodynamics of CuAlO<sub>2</sub> and CuAl<sub>2</sub>O<sub>4</sub> and Phase Equilibria in the System Cu<sub>2</sub>O–CuO–Al<sub>2</sub>O<sub>3</sub>, *Journal of the American Ceramic Society*, 1975, 58 (5–6), 192-195.
- (40) Chen, M.; Hallstedt, B.; Gauckler, L. Thermodynamic assessment of the Co–O system, *Journal of Phase Equilibria*, 2003, 24 (3), 212-227.
- (41) Jacob, K. T.; Kumar, A.; Rajitha, G.; Waseda, Y. Thermodynamic Data for Mn<sub>3</sub>O<sub>4</sub>, Mn<sub>2</sub>O<sub>3</sub> and MnO<sub>2</sub>, *High Temperature Materials and Processes*, 2012, 3 (4), 459-472.
- (42) de Diego, L. F.; Gayán, P.; García-Labiano, F.; Celaya, J.; Abad, A.; Adánez, J. Impregnated CuO/Al<sub>2</sub>O<sub>3</sub> Oxygen Carriers for Chemical-Looping Combustion: Avoiding Fluidized Bed Agglomeration, *Energy & Fuels*, 2005, 19 (5), 1850-1856.
- (43) Chuang, S. Y.; Dennis, J. S.; Hayhurst, A. N.; Scott, S. A. Development and performance of Cu-based oxygen carriers for chemical-looping combustion, *Combustion and Flame*, 2008, 154 (1–2), 109-121.
- (44) Forero, C. R.; Gayán, P.; García-Labiano, F.; de Diego, L. F.; Abad, A.; Adánez, J. High temperature behaviour of a CuO/γAl<sub>2</sub>O<sub>3</sub> oxygen carrier for chemical-looping combustion, *International Journal of Greenhouse Gas Control*, 2011, 5 (4), 659-667.
- (45) Gayán, P.; Forero, C. R.; Abad, A.; de Diego, L. F.; García-Labiano, F.; Adánez, J. Effect of Support on the Behavior of Cu-Based Oxygen Carriers during Long-Term CLC Operation at Temperatures above 1073 K, *Energy & Fuels*, 2011, 25 (3), 1316-1326.
- (46) Wang, B.; Zhao, H.; Zheng, Y.; Liu, Z.; Yan, R.; Zheng, C. Chemical looping combustion of a Chinese anthracite with Fe<sub>2</sub>O<sub>3</sub>-based and CuO-based oxygen carriers, *Fuel Processing Technology*, 2012, 96, 104-115.
- (47) Mattisson, T.; Järnäs, A.; Lyngfelt, A. Reactivity of Some Metal Oxides Supported on Alumina with Alternating Methane and Oxygen Application for Chemical-Looping Combustion, *Energy & Fuels*, 2003, 17 (3), 643-651.
- (48) de Diego, L. F.; García-Labiano, F.; Gayán, P.; Celaya, J.; Palacios, J. M.; Adánez, J. Operation of a 10 kWth chemical-looping combustor during 200 h with a CuO–Al<sub>2</sub>O<sub>3</sub> oxygen carrier, *Fuel*, 2007, 86 (7–8), 1036-1045.
- (49) de Diego, L. F.; García-Labiano, F.; Adánez, J.; Gayán, P.; Abad, A.; Corbella, B. M.; María Palacios, J. Development of Cu-based oxygen carriers for chemical-looping combustion, *Fuel*, 2004, 83 (13), 1749-1757.
- (50) Chuang, S. Y.; Dennis, J. S.; Hayhurst, A. N.; Scott, S. A. Kinetics of the chemical looping oxidation of H<sub>2</sub> by a co-precipitated mixture of CuO and Al<sub>2</sub>O<sub>3</sub>, *Chemical Engineering Research and Design*, 2011, 89 (9), 1511-1523.
- (51) Harper, R. N.; Boyce, C. M.; Scott, S. A. Oxygen carrier dispersion in inert packed beds to improve performance in chemical looping combustion, *Chemical Engineering Journal*, 2013, 234, 464-474.

- (52) Zhao, H.-y.; Cao, Y.; Orndorff, W.; Pan, W.-p. Study on modification of Cu-based oxygen carrier for chemical looping combustion, *Journal of Thermal Analysis and Calorimetry*, 2013, 113 (3), 1123-1128.
- (53) Imtiaz, Q.; Kierzkowska, A. M.; Broda, M.; Müller, C. R. Synthesis of Cu-Rich, Al<sub>2</sub>O<sub>3</sub>-Stabilized Oxygen Carriers Using a Coprecipitation Technique: Redox and Carbon Formation Characteristics, *Environmental Science and Technology*, 2012, 46 (6), 3561-3566.
- (54) Imtiaz, Q.; Kierzkowska, A. M.; Müller, C. R. Coprecipitated, Copper-Based, Alumina-Stabilized Materials for Carbon Dioxide Capture by Chemical Looping Combustion, *ChemSusChem*, 2012, 5 (8), 1610-1618.
- (55) Song, Q.; Liu, W.; Bohn, C. D.; Harper, R. N.; Sivaniah, E.; Scott, S. A.; Dennis, J. S. A high performance oxygen storage material for chemical looping processes with CO<sub>2</sub> capture, *Energy & Environmental Science*, 2013, 6 (1), 288-298.
- (56) Mei, D.; Zhao, H.; Ma, Z.; Zheng, C. Using the Sol-Gel-Derived CuO/CuAl<sub>2</sub>O<sub>4</sub> Oxygen Carrier in Chemical Looping with Oxygen Uncoupling for Three Typical Coals, *Energy & Fuels*, 2013, 27 (5), 2723-2731.
- (57) Wang, S.; Luo, M.; Wang, G.; Wang, L.; Lv, M. Analysis of Reactivity of a CuO-Based Oxygen Carrier for Chemical Looping Combustion of Coal, *Energy & Fuels*, 2012, 26 (6), 3275-3283.
- (58) van Garderen, N.; Clemens, F. J.; Graule, T. Development of copper impregnated porous granulates for chemical-looping combustion, *Fuel*, 2014, 119, 323-327.
- (59) Cui, Y.; Cao, Y.; Pan, W.-p. Preparation of copper-based oxygen carrier supported by titanium dioxide, *Journal of Thermal Analysis and Calorimetry*, 2013, 114 (3), 1089-1097.
- (60) Zhang, Y.; Doroodchi, E.; Moghtaderi, B. Chemical looping combustion of ultra low concentration of methane with Fe<sub>2</sub>O<sub>3</sub>/Al<sub>2</sub>O<sub>3</sub> and CuO/SiO<sub>2</sub>, *Applied Energy*, 2014, 113, 1916-1923.
- (61) Forero, C. R.; Gayán, P.; de Diego, L. F.; Abad, A.; García-Labiano, F.; Adánez, J. Syngas combustion in a 500 Wth Chemical-Looping Combustion system using an impregnated Cu-based oxygen carrier, *Fuel Processing Technology*, 2009, 90 (12), 1471-1479.
- (62) Forero, C. R.; Gayán, P.; García-Labiano, F.; de Diego, L. F.; Abad, A.; Adánez, J. Effect of gas composition in Chemical-Looping Combustion with copper-based oxygen carriers: Fate of sulphur, *International Journal of Greenhouse Gas Control*, 2010, 4 (5), 762-770.
- (63) Zhao, H.-y.; Cao, Y.; Kang, Z.-z.; Wang, Y.-b.; Pan, W.-p. Thermal characteristics of Cu-based oxygen carriers, *Journal of Thermal Analysis and Calorimetry*, 2012, 109 (3), 1105-1109.
- (64) Håkonsen, S. F.; Blom, R. Chemical Looping Combustion in a Rotating Bed Reactor – Finding Optimal Process Conditions for Prototype Reactor, *Environmental Science and Technology*, 2011, 45 (22), 9619-9626.
- (65) Tian, H.; Chaudhari, K.; Simonyi, T.; Poston, J.; Liu, T.; Sanders, T.; Veser, G. t.; Siriwardane, R. Chemical-looping Combustion of Coal-derived Synthesis Gas Over Copper Oxide Oxygen Carriers, *Energy & Fuels*, 2008, 22 (6), 3744-3755.
- (66) Corbella, B. M.; de Diego, L.; García-Labiano, F.; Adánez, J.; Palacios, J. M. Characterization and Performance in a Multicycle Test in a Fixed-Bed Reactor of Silica-Supported Copper Oxide as Oxygen Carrier for Chemical-Looping Combustion of Methane, *Energy & Fuels*, 2005, 20 (1), 148-154.
- (67) Corbella, B. M.; De Diego, L.; García, F.; Adánez, J.; Palacios, J. M. The Performance in a Fixed Bed Reactor of Copper-Based Oxides on Titania as Oxygen Carriers for Chemical Looping Combustion of Methane, *Energy & Fuels*, 2005, 19 (2), 433-441.
- (68) Adánez, J.; Gayán, P.; Celaya, J.; de Diego, L. F.; García-Labiano, F.; Abad, A. Chemical Looping Combustion in a 10 kW<sub>th</sub> Prototype Using a CuO/Al<sub>2</sub>O<sub>3</sub> Oxygen Carrier: Effect of Operating

Conditions on Methane Combustion, *Industrial & Engineering Chemistry Research*, 2006, 45 (17), 6075-6080.

(69) Adánez, J.; de Diego, L. F.; García-Labiano, F.; Gayán, P.; Abad, A.; Palacios, J. M. Selection of Oxygen Carriers for Chemical-Looping Combustion, *Energy & Fuels*, 2004, 18 (2), 371-377.

(70) Saha, C.; Bhattacharya, S. Comparison of CuO and NiO as oxygen carrier in chemical looping combustion of a Victorian brown coal, *International Journal of Hydrogen Energy*, 2011, 36 (18), 12048-12057.

(71) Saha, C.; Zhang, S.; Xiao, R.; Bhattacharya, S. Chemical Looping Combustion (CLC) of two Victorian brown coals – Part 2: Assessment of interaction between CuO and minerals inherent in coals during multi cycle experiments, *Fuel*, 2012, 96, 335-347.

(72) Chuang, S. Y.; Dennis, J. S.; Hayhurst, A. N.; Scott, S. A. *Kinetics of Oxidation of a Reduced Form of the Cu-Based Oxygen-Carrier for Use in Chemical-Looping Combustion*, *Proceedings of the 20<sup>th</sup> International Conference on Fluidized Bed Combustion*, Yue, G.; Zhang, H.; Zhao, C.; Luo, Z. (Ed.), Springer: Berlin, 2010.

(73) Chuang, S. Y.; Dennis, J. S.; Hayhurst, A. N.; Scott, S. A. Kinetics of the chemical looping oxidation of CO by a co-precipitated mixture of CuO and Al<sub>2</sub>O<sub>3</sub>, *Proceedings of the Combustion Institute*, 2009, 32 (2), 2633-2640.

(74) Chuang, S. Y.; Dennis, J. S.; Hayhurst, A. N.; Scott, S. A. Kinetics of the Oxidation of a Co-precipitated Mixture of Cu and Al<sub>2</sub>O<sub>3</sub> by O<sub>2</sub> for Chemical-Looping Combustion, *Energy & Fuels*, 2010, 24 (7), 3917-3927.

(75) García-Labiano, F.; Adánez, J.; de Diego, L. F.; Gayán, P.; Abad, A. Effect of Pressure on the Behavior of Copper-, Iron-, and Nickel-Based Oxygen Carriers for Chemical-Looping Combustion, *Energy & Fuels*, 2005, 20 (1), 26-33.

(76) Monazam, E. R.; Breault, R. W.; Siriwardane, R.; Tian, H.; Simonyi, T.; Carpenter, S. Effect of Carbon Deposition on the Oxidation Rate of Copper/Bentonite in the Chemical Looping Process, *Energy & Fuels*, 2012, 26 (11), 6576-6583.

(77) Monazam, E. R.; Siriwardane, R.; Breault, R. W.; Tian, H.; Shadle, L. J.; Richards, G.; Carpenter, S. Kinetics of the Reduction of CuO/Bentonite by Methane (CH<sub>4</sub>) during Chemical Looping Combustion, *Energy & Fuels*, 2012, 26 (5), 2779-2785.

(78) Sahir, A. H.; Lighty, J. S.; Sohn, H. Y. Kinetics of Copper Oxidation in the Air Reactor of a Chemical Looping Combustion System using the Law of Additive Reaction Times, *Industrial & Engineering Chemistry Research*, 2011, 50 (23), 13330-13339.

(79) García-Labiano, F.; de Diego, L. F.; Adánez, J.; Abad, A.; Gayán, P. Reduction and Oxidation Kinetics of a Copper-Based Oxygen Carrier Prepared by Impregnation for Chemical-Looping Combustion, *Industrial & Engineering Chemistry Research*, 2004, 43 (26), 8168-8177.

(80) Yamarte, L.; Paxman, D.; Begum, S.; Sarkar, P.; Chambers, A. TG measurement of reactivity of candidate oxygen carrier materials, *Journal of Thermal Analysis and Calorimetry*, 2013, *In press*.

(81) Wang, S.; Wang, G.; Jiang, F.; Luo, M.; Li, H. Chemical looping combustion of coke oven gas by using Fe<sub>2</sub>O<sub>3</sub>/CuO with MgAl<sub>2</sub>O<sub>4</sub> as oxygen carrier, *Energy & Environmental Science*, 2010, 3 (9), 1353-1360.

(82) Mattisson, T.; Leion, H.; Lyngfelt, A. Chemical-looping with oxygen uncoupling using CuO/ZrO<sub>2</sub> with petroleum coke, *Fuel*, 2009, 88 (4), 683-690.

(83) Adánez-Rubio, I.; Gayán, P.; Abad, A.; de Diego, L. F.; García-Labiano, F.; Adánez, J. Evaluation of a Spray-Dried CuO/MgAl<sub>2</sub>O<sub>4</sub> Oxygen Carrier for the Chemical Looping with Oxygen Uncoupling Process, *Energy & Fuels*, 2012, 26 (5), 3069-3081.

- (84) Gayán, P.; Adánez-Rubio, I.; Abad, A.; de Diego, L. F.; García-Labiano, F.; Adánez, J. Development of Cu-based oxygen carriers for Chemical-Looping with Oxygen Uncoupling (CLOU) process, *Fuel*, 2012, 96, 226-238.
- (85) Leion, H.; Mattisson, T.; Lyngfelt, A. Using chemical-looping with oxygen uncoupling (CLOU) for combustion of six different solid fuels, *Energy Procedia*, 2009, 1 (1), 447-453.
- (86) Hedayati, A.; Azad, A.-M.; Rydén, M.; Leion, H.; Mattisson, T. Evaluation of Novel Ceria-Supported Metal Oxides As Oxygen Carriers for Chemical-Looping Combustion, *Industrial & Engineering Chemistry Research*, 2012, 51 (39), 12796-12806.
- (87) Peterson, S. B.; Konya, G.; Clayton, C. K.; Lewis, R. J.; Wilde, B. R.; Eyring, E. M.; Whitty, K. J. Characteristics and CLOU Performance of a Novel SiO<sub>2</sub>-Supported Oxygen Carrier Prepared from CuO and β-SiC, *Energy & Fuels*, 2013, 27 (10), 6040-6047.
- (88) Moldenhauer, P.; Rydén, M.; Mattisson, T.; Lyngfelt, A. Chemical-looping combustion and chemical-looping with oxygen uncoupling of kerosene with Mn- and Cu-based oxygen carriers in a circulating fluidized-bed 300W laboratory reactor, *Fuel Processing Technology*, 2012, 104, 378-389.
- (89) Adánez-Rubio, I.; Abad, A.; Gayán, P.; García-Labiano, F.; de Diego, L. F.; Adánez, J. The fate of sulphur in the Cu-based Chemical Looping with Oxygen Uncoupling (CLOU) Process, *Applied Energy*, 2014, 113, 1855-1862.
- (90) Xu, L.; Wang, J.; Li, Z.; Cai, N. Experimental Study of Cement-Supported CuO Oxygen Carriers in Chemical Looping with Oxygen Uncoupling (CLOU), *Energy & Fuels*, 2013, 27 (3), 1522-1530.
- (91) Eyring, E. M.; Konya, G.; Lighty, J. S.; Sahir, A. H.; Sarofim, A. F.; Whitty, K. Chemical Looping with Copper Oxide as Carrier and Coal as Fuel, *Oil & Gas Science and Technology*, 2011, 66 (2), 209-221.
- (92) Wen, Y.-y.; Li, Z.-s.; Xu, L.; Cai, N.-s. Experimental Study of Natural Cu Ore Particles as Oxygen Carriers in Chemical Looping with Oxygen Uncoupling (CLOU), *Energy & Fuels*, 2012, 26 (6), 3919-3927.
- (93) Clayton, C. K.; Whitty, K. J. Measurement and modeling of decomposition kinetics for copper oxide-based chemical looping with oxygen uncoupling, *Applied Energy*, 2014, 116, 416-423.
- (94) Mattisson, T. Materials for Chemical-Looping with Oxygen Uncoupling, *ISRN Chemical Engineering*, 2013, 1-19.
- (95) Rydén, M.; Leion, H.; Mattisson, T.; Lyngfelt, A. Combined oxides as oxygen-carrier material for chemical-looping with oxygen uncoupling, *Applied Energy*, 2013, 113, 1924-1932.
- (96) Imtiaz, Q.; Hosseini, D.; Müller, C. R. Review of Oxygen Carriers for Chemical Looping with Oxygen Uncoupling (CLOU): Thermodynamics, Material Development, and Synthesis, *Energy Technology*, 2013, 1 (11), 633-647.
- (97) Fossdal, A.; Bakken, E.; Øye, B. A.; Schøning, C.; Kaus, I.; Mokkelbost, T.; Larring, Y. Study of inexpensive oxygen carriers for chemical looping combustion, *International Journal of Greenhouse Gas Control*, 2011, 5 (3), 483-488.
- (98) Sarshar, Z.; Kleitz, F.; Kaliaguine, S. Novel oxygen carriers for chemical looping combustion: La<sub>1-x</sub>Ce<sub>x</sub>BO<sub>3</sub> (B = Co, Mn) perovskites synthesized by reactive grinding and nanocasting, *Energy & Environmental Science*, 2011, 4 (10), 4258-4269.
- (99) Sarshar, Z.; Sun, Z.; Zhao, D.; Kaliaguine, S. Development of Sinter-Resistant Core-Shell LaMn<sub>x</sub>Fe<sub>1-x</sub>O<sub>3</sub>@mSiO<sub>2</sub> Oxygen Carriers for Chemical Looping Combustion, *Energy & Fuels*, 2012, 26 (5), 3091-3102.
- (100) Readman, J. E.; Olafsen, A.; Larring, Y.; Blom, R. La<sub>0.8</sub>Sr<sub>0.2</sub>Co<sub>0.2</sub>Fe<sub>0.8</sub>O<sub>3-δ</sub> as a potential oxygen carrier in a chemical looping type reactor, an in-situ powder X-ray diffraction study, *Journal of Materials Chemistry*, 2005, 15 (19), 1931-1937.

- (101) Leion, H.; Larring, Y.; Bakken, E.; Bredesen, R.; Mattisson, T.; Lyngfelt, A. Use of  $\text{CaMn}_{0.875}\text{Ti}_{0.125}\text{O}_3$  as Oxygen Carrier in Chemical-Looping with Oxygen Uncoupling, *Energy & Fuels*, 2009, 23 (10), 5276-5283.
- (102) Rydén, M.; Lyngfelt, A.; Mattisson, T.; Chen, D.; Holmen, A.; Bjørgum, E. Novel oxygen-carrier materials for chemical-looping combustion and chemical-looping reforming;  $\text{La}_x\text{Sr}_{1-x}\text{Fe}_y\text{Co}_{1-y}\text{O}_{3-\delta}$  perovskites and mixed-metal oxides of  $\text{NiO}$ ,  $\text{Fe}_2\text{O}_3$  and  $\text{Mn}_3\text{O}_4$ , *International Journal of Greenhouse Gas Control*, 2008, 2 (1), 21-36.
- (103) Noorman, S.; Gallucci, F.; van Sint Annaland, M.; Kuipers, J. A. M. Experimental Investigation of Chemical-Looping Combustion in Packed Beds: A Parametric Study, *Industrial & Engineering Chemistry Research*, 2011, 50 (4), 1968-1980.
- (104) Hallberg, P.; Jing, D.; Rydén, M.; Mattisson, T.; Lyngfelt, A. Chemical Looping Combustion and Chemical Looping with Oxygen Uncoupling Experiments in a Batch Reactor Using Spray-Dried  $\text{CaMn}_{1-x}\text{M}_x\text{O}_{3-\delta}$  ( $\text{M} = \text{Ti}, \text{Fe}, \text{Mg}$ ) Particles as Oxygen Carriers, *Energy & Fuels*, 2013, 27 (3), 1473-1481.
- (105) Jing, D.; Mattisson, T.; Leion, H.; Rydén, M.; Lyngfelt, A. Examination of Perovskite Structure  $\text{CaMnO}_{3-\delta}$  with  $\text{MgO}$  Addition as Oxygen Carrier for Chemical Looping with Oxygen Uncoupling Using Methane and Syngas, *International Journal of Chemical Engineering*, 2013, 1-16.
- (106) de Diego, L. F.; Abad, A.; Cabello, A.; Gayán, P.; García-Labiano, F.; Adánez, J. Reduction and Oxidation Kinetics of a  $\text{CaMn}_{0.9}\text{Mg}_{0.1}\text{O}_{3-\delta}$  Oxygen Carrier for Chemical Looping Combustion, *Industrial & Engineering Chemistry Research*, 2014, 53 (1), 87-103.
- (107) Sarshar, Z.; Kaliaguine, S. Reduction Kinetics of Perovskite-Based Oxygen Carriers for Chemical Looping Combustion, *Industrial & Engineering Chemistry Research*, 2013, 52 (21), 6946-6955.
- (108) Leonidova, E.; Leonidov, I. A.; Patrakeev, M. V.; Kozhevnikov, V. L. Oxygen non-stoichiometry, high-temperature properties, and phase diagram of  $\text{CaMnO}_{3-\delta}$ , *Journal of Solid State Electrochemistry*, 2011, 15 (5), 1071-1075.
- (109) Bakken, E.; Norby, T.; Stølen, S. Nonstoichiometry and reductive decomposition of  $\text{CaMnO}_{3-\delta}$ , *Solid State Ionics*, 2005, 176 (1-2), 217-223.
- (110) Rørmak, L.; Wiik, K.; Stolen, S.; Grande, T. Oxygen stoichiometry and structural properties of  $\text{La}_{1-x}\text{A}_x\text{MnO}_{3\pm\delta}$  ( $\text{A} = \text{Ca}$  or  $\text{Sr}$  and  $0 \leq x \leq 1$ ), *Journal of Materials Chemistry*, 2002, 12 (4), 1058-1067.
- (111) Rydén, M.; Lyngfelt, A.; Mattisson, T.  $\text{CaMn}_{0.875}\text{Ti}_{0.125}\text{O}_3$  as oxygen carrier for chemical-looping combustion with oxygen uncoupling (CLOU) – Experiments in a continuously operating fluidized-bed reactor system, *International Journal of Greenhouse Gas Control*, 2011, 5 (2), 356-366.
- (112) Källén, M.; Rydén, M.; Dueso, C.; Mattisson, T.; Lyngfelt, A.  $\text{CaMn}_{0.9}\text{Mg}_{0.1}\text{O}_{3-\delta}$  as Oxygen Carrier in a Gas-Fired 10  $\text{kW}_{\text{th}}$  Chemical-Looping Combustion Unit, *Industrial & Engineering Chemistry Research*, 2013, 52 (21), 6923-6932.
- (113) Shulman, A.; Linderholm, C.; Mattisson, T.; Lyngfelt, A. High Reactivity and Mechanical Durability of  $\text{NiO}/\text{NiAl}_2\text{O}_4$  and  $\text{NiO}/\text{NiAl}_2\text{O}_4/\text{MgAl}_2\text{O}_4$  Oxygen Carrier Particles Used for more than 1000 h in a 10 kW CLC Reactor, *Industrial & Engineering Chemistry Research*, 2009, 48 (15), 7400-7405.
- (114) Linderholm, C.; Abad, A.; Mattisson, T.; Lyngfelt, A. 160 h of chemical-looping combustion in a 10 kW reactor system with a  $\text{NiO}$ -based oxygen carrier, *International Journal of Greenhouse Gas Control*, 2008, 2 (4), 520-530.
- (115) Koponen, M. J.; Venäläinen, T.; Suvanto, M.; Kallinen, K.; Kinnunen, T.-J. J.; Härkönen, M.; Pakkanen, T. A. Methane conversion and  $\text{SO}_2$  resistance of  $\text{LaMn}_{1-x}\text{Fe}_x\text{O}_3$  ( $x = 0.4, 0.5, 0.6, 1$ )

perovskite catalysts promoted with palladium, *Journal of Molecular Catalysis A: Chemical*, 2006, 258 (1–2), 246-250.

(116) Rosso, I.; Saracco, G.; Specchia, V.; Garrone, E. Sulphur poisoning of  $\text{LaCr}_{0.5-x}\text{Mn}_x\text{Mg}_{0.5}\text{O}_3\cdot\gamma\text{MgO}$  catalysts for methane combustion, *Applied Catalysis B: Environmental*, 2003, 40 (3), 195-205.

(117) Alifanti, M.; Auer, R.; Kirchnerova, J.; Thyron, F.; Grange, P.; Delmon, B. Activity in methane combustion and sensitivity to sulfur poisoning of  $\text{La}_{1-x}\text{Ce}_x\text{Mn}_{1-y}\text{Co}_y\text{O}_3$  perovskite oxides, *Applied Catalysis B: Environmental*, 2003, 41 (1–2), 71-81.

(118) Zhu, Y.; Tan, R.; Feng, J.; Ji, S.; Cao, L. The reaction and poisoning mechanism of  $\text{SO}_2$  and perovskite  $\text{LaCoO}_3$  film model catalysts, *Applied Catalysis A: General*, 2001, 209 (1–2), 71-77.

(119) Wang, H.; Zhu, Y.; Tan, R.; Yao, W. Study on the Poisoning Mechanism of Sulfur Dioxide for Perovskite  $\text{La}_{0.9}\text{Sr}_{0.1}\text{CoO}_3$  Model Catalysts, *Catalysis Letters*, 2002, 82 (3–4), 199-204.

(120) Zhang, R.; Alamdari, H.; Kaliaguine, S.  $\text{SO}_2$  poisoning of  $\text{LaFe}_{0.8}\text{Cu}_{0.2}\text{O}_3$  perovskite prepared by reactive grinding during  $\text{NO}$  reduction by  $\text{C}_3\text{H}_6$ , *Applied Catalysis A: General*, 2008, 340 (1), 140-151.

(121) *Properties and Applications of Perovskite-Type Oxides*, Tejuca, L. G.; Fierro, J. L. G. (Ed.), Marcel Dekker: New York, 1993.

(122) Li, W.; Dai, H.; Lieu, Y. *Improving  $\text{SO}_2$  Resistance of Base Metal Perovskite Type Oxidation Catalyst*, Studies in Surface Science and Catalysis, Guzzi, L.; Solymosi, f.; Tétéyi, P. (Ed.), Elsevier: Budapest, 1993.

(123) Rosso, I.; Saracco, G.; Specchia, V. Tackling the problem of sulfur poisoning of perovskite catalysts for natural gas combustion, *Korean Journal of Chemical Engineering*, 2003, 20 (2), 222-229.

(124) Sundqvist, S.; Leion, H.; Rydén, M.; Lyngfelt, A.; Mattisson, T.  $\text{CaMn}_{0.875}\text{Ti}_{0.125}\text{O}_{3-\delta}$  as an Oxygen Carrier for Chemical-Looping with Oxygen Uncoupling (CLOU) – Solid-Fuel Testing and Sulfur Interaction, *Energy Technology*, 2013, 1 (5–6), 338-344.

(125) Cabello, A.; Abad, A.; Gayán, P.; de Diego, L. F.; García-Labiano, F.; Adánez, J. Effect of operating conditions and  $\text{H}_2\text{S}$  presence on performance of  $\text{CaMg}_{0.1}\text{Mn}_{0.9}\text{O}_{3-\delta}$  perovskite material in CLC, *Energy & Fuels*, 2014, *In press*.

(126) Hansen, P. F. B.; Dam-Johansen, K.; Østergaard, K. High-temperature reaction between sulphur dioxide and limestone – V. The effect of periodically changing oxidizing and reducing conditions, *Chemical Engineering Science*, 1993, 48 (7), 1325-1341.

(127) Fernández, M. J.; Lyngfelt, A.; Steenari, B. M. Reaction between limestone and  $\text{SO}_2$  under conditions alternating between oxidizing and reducing. The effect of the  $\text{SO}_2$  concentration, *Journal of the Institute of Energy*, 2000, 73 (495), 119-125.

(128) Mattisson, T.; Lyngfelt, A. The reaction between sulphur dioxide and limestone under periodically changing oxidising and reducing conditions – The effect of reducing gases, *Journal of the Institute of Energy*, 1998, 71 (489), 190-196.

(129) Bale, C. W.; Bélisle, E.; Chartrand, P.; Deckerov, S. A.; Eriksson, G.; Hack, K.; Jung, I. H.; Kang, Y. B.; Melançon, J.; Pelton, A. D.; Robelin, C.; Petersen, S. FactSage thermochemical software and databases – recent developments, *Calphad*, 2009, 33 (2), 295-311.

(130) Chadda, D.; Ford, J. D.; Fahim, M. A. Chemical Energy Storage by the Reaction Cycle  $\text{CuO}/\text{Cu}_2\text{O}$  *International Journal of Energy Research*, 1989, 13 (63), 63-73.

(131) Sahir, A. H.; Lighty, J. S.; Sohn, H. Y.; Leion, H. Rate Analysis of Chemical-Looping with Oxygen Uncoupling (CLOU) for Solid Fuels, *Energy & Fuels*, 2012, 26 (7), 4395-4404.

- (132) Clayton, C. K.; Sohn, H. Y.; Whitty, K. J. Oxidation Kinetics of  $\text{Cu}_2\text{O}$  in Oxygen Carriers for Chemical Looping with Oxygen Uncoupling, *Industrial & Engineering Chemistry Research*, 2014.
- (133) Leion, H.; Mattisson, T.; Lyngfelt, A. Use of Ores and Industrial Products As Oxygen Carriers in Chemical-Looping Combustion, *Energy & Fuels*, 2009, 23 (4), 2307-2315.
- (134) Rydén, M.; Lyngfelt, A.; Mattisson, T. Combined manganese/iron oxides as oxygen carrier for chemical looping combustion with oxygen uncoupling (CLOU) in a circulating fluidized bed reactor system, *Energy Procedia*, 2011, 4, 341-348.
- (135) Linderholm, C.; Lyngfelt, A.; Cuadrat, A.; Jerndal, E. Chemical-looping combustion of solid fuels – Operation in 10 kW unit with two fuels, above-bed and in-bed fuel feed and two oxygen carriers, manganese ore and ilmenite, *Fuel*, 2012, 102, 808-822.
- (136) US Geological Survey Mineral Commodity Summaries, 2011, ISBN 978-1-4113-3083-2.
- (137) Adánez, J.; Cuadrat, A.; Abad, A.; Gayán, P.; de Diego, L. F.; García-Labiano, F. Ilmenite Activation during Consecutive Redox Cycles in Chemical-Looping Combustion, *Energy & Fuels*, 2010, 24 (2), 1402-1413.
- (138) Leion, H.; Lyngfelt, A.; Johansson, M.; Jerndal, E.; Mattisson, T. The use of ilmenite as an oxygen carrier in chemical-looping combustion, *Chemical Engineering Research and Design*, 2008, 86 (9), 1017-1026.
- (139) Zafar, Q.; Abad, A.; Mattisson, T.; Gevert, B.; Strand, M. Reduction and oxidation kinetics of  $\text{Mn}_3\text{O}_4/\text{Mg-ZrO}_2$  oxygen carrier particles for chemical-looping combustion, *Chemical Engineering Science*, 2007, 62 (23), 6556-6567.
- (140) Johansson, M.; Mattisson, T.; Lyngfelt, A. Investigation of  $\text{Mn}_3\text{O}_4$  With Stabilized  $\text{ZrO}_2$  for Chemical-Looping Combustion, *Chemical Engineering Research and Design*, 2006, 84 (9), 807-818.
- (141) Rasband, W. S. *ImageJ*, National Institutes of Health: Bethesda, 1997.
- (142) Rydén, M.; Moldenhauer, P.; Lindqvist, S.; Mattisson, M.; Lyngfelt, A. Measuring attrition resistance of oxygen carrier particles for chemical-looping combustion with the jet cup method, *Submitted for publication*, 2014.
- (143) *Perry's Chemical Engineering Handbook*, Perry, R. H.; Green, D. W. (Ed.), 7<sup>th</sup> ed., McGraw-Hill, 1997.
- (144) Cho, P.; Mattisson, T.; Lyngfelt, A. Carbon Formation on Nickel and Iron Oxide-Containing Oxygen Carriers for Chemical-Looping Combustion, *Industrial & Engineering Chemistry Research*, 2005, 44 (4), 668-676.
- (145) Gadalla, A. M. M.; White, J. Equilibrium Relationships in the System  $\text{CuO-Cu}_2\text{O-Al}_2\text{O}_3$ , *Trans. Brit. Ceram. Soc.*, 1964, 63 (1), 39-62.
- (146) Scientific Group Thermodata Europe (SGTE) *Thermodynamic Properties of Inorganic Material compiled by SGTE*, Pure Substances Elements and Compounds from AgBr to  $\text{Ba}_3\text{N}_2$ , Hurtado, I.; Neuschütz, D. (Ed.), SpringerMaterials – The Landolt-Börnstein Database, 1999, 208.
- (147) *Thermochemical properties of inorganic substances*, Knacke, O.; Kubaschewski, O.; Hesselmann, K. (Ed.), 2<sup>nd</sup> ed., Springer-Verlag: Berlin, 1991, 627.
- (148) Barin, I. *Thermochemical data of pure substances, in collaboration with Gregor Platzki*, Karin, S.; James, G. (Ed.), 3<sup>rd</sup> ed., VCH Verlagsgesellschaft mbH: Weinheim, 1995.
- (149) Tsuchida, T.; Furuichi, R.; Sukegawa, T.; Furudate, M.; Ishii, T. Thermoanalytical study on the reaction of the  $\text{CuO-Al}_2\text{O}_3$  ( $\eta$ ,  $\gamma$  and  $\alpha$ ) systems, *Thermochimica Acta*, 1984, 78 (1-3), 71-80.
- (150) Susnitzky, D. W.; Carter, C. B. The formation of copper aluminate by solid-state reaction, *Journal of Materials Research*, 1991, 6 (09), 1958-1963.

- (151) Bolt, P. H.; Habraken, F. H. P. M.; Geus, J. W. Formation of Nickel, Cobalt, Copper, and Iron Aluminates from  $\alpha$ - and  $\gamma$ -Alumina-Supported Oxides: A Comparative Study, *Journal of Solid State Chemistry*, 1998, 135 (1), 59-69.
- (152) Tang, Y.; Chui, S. S.-Y.; Shih, K.; Zhang, L. Copper Stabilization via Spinel Formation during the Sintering of Simulated Copper-Laden Sludge with Aluminum-Rich Ceramic Precursors, *Environmental Science and Technology*, 2011, 45 (8), 3598-3604.
- (153) Tsuboi, N.; Itoh, Y.; Ogata, J.; Kobayashi, S.; Shimizu, H.; Kato, K.; Kaneko, F. Composition and Structure Control of Cu–Al–O Films Prepared by Reactive Sputtering and Annealing, *Japanese Journal of Applied Physics*, 2007, 46 (1), 351-355.
- (154) Woelk, H.-J.; Hoffmann, B.; Mestl, G.; Schloegl, R. Experimental Archaeology: Investigation on the Copper–Aluminum–Silicon–Oxygen System, *Journal of the American Ceramic Society*, 2002, 85 (7), 1876-1878.
- (155) Patrick, V.; Gavalas, G. R.; Flytzani-Stephanopoulos, M.; Jothimurugesan, K. High-temperature sulfidation-regeneration of copper(II) oxide-alumina sorbents, *Industrial & Engineering Chemistry Research*, 1989, 28 (7), 931-940.
- (156) Patrick, V.; Gavalas, G. Structure and Reduction and Mixed Copper-Aluminum Oxide, *Journal of the American Ceramic Society*, 1990, 73 (2), 358-369.
- (157) Zalazinskii, A. G.; Balakirev, V. F.; Chebotaev, N. M.; Chufarov, G. I. Thermodynamic Analysis of the Reduction, Dissociation, and Formation of Copper(I) Aluminate ( $\text{CuAlO}_2$ ), Chromate(III) ( $\text{CuCrO}_2$ ), and Ferrate(II) ( $\text{CuFeO}_2$ ) from the Free Elements and Oxides, *Russian Journal of Inorganic Chemistry (Translation of Zhurnal Neorganicheskoi Khimii)*, 1969, 14 (3), 326-328.
- (158) Kumekawa, Y.; Hirai, M.; Kobayashi, Y.; Endoh, S.; Oikawa, E.; Hashimoto, T. Evaluation of thermodynamic and kinetic stability of  $\text{CuAlO}_2$  and  $\text{CuGaO}_2$ , *Journal of Thermal Analysis and Calorimetry*, 2010, 99 (1), 57-63.
- (159) Siriwardane, R.; Tian, H.; Miller, D.; Richards, G.; Simonyi, T.; Poston, J. Evaluation of reaction mechanism of coal-metal oxide interactions in chemical-looping combustion, *Combustion and Flame*, 2010, 157 (11), 2198-2208.
- (160) Khawam, A.; Flanagan, D. R. Solid-State Kinetic Models: Basics and Mathematical Fundamentals, *The Journal of Physical Chemistry B*, 2006, 110 (35), 17315-17328.
- (161) Mattisson, T.; Lyngfelt, A.; Cho, P. The use of iron oxide as an oxygen carrier in chemical-looping combustion of methane with inherent separation of  $\text{CO}_2$ , *Fuel*, 2001, 80 (13), 1953-1962.
- (162) Abad, A.; Adánez, J.; García-Labiano, F.; de Diego, L. F.; Gayán, P.; Celaya, J. Mapping of the range of operational conditions for Cu-, Fe-, and Ni-based oxygen carriers in chemical-looping combustion, *Chemical Engineering Science*, 2007, 62 (1–2), 533-549.
- (163) Keller, M.; Leion, H.; Mattisson, T.; Lyngfelt, A. Gasification inhibition in chemical-looping combustion with solid fuels, *Combustion and Flame*, 2011, 158 (3), 393-400.
- (164) Hüttinger, K. J.; Merdes, W. F. The carbon-steam reaction at elevated pressure: Formations of product gases and hydrogen inhibitions, *Carbon*, 1992, 30 (6), 883-894.
- (165) Gadsby, J.; Hinshelwood, C. N.; Sykes, K. W. The Kinetics of the Reactions of the Steam-Carbon System, *Proceedings of the Royal Society of London. Series A. Mathematical and Physical Sciences*, 1946, 187 (1009), 129-151.
- (166) McKee, D. W. Gasification of graphite in carbon dioxide and water vapor – the catalytic effects of alkali metal salts, *Carbon*, 1982, 20 (1), 59-66.
- (167) McKee, D. W.; Chatterji, D. The catalytic behavior of alkali metal carbonates and oxides in graphite oxidation reactions, *Carbon*, 1975, 13 (5), 381-390.

- (168) Kwon, T. W.; Kim, J. R.; Kim, S. D.; Park, W. H. Catalytic steam gasification of lignite char, *Fuel*, 1989, 68 (4), 416-421.
- (169) Ye, D. P.; Agnew, J. B.; Zhang, D. K. Gasification of a South Australian low-rank coal with carbon dioxide and steam: kinetics and reactivity studies, *Fuel*, 1998, 77 (11), 1209-1219.
- (170) Fox, D. A.; White, A. H. Effect of Sodium Carbonate upon Gasification of Carbon and Production of Producer Gas, *Industrial & Engineering Chemistry Research*, 1931, 23 (3), 259-266.
- (171) Kapteijn, F.; Abbel, G.; Moulijn, J. A. CO<sub>2</sub> gasification of carbon catalysed by alkali metals: Reactivity and mechanism, *Fuel*, 1984, 63 (8), 1036-1042.
- (172) Nandi, S. P.; Johnson, J. L. Catalytic gasification of lignite chars, *Symposium on Coal Gasification Chemistry, Washington, USA – Division of Fuels, American Chemical Society*, 1979, 24 (3), 17-27.
- (173) Guo, D.-l.; Wu, S.-b.; Liu, B.; Yin, X.-l.; Yang, Q. Catalytic effects of NaOH and Na<sub>2</sub>CO<sub>3</sub> additives on alkali lignin pyrolysis and gasification, *Applied Energy*, 2012, 95, 22-30.
- (174) Gu, H.; Shen, L.; Xiao, J.; Zhang, S.; Song, T.; Chen, D. Iron ore as oxygen carrier improved with potassium for chemical looping combustion of anthracite coal, *Combustion and Flame*, 2012, 159 (7), 2480-2490.
- (175) Wigmans, T.; Göebel, J. C.; Moulijn, J. A. The influence of pretreatment conditions on the activity and stability of sodium and potassium catalysts in carbon-steam reactions, *Carbon*, 1983, 21 (3), 295-301.
- (176) Baker, R. T. K.; Chludzinski Jr, J. J. Catalytic gasification of graphite by chromium and copper in oxygen, steam and hydrogen, *Carbon*, 1981, 19 (2), 75-82.
- (177) Spiro, C. L.; McKee, D. W.; Kosky, P. G.; Lamby, E. J. Observation of alkali catalyst particles during gasification of carbonaceous materials in CO<sub>2</sub> and steam, *Fuel*, 1984, 63 (5), 686-691.
- (178) Moulijn, J. A.; Cerfontain, M. B.; Kapteijn, F. Mechanism of the potassium catalysed gasification of carbon in CO<sub>2</sub>, *Fuel*, 1984, 63 (8), 1043-1047.
- (179) Keller, M.; Leion, H.; Mattisson, T. Mechanisms of Solid Fuel Conversion by Chemical-Looping Combustion (CLC) using Manganese Ore: Catalytic Gasification by Potassium Compounds, *Energy Technology*, 2013, 1 (4), 273-282.
- (180) Brown, T. A.; Scala, F.; Scott, S. A.; Dennis, J. S.; Salatino, P. The attrition behaviour of oxygen-carriers under inert and reacting conditions, *Chemical Engineering Science*, 2012, 71, 449-467.
- (181) Sim, C. Y.; Brown, T.; Chen, Q.; Sharifi, V.; Swithenbank, J.; Dennis, J.; Scott, S. Particle characterisation in chemical looping combustion, *Chemical Engineering Science*, 2012, 69 (1), 211-224.
- (182) Varela, A.; Dios, S. d.; Parras, M.; Hernando, M. a.; Fernández-Díaz, M. T.; Landa-Cánovas, A. R.; González-Calbet, J. M. Ordered Rock-Salt Related Nanoclusters in CaMnO<sub>2</sub>, *Journal of the American Chemical Society*, 2009, 131 (24), 8660-8668.
- (183) Reller, A.; Davoodabady, G.; Oswald, H. R. Reversible topotactic reduction of perovskite-related calcium manganese oxides, *Thermochimica Acta*, 1985, 83 (1), 121-124.
- (184) Poeppelmeier, K. R.; Horowitz, H. S.; Longo, J. M. Oxide solid solutions derived from homogeneous carbonate precursors: The CaO–MnO solid solution, *Journal of the Less Common Metals*, 1986, 116 (1), 219-227.
- (185) Shannon, R. D. Revised effective ionic radii and systematic studies of interatomic distances in halides and chalcogenides, *Acta Crystallographica Section A*, 1976, 32 (5), 751-767.